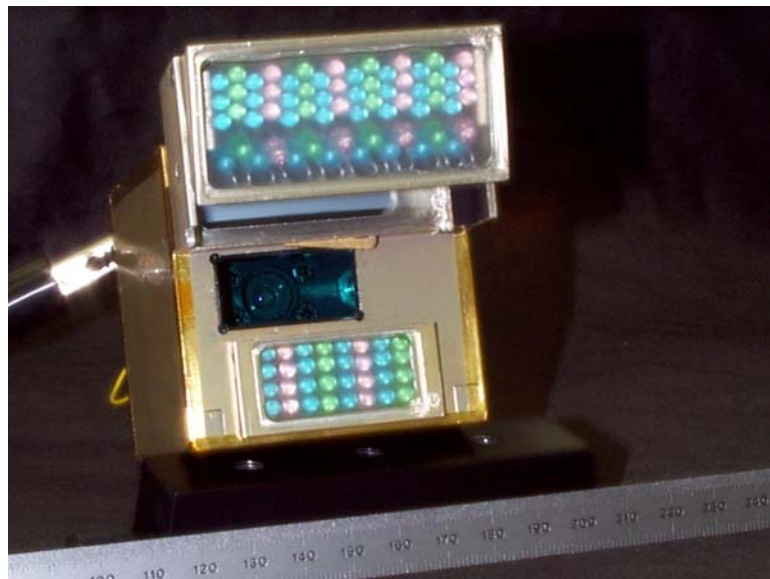# 2007 Phoenix Mars Scout Mission and Mars Surveyor 2001 Robotic Arm Camera (RAC) Calibration Report

Version 1.0

November 20, 2008

Brent J. Bos, Peter H. Smith, Roger Tanner, Robert Reynolds, Robert Marcialis
University of Arizona Lunar and Planetary

Table of Contents

2007 Phoenix Mars Scout Mission and Mars Surveyor 2001 Robotic Arm Camera

(RAC) Calibration Report

Brent J. Bos, Peter H. Smith, Roger Tanner, Robert Reynolds, Robert Marcialis
University of Arizona Lunar and Planetary Laboratory

1.0 Introduction

In the fall of 1999, the Mars Atmospheric and Geologic Imaging (MAGI) team of the University of Arizona's Lunar and Planetary Laboratory (Tucson, Arizona) delivered a flight ready Robotic Arm Camera (RAC) to the Jet Propulsion Laboratory (JPL) in Pasadena, California. This instrument was designed to be mounted between the wrist and elbow joints of the Robotic Arm (RA) onboard the Mars Surveyor 2001 lander to provide operational support and scientific imaging on the Martian surface. In particular, the RAC was to provide images of trenches dug by the RA and document the contents of the RA scoop. And in the event of poor performance by the lander panoramic camera, the RAC would serve as a back-up capable of stereoscopic, panoramic imaging with 2 mrad/pixel resolution. This document reports the results of the MAGI team RAC laboratory calibration testing. The delta calibration done to the RAC for the 2007 Phoenix Mars mission did not show any changes in the cameras calibration verse the 01 calibration.

2.0 Instrument Description

At the heart of the Robotic Arm Camera lies a 512-square pixel (512x256 pixels exposed for imaging), frame-transfer, charge-coupled-device (CCD) manufactured by

Loral in Huntington Beach, California and provided by our German partners at MPAe

(Max-Planck-Institut für Aeronomie) led by Dr. H. Uwe Keller (Katlenburg-Lindau,

Germany). See Figure 2.1. The detector does not include a mechanical shutter but the
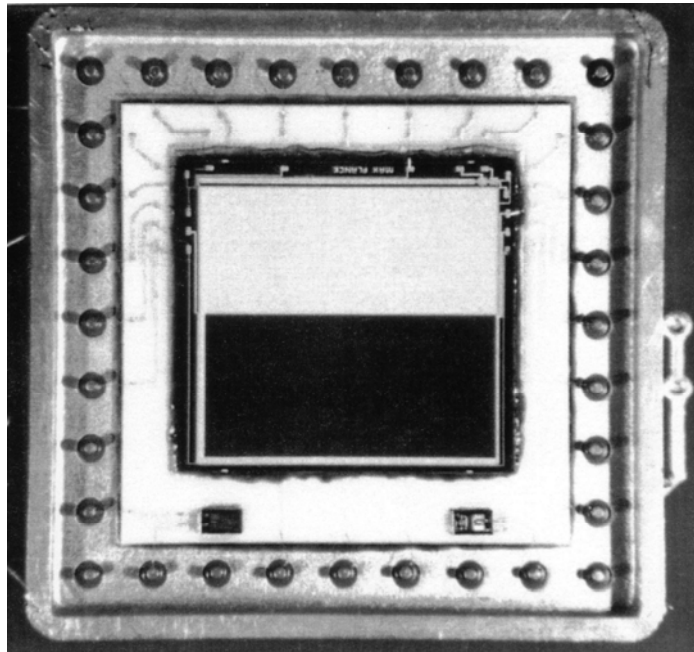
Figure 2.1 Image of the type of detector used in the RAC.

transfer of image charge to the storage section takes only 0.5 ms. The chip is read out

with a 12-bit analog-to-digital converter (ADC) to provide an image data range of 0-4095

digital numbers (DN). The pixels' active area is 17x23 μm with a 23 μm pixel pitch. The

pixels' active area is not square due to the presence of anti-blooming gates which run

vertically along the array (see Figure 2.2).

This particular detector packaging design was originally developed by MPAe for

the Cassini Huygens Descent Imager and Spectral Radiometer currently enroute to

Saturn. This same detector design was used in the highly successful Imager for Mars

Pathfinder (IMP) which returned over 16,000 images of the Martian landscape from July
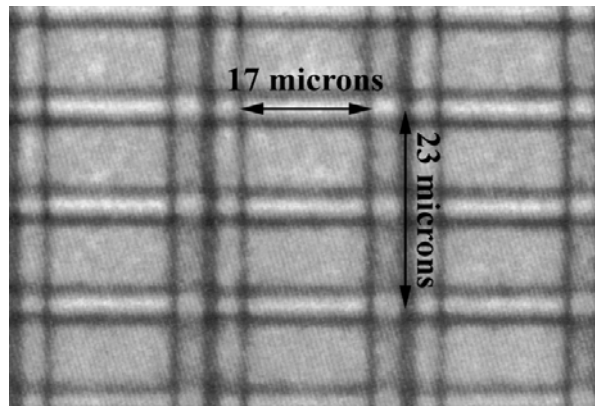
Figure 2.2 Close-up image detail of RAC pixels.

4, 1997 to September 28, 1997 (*Reid et al*.,1999). The same design was also used in the

Surface Stereo Imager (SSI) and RAC onboard the ill-fated Mars Polar Lander (MPL).

Due to the loss of the lander, no images were returned from the Martian surface but the

cameras once again proved their ability to survive launch and cruise when they returned

dark frames during the end of the MPL cruise phase.

The RAC optical system consists of a 12.5 mm focal length, four-element double-

Gauss lens operating at f/11.23-f/23.0 with a window of BG40 filter glass from Schott

Glass Technologies positioned between the lenses and the outside scene. The BG40 filter

is included to block near-infrared radiation greater than 700 nm. In addition, a sapphire

cover window can be rotated into place to protect the filter window from dust storms and

flying debris kicked up by RA digging operations. This cover window is transparent so that in the case of a cover motor failure, the RAC can still obtain high-quality images. In order to provide images of objects as close as 11 mm to as far away as infinity, the Gaussian lens cell is mounted on a small, motorized translation stage. The stage can provide 313 different focus positions ranging from focus step 0 for 1:1 conjugate ratio imaging, to focus step 312 for objects at infinity. The field of view at infinity focus is roughly 25° x 50°.

Unlike the IMP and SSI, the RAC does not have discrete narrow band-pass filters to provide color images. Instead the RAC can provide its own light in red, green, and blue. Two assemblies of light emitting diodes (LED) are mounted to the RAC front face, an upper assembly and a lower assembly. The lower assembly consists of 8 red, 8 green, and 16 blue LEDs. The upper assembly has 16 red, 16 green, and 32 blue LED's aimed to illuminate the RA scoop and 4 red, 4 green, and 8 blue LED's pointed down to illuminate the RA scoop blade and other close-up objects. Exposures can be captured in the three colors to provide color images of any object when the reflected radiance of ambient light is low relative to the LED light. This condition can occur when: objects are in the scoop, an object is in the lander's shadow, an RA trench is deep enough to provide shadow, or the sun has set.

3.0 Calibration Overview

In many ways, modern spacecraft imagers have much in common with the solid-state cameras used today in consumer goods, manufacturing, transportation, and the

entertainment industry. But the mandatory reliability of spacecraft imagers in the harsh launch and space environment is certainly one area where they differ from typical cameras. Another, and arguably, equally important way in which a spacecraft camera differs from other cameras is in how well the imager's performance is known. The process of accurately knowing the camera's performance is called calibration. Calibration is so important to spacecraft instrumentation because without it, an instrument's user cannot be sure how to interpret the returned data. An observed effect could be due to the object under observation; or it could simply be caused by the instrument that did the observing. An instrument's calibration allows us to be able to tell the difference.

The Robotic Arm Camera's performance was extensively studied and measured during a four-month period from July 1999 to October 1999. This activity was conducted in the University of Arizona Lunar Planetary Laboratory (LPL) clean room by MAGI team members which included Roger Tanner, Bob Marcialis, Robert Reynolds, Brent Bos, and Terry Friedman. This team came highly qualified to the task after having previously calibrated three flight ready cameras: the Imager for Mars Pathfinder, the MPL Surface Stereo Imager, and the MPL RAC. In addition, most of the test fixtures, instruments, and set-ups were the same as used for those three instruments.

The data files were stored in UAX format on the local LPL network in the /home/mars/uatest/Database/RF directory. This directory is divided into sub-directories named after the type of test data stored there. The directory tree structure is as follows:

/home/mars/uatest/Database/RF/*test type*/*test location*/FIM/*date(yymmdd)*/*file name*. For

instance, an image data file for a test completed on September 9, 1999 can be found at

/home/mars/uatest/Database/RF/AR/UA/FIM/990929 with an image file name of

990929190631.B.495.RF.AR.UA.FIM. Table 3.2 lists what directories correspond to

Calibration Test	Date	Test Details
Flat Fields	7-21-99	Pre-vibration testing
	7-23-99	Post-vibration testing
Focus Table	8-2-99 -- 9-19-99	
Geometric Distortion	9-19-99	
MTF	9-19-99	10:1 vertical slits, cover up
	9-20-99	10:1 vertical slits, cover down
	9-20-99	10:1 horizontal slits, cover up
	9-20-99	10:1 horizontal slits, cover down
	10-6-99	1:1 vertical slits, cover up
	10-6-99	1:1 vertical slits, cover down
	10-7-99	1:1 horizontal slits, cover up
	10-7-99	1:1 horizontal slits, cover down
	10-7-99	1:1 45° slits, cover up
	10-7-99	1:1 45° slits, cover down
	10-8-99	10:1 45° slits, cover up
	10-8-99	10:1 45° slits, cover down
Lamp Responsivity with Temperature	9-29-99	-115° C
	9-29-99	-70° C
	9-29-99	-30° C
	9-29-99	0° C
	9-29-99	30° C
	10-4-99	Room temperature
	10-4-99	Room temperature, chamber open
Absolute Responsivity with Temperature	9-28-99	-115° C
	9-29-99	-70° C
	9-29-99	-30° C
	9-29-99	0° C
	9-29-99	30° C
	10-4-99	Room temperature
	10-4-99	Room temperature, chamber open
LED Lamp Spectra with Temperature	9-28-99	-115° C
	9-29-99	-70° C
	9-29-99	-30° C
	9-29-99	0° C
	9-29-99 – 9-30-99	30° C
	10-4-99	Room temperature
	10-4-99	Room temperature, chamber open
Responsivity with Focus	10-5-99	
Image Response Uniformity	10-5-99	DISR 24" integrating sphere with LED's on and off
Upper Lamps Baffle Test	10-11-99	
Scoop Images	10-11-99	
Stray Light	10-12-99	
	10-13-99	New set-up
	10-14-99	
	10-15-99	1:1
	10-18-99	Vertical 1:1
	10-19-99	Vertical 1:1
	10-18-99	Close focus
	10-19-99	∞ focus
LED Lamp Flat Fields	10-20-99	Focus step 300, dist.=285 mm, both lamps
	10-20-99	Focus step 292, dist.=169 mm, both lamps
	10-20-99	Focus step 279, dist.=99 mm, both lamps
	10-20-99	Focus step 265, dist.=66.7 mm, both lamps
	10-20-99	Focus step 250, dist.=48.6 mm, both lamps
	10-21-99	Focus step 250, dist.=48.6 mm, upper lamps
	10-21-99	Focus step 265, dist.=66.7 mm, upper lamps
	10-21-99	Focus step 279, dist.=99 mm, upper lamps
	10-21-99	Focus step 292, dist.=169 mm, upper lamps
	10-21-99	Focus step 234, dist.=37.1 mm, upper lamps
	10-21-99	Focus step 217, dist.=29.37 mm, upper lamps
	10-21-99	Focus step 198, dist.=23.69 mm, upper lamps
	10-21-99	Focus step 177, dist.=19.53 mm, upper lamps
	10-21-99	Focus step 153, dist.=16.40 mm, upper lamps
	10-21-99	Focus step 125, dist.=14.08 mm, upper lamps
	10-22-99	Focus step 87, dist.=12.32 mm, upper lamps
	10-22-99	Focus step 0, dist.=11.35 mm, upper lamps
	10-22-99	Focus step 0, dist.=11.35 mm, both lamps
	10-22-99	Focus step 87, dist.=12.32 mm, both lamps
	10-22-99	Focus step 125, dist.=14.08 mm, both lamps
	10-22-99	Focus step 153, dist.=16.40 mm, both lamps
	10-22-99	Focus step 177, dist.=19.53 mm, both lamps

	10-22-99	Focus step 198, dist.=23.69 mm, both lamps
	10-22-99	Focus step 217, dist.=29.37 mm, both lamps
	10-22-99	Focus step 234, dist.=37.10 mm, both lamps
Color Chart Imaging	10-23-99	Focus step 292, cover up, Kodak chart
	10-23-99	Focus step 292 cover down, Kodak chart
	10-23-99	Focus step 292, cover up, Kodak chart other half
	10-23-99	Focus step 292, cover down, Kodak chart other half
	10-23-99	Large Spectralon, cover up and down
Color Chip Imaging	10-23-99	Focus step 250, dist.=48.5 mm, both lamps, cover up
	10-23-99	Focus step 250, dist.=48.5 mm, both lamps, cover down
	10-23-99	Focus step 250, dist.=48.5 mm, both lamps, cover up
	10-23-99	Focus step 250, dist.=48.5 mm, both lamps, cover down
Color Chip Target Imaging	10-24-99	Focus step 0, dist.=11.35 mm, cover up

Table 3.1. Summary of RAC calibration testing.

Calibration Test Category	Directory
Absolute Responsivity	AR
Dark Current	DC
Focus	FC
Geometric Distortion	GT
Stray Light	SL
Spectral Profile	SP
Radiometric Uniformity	RU

Table 3.2. Data directory nomenclature.

4.0 Modulation Transfer Function Measurement

4.1 Modulation Transfer Function

A multitude of image quality tests can be carried-out with a camera system, including standard target imaging, bar chart imaging, point-source imaging, etc. But arguably one of the most useful descriptors of an incoherent imaging system's performance is the modulation transfer function (MTF).

A detailed explanation of MTF is beyond the scope of this text (see *Gaskill* 1978 for a complete description) but essentially an imaging system's MTF describes the sharpness of the images it can obtain by showing how the spatial frequencies present in an image are altered by the system. Any real image can be described with a Fourier series, an infinite series of sine functions. So if it is known how an imaging system alters each sine function within an image, it can be determined how the system changes the image. One can think of the term "modulation" in modulation transfer function as being equivalent to contrast. So in regards to that representation the one-dimensional MTF can be expressed as

$$\text{MTF}(\xi) = \frac{f_\xi(x\max) - f_\xi(x\min)}{f_\xi(x\max) + f_\xi(x\min)} \qquad (4.1.1)$$

where $f_\xi(x) = a_\xi \sin(2\pi\xi x) + c_\xi$, xmax and xmin are the locations of the maximum and minimum values of the function f_ξ, respectively, ξ is the spatial frequency and a_ξ and c_ξ are simple constants. Inspection of Eq. (4.1.1) reveals that the maximum possible MTF value is 1. Ideally one would like to have MTF=1 for all spatial frequencies, ξ, so that the resulting image is a perfect representation of the object. This is physically impossible, however, for an imaging system with a finite size aperture that diffracts incoming light and a finite number of pixels whose very size and spacing limit the resolution.

4.2 MTF Experimental Procedure

The task of measuring an imaging system's MTF is not a trivial one. There are several methods to measure MTF: sine patterns can be imaged and measured, point sources can be imaged and the images Fourier transformed, an edge can be imaged and differentiated, and then Fourier transformed, or a line can be imaged and Fourier transformed. We decided to use the latter method by measuring the RAC's line spread function (LSF) at 0°, 45°, and 90° relative to horizontal and Fourier transforming them to obtain MTF values.

The theory of obtaining the MTF from an LSF is well presented in *Gaskill* [1978] but we summarize the results here for the reader's convenience

$$\text{MTF}(\xi,0) = |\mathcal{F}\{\text{LSF}(x)\}|, \qquad (4.2.1)$$

where $\mathcal{F}\{\}$ represents the one-dimensional Fourier transform operation. The line spread function is simply the response of the imaging system to an infinitely thin slit. In practice, an infinitely thin slit transmits no light. So we had to choose a test target slit width that was thin, about 1/10 the width of an array pixel, but still allowed adequate light to pass. We used two different slit width sizes, 23 μm for testing at a 10:1 conjugate ratio and 2.3 μm for testing at 1:1.

A schematic of our experimental set-up is shown in Figure 4.2.1. Taking only one image of the MTF target provides a measurement of the LSF but it is poorly sampled. Figure 4.2.2 shows what an actual test image looks like. To sample properly we take an image and then move the target slightly, then take another image, and so on. The

distance moved between each image is kept constant and is controlled by a mechanical

stepper motor. By measuring the response of a single pixel at each target position, the

LSF at that pixel is known. 100-111 images were taken for each MTF profile. Three

different profiles were taken because Eq. (4.2.1) shows that line spread function testing

will only result in a one-dimensional profile of the MTF, which is a two-dimensional

function in this case. We measured horizontally, vertically and at 45° relative to the array

to help give us a picture of how the RAC's MTF looks in two-dimensions. The test was

conducted for four different imaging scenarios: 10:1 RAC cover up, 10:1 RAC cover
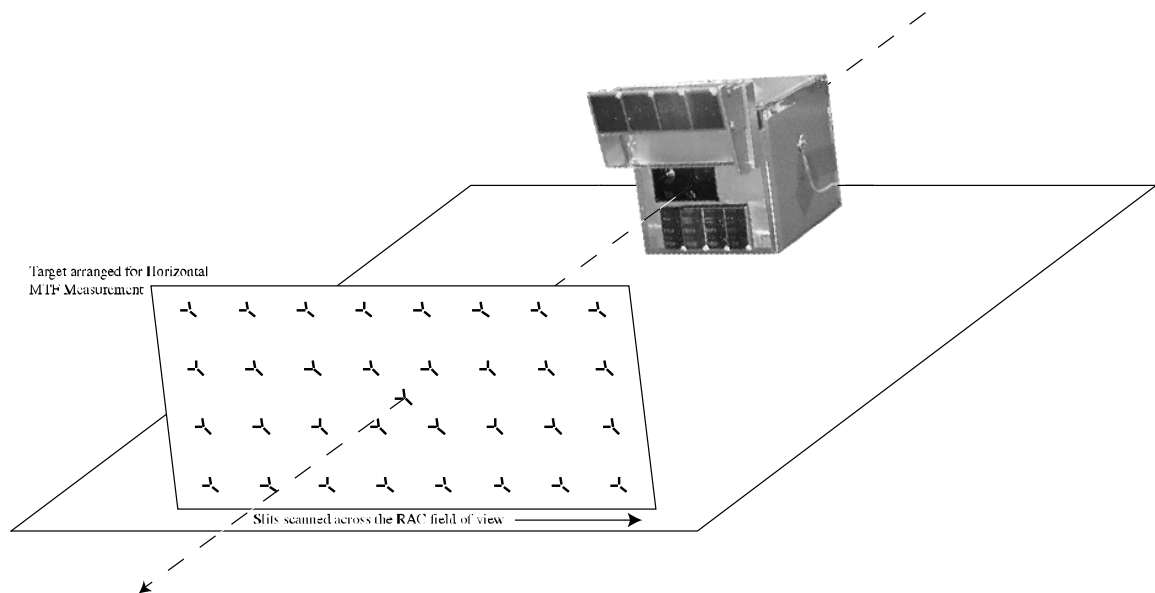
Figure 4.2.1. MTF experimental set-up schematic.
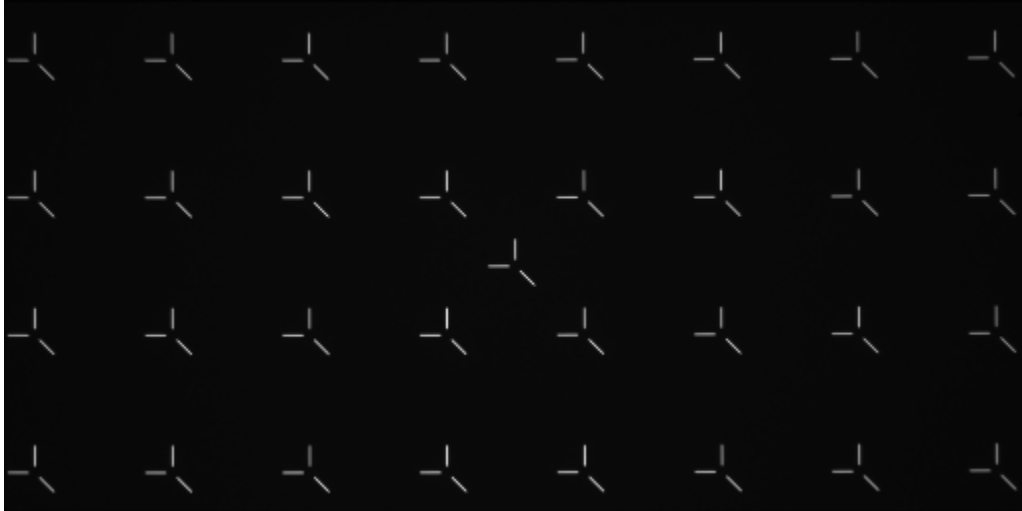
Figure 4.2.1 MTF target image back illuminated.

down, 1:1 RAC cover up, and 1:1 RAC cover down. For MTF testing, 10:1 occurred at

RAC focus motor step 279 and an object distance of 99 mm. 1:1 imaging occurred at

RAC focus motor step 0 and an object distance of 11.35 mm.

4.3 Data Analysis

4.3.1 Image Reduction

MTF data analysis is performed using Research Systems' Interactive Data

Language 5.2 (IDL) running on a *Silicon Graphics Indigo[2]* workstation. IDL is a higher

level language with built in functions that lends itself to image processing and analysis.

In addition, we use several custom pieces of IDL code in the reductions which are all part

of the MAGI team's MAGISOFT. The actual code written to perform the reductions is

rac01_mtf.pro and can be found in the LPL directory /home/lpl/brentb.

The first step in the data reduction is to change the series of images into line spread function data. Now the line spread function can just be thought of as the response history of an individual pixel to the slit image as the slits were scanned across. So the first step in the reduction is to examine the central image in each series of scans and choose the appropriate pixels to monitor. The pixels chosen were those that were as close to the center of the slits as possible and had the highest response. The chosen pixel positions are then entered into the *rac01_mtf.pro* program. The program then examines each image in a scan and records the response at each pixel site to produce LSF measurements.

Those raw LSF measurements are then further refined by subtracting an offset value from them. This is necessary because the LSF's fall to essentially constant, non-zero values far from the slit centers. This is not due to the RAC hardware offset of ~8 DN or due to thermal noise. The effects seen are too large for that. Typical values at the edge of the LSF's are 25 DN for 10:1 imaging and 140 DN for 1:1 imaging. We believe those kind of values could only be the result of stray light, multiple reflections of light bouncing off the camera face, from the dark areas of the MTF target.

So to correct for this situation, we find offset values for each pixel that when subtracted from the LSF's do not produce negative values. We want to be careful because subtracting off too large a value would produce an error in the MTF results that would show the camera's performance to be better than it was. So we find offset values in one of three ways. The first is to choose the minimum value in each LSF as the correct

offset value. The second is to look at the pixels' responses when the slits have been moved extremely far away. The very existence of this type of data is made possible by the experience gained from the three previous flight cameras calibrated by the MAGI team in which similar effects have been noticed. By moving the slits as far away as possible from the slits, the response seen for that position can only be due to reflections and not to camera blurring of the slits. When this type of data is unavailable we find DN values from other pixel sites that are further away from the slits but still close enough to the pixels of interest to be applicable. Then the offset values from these techniques are compared and the smallest values selected as the best offsets to use. A unique DN offset value is assigned to each pixel for each test. We should note that typically the offset values found with the different techniques are within a few DN of each other.

The final step in turning LSF's into MTF's essentially follows Eq. (4.2.1). The LSF's are Fourier transformed, the Fourier transforms are multiplied by their complex conjugates, and then their square roots are taken.

4.3.2 Step Size Determination

The determination of the distance the slits move on the RAC's array between each image in an LSF scan is the final piece of work required for MTF data reduction. The step size in object space is known very accurately, on the order of tens of nanometers. But converting object space step size to image space requires using other variables as well that are not known nearly as accurately.

Based on our experience with MTF testing we believe there are three reasonable

ways of determining step sizes. Method 1 is to use the relationship

$$m = \frac{f}{S_o - f} \quad , \qquad\qquad (4.3.2.1)$$

where m is magnification, S_o is the principal plane to target distance, and f is the RAC

lens effective focal length. The image space step size is then just the magnification times

the well-known object space step size. The RAC lens effective focal length is known to

reasonable accuracy since it was measured by the vendor but the principal plane to target

distance is not known nearly as well. The reason for this is that the principal plane is not

a physical plane that can be measured to. Its location is inside of the RAC lens. So

calculating the distance to the MTF target requires: knowing the distance from the

principal plane to the front lens surface (not measured by the vendor), knowing the

distance from the front lens surface to the outside-front of the RAC, and knowing the

distance from the RAC front to the MTF target. If one is extremely careful with the

measurement, considering those three error stack-ups, we estimate that S_o might be

known to ±0.75 mm. The test situation that would result in the smallest error using this

method is the one where S_o is largest. This corresponds to the10:1 set-up where S_o is

approximately 141.04 mm. So then using Eq. (4.3.2.1) and considering only the

uncertainty in the target distance, the uncertainty would be ±0.59%, a pretty good result.

Method 2 for determining step size is to use only the image data itself. This can

be done by measuring the locations of the slits on the array in the first and last images.

Once that distance is known, dividing by the number of steps taken results in the image space step size. The relative distance between pixels is known very well because the array's pixel pitch is known and modern photolithography is extremely accurate. The inaccuracy in this method comes in with knowing where the centers of the slits are on the pixels. If a pixel has a high value, it doesn't necessarily mean that the slit image is centered right on it. So it is possible to have a ±0.5 pixel error in knowing the slit center on the first image and in the last image. This gives a total possible error of ±1.0 pixel. The total distance traveled by a slit in a data series is only about 10 pixels. So use of this method would result in an uncertainty of ±10%, not even in the same ballpark as method 1 but at least it does not rely on the test technician being highly accurate with a difficult measurement.

The third and final method for determining image space step size is similar to method 2. It uses the image data, the accurately known object space step size, and the accurately known distance between slits on the MTF target to determine the magnification, m. Then, multiplication of the object space step size by m gives the image space step size. In method 3 the distance between slits is measured in the central image of an MTF image series. Just like in method 2, the uncertainty in knowing the distance between slit centers is ±1.0 pixels. But to help reduce the effect of this uncertainty one can use slits that are far apart, about 385.5 pixels. Using slits that far apart can introduce other errors, however, for instance, there might be a slight tilt in the target. For the set-ups used for RAC testing, we estimate the maximum error from target tilt alone to be about ±0.06 pixels. Also, the nominal RAC lens design does show that distortion might

be evident for a large slit separation; and more evident at 10:1 imaging then 1:1. The

design shows this could introduce ±0.5 pixel uncertainty. Taking those three errors into

account, the uncertainty in finding the image space step size would be ±0.47%.

   The preceeding analysis showed that method 1 and method 3 would have about

the same uncertainty in step size but we choose to use method 3 for three reasons: the

estimated error with method 3 is marginally lower than with method 1, the third method's

errors are better known, and we can probably know the total center to center distance

between slits with even better than ±1.0 pixel accuracy. The slit images should be

symmetrical so by using an equation similar to that used for finding the center of mass of

objects, we can estimate the center of a slit to approximately ±0.25 pixel accuracy for a

total center to center spacing error of ±0.5 pixel. We use the following calculation to

better estimate the location of the slit centers

$$x_{center} = \frac{\sum_i DN_i x_i}{\sum_i DN_i} \qquad (4.3.2.2).$$

For each slit location we determine 8 different slit center location estimates, x_{center}. And to

reduce the effect of any noise that might be present, we average those together to find the

final slit location. The inputs into Eq. (4.3.2.2) consist of three DN values and three

location values: the maximum response and location and those on either side of it. The

final distance measurement used is an average of the distance between the two most

distance slits right above target center and right below target center. So each final

distance measurement is a combination of 32 different slit location measurements. This

technique is used on each unique test set-up so that each set-up has its own step size

assigned to it. To facilitate the taking of the measurement, the *rac01_mtf_scale.pro*

program was created and is used.   It can be found in /home/lpl/brentb. Once the step

sizes are known they are used as input into the *rac01_mtf.pro* program.

4.3.3 Results

We present the final results of the RAC MTF testing for each test set-up in

Figures 4.3.3.1-4.3.3.12. Some explanation of these figures is in order to help explain

what they illustrate. The plot in the upper left corners of Fig. 4.3.3.1-4.3.3.12 is a plot of

each line spread function that we find at each pixel location that had a slit scanned across

it. The LSF's are over-plotted with each other so that the scatter in the results can be

easily seen. We find the LSF centers by using Eq. (4.3.2.2) and the central 21 values of

each LSF.

The plot directly below the LSF plot is the MTF plot calculated using Eq. (4.2.1).

Again the results for each pixel are over-plotted with each other to accentuate any data

spread. The MTF data is completely immune to any uncertainties in the LSF center

location since the Fourier transform of a shift results in a phase change in frequency

space; and since we take the absolute value of the transform we remove the phase

information. So the spread seen in the MTF results can only be caused by the data itself.

The data spread seen in the MTF plots is something we have not seen before with

the IMP, the MPL SSI, or the MPL RAC. So to help interpret what is happening with the

RAC a second column of plots is included in Fig. 4.3.3.1-4.3.3.12. The plot in the upper

right corners is a plot of image quality versus the distance from the theoretical center of

the array (255.5 pixels, 127.5 pixels, pixel positions starting at 0,0). Image quality is

defined to be the MTF at approximately 26 1/mm. Directly below that plot is a grayscale

image of image quality corresponding to where it was measured on the array. A

grayscale value of 0 is assigned to the lowest MTF and a value of 255 assigned to the

highest. Nearest neighbor interpolation is used to fill in the grayscale values on pixel

sites where the MTF was not measured. The image is orientated the same as it would be

for a regular image so that the object scene looks the same as it would if one was looking

at the object through the back of the RAC's head.

We have already discussed one portion of the uncertainty in the MTF results in

section 4.3.2. In that section we explained that the uncertainty in the LSF position and

MTF frequencies is approximately ±0.5%. The uncertainty in the MTF values though,

still needs to be discussed. There are two dominant sources of error that effect the MTF

Figure 4.3.3.1 Horizontal MTF measurements at 1:1 focus (focus motor step 0) with RAC cover up.
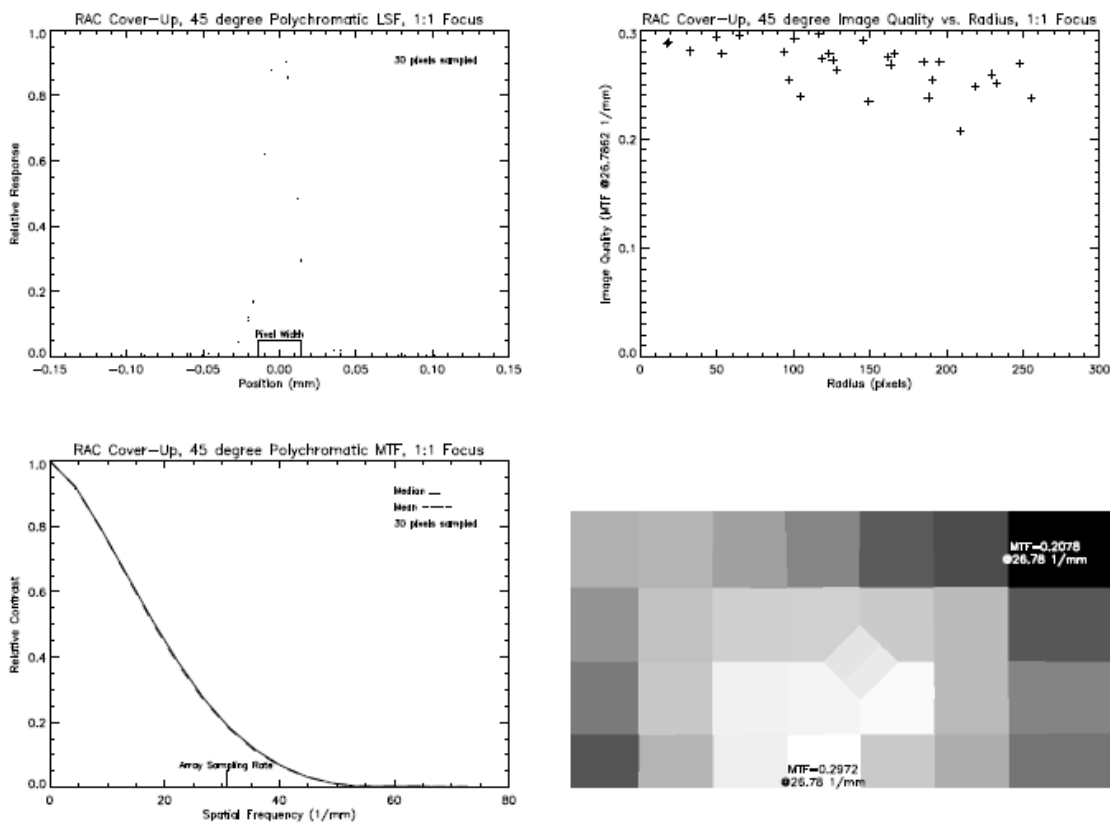
Figure 4.3.3.2 45° MTF measurements at 1:1 focus (focus motor step 0) with RAC cover up.
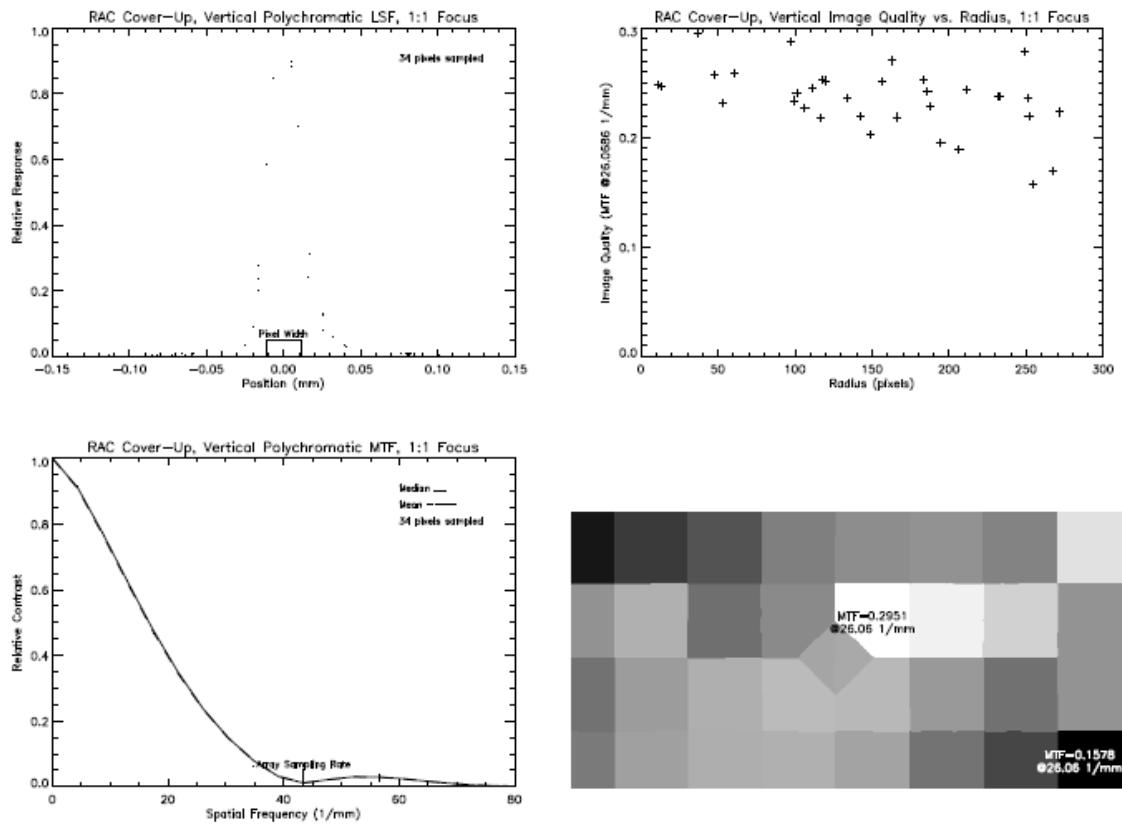
Figure 4.3.3.3 Vertical MTF measurements at 1:1 focus (focus motor step 0) with RAC cover up.
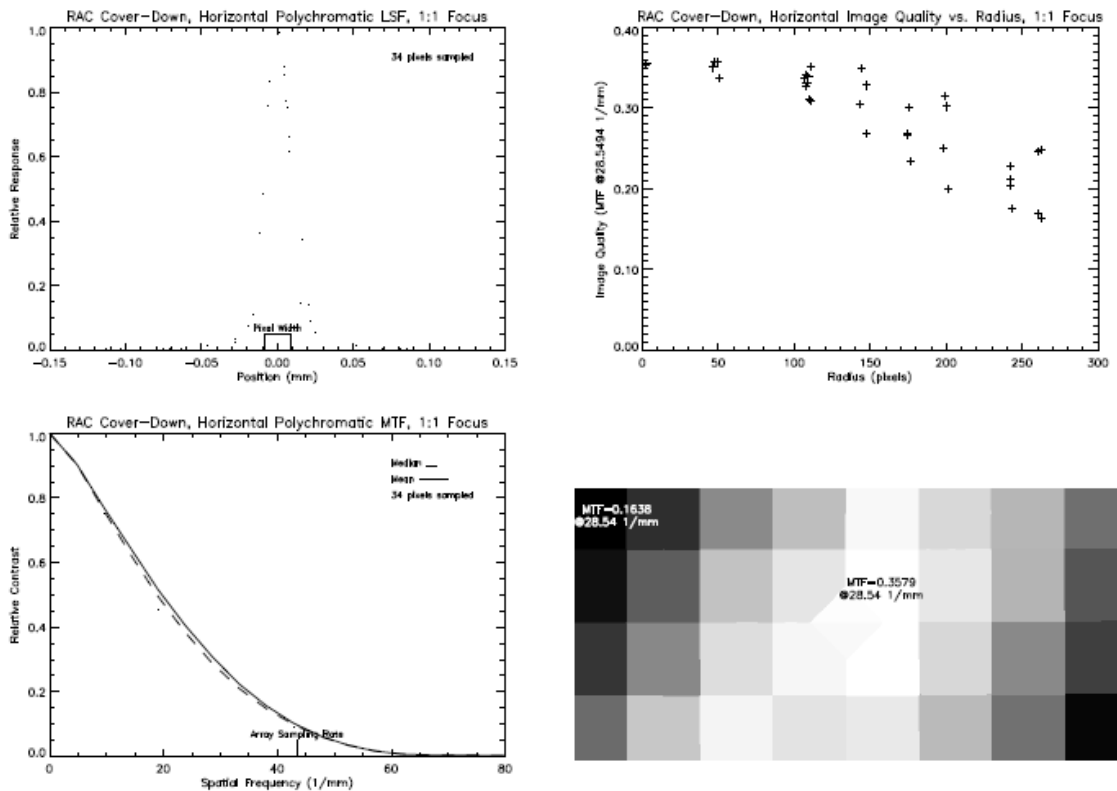
Figure 4.3.3.4 Horizontal MTF measurements at 1:1 focus (focus motor step 0) with RAC cover down.
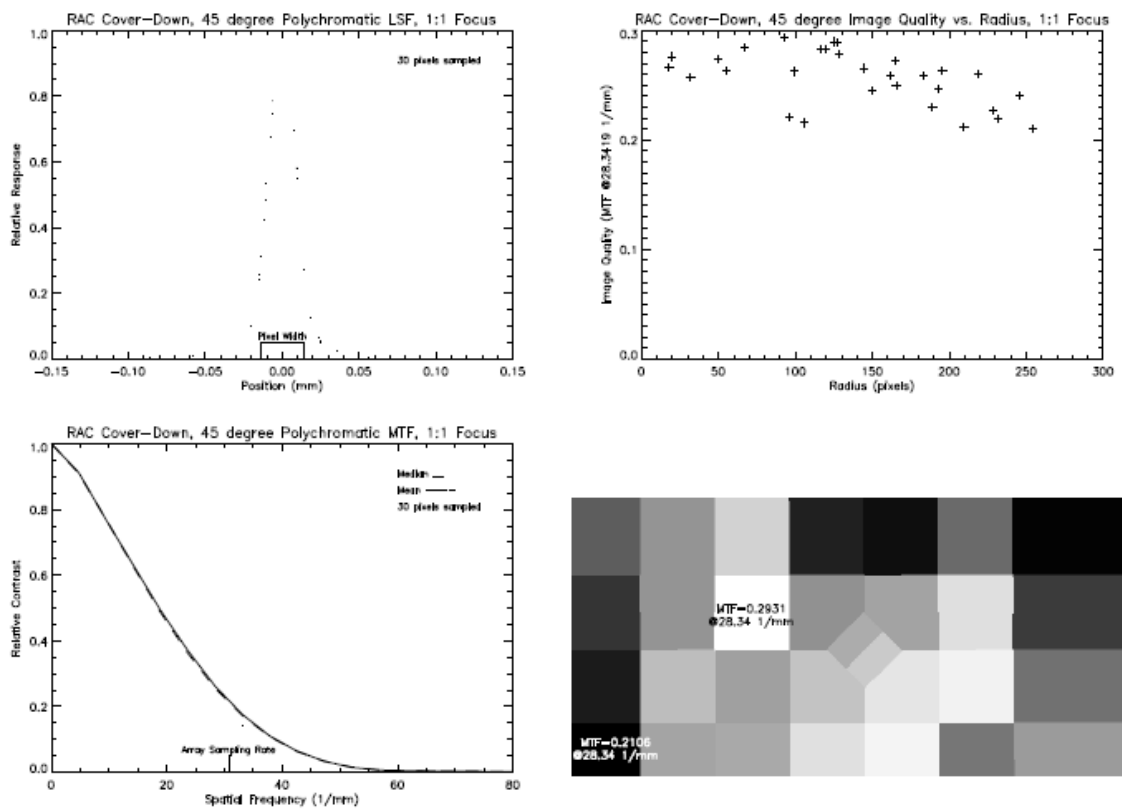
Figure 4.3.3.5 45° MTF measurements at 1:1 focus (focus motor step 0) with RAC cover down.
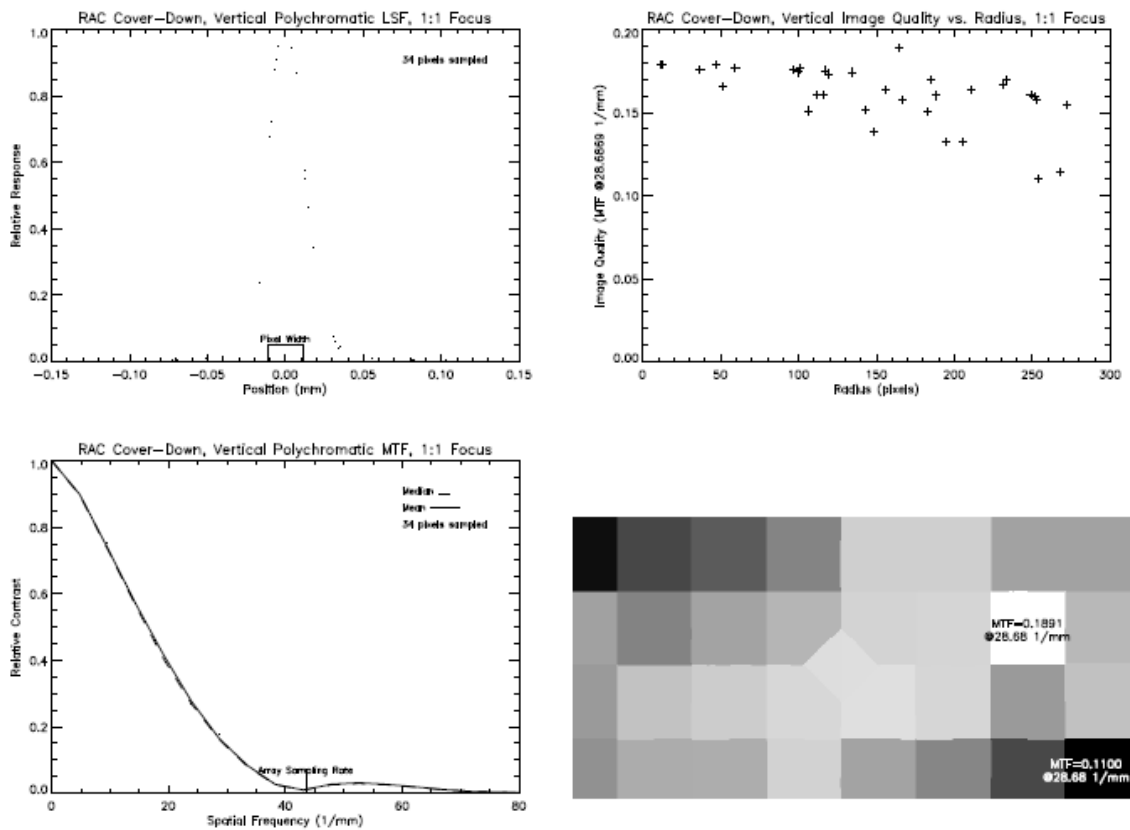
Figure 4.3.3.6 Vertical MTF measurements at 1:1 focus (focus motor step 0) with RAC cover down.
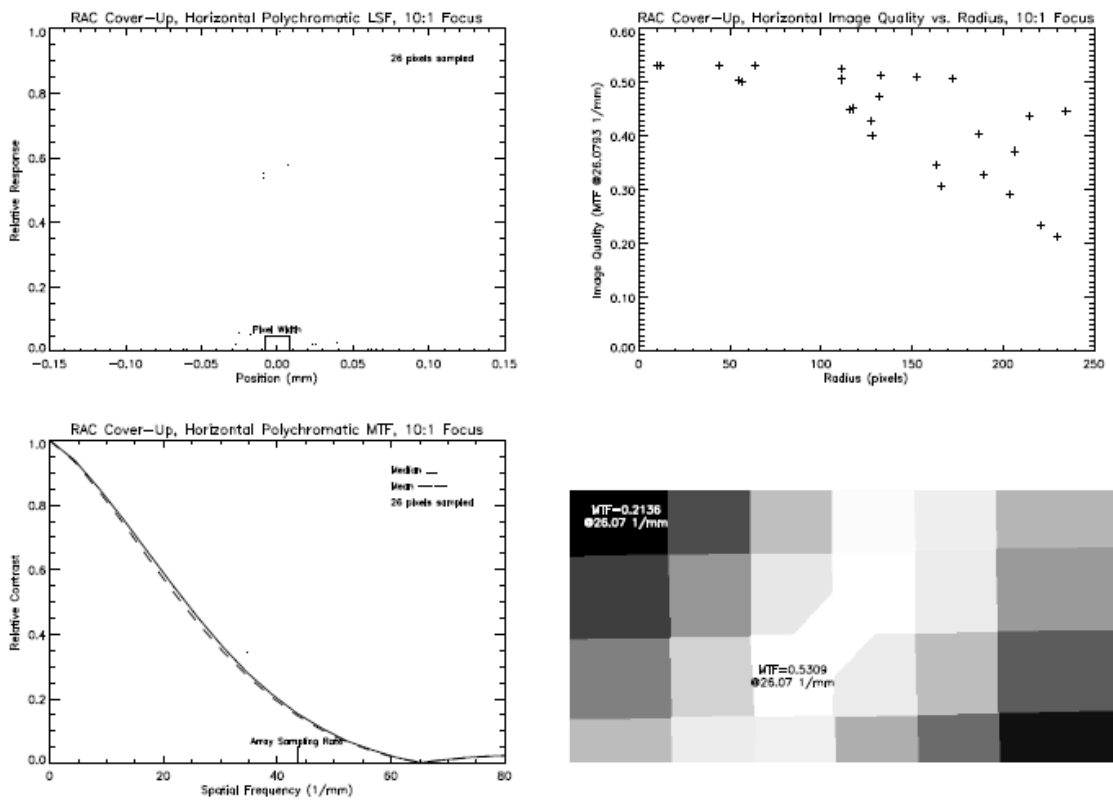
Figure 4.3.3.7 Horizontal MTF measurements at 10:1 focus (focus motor step 279) with RAC cover up.

29
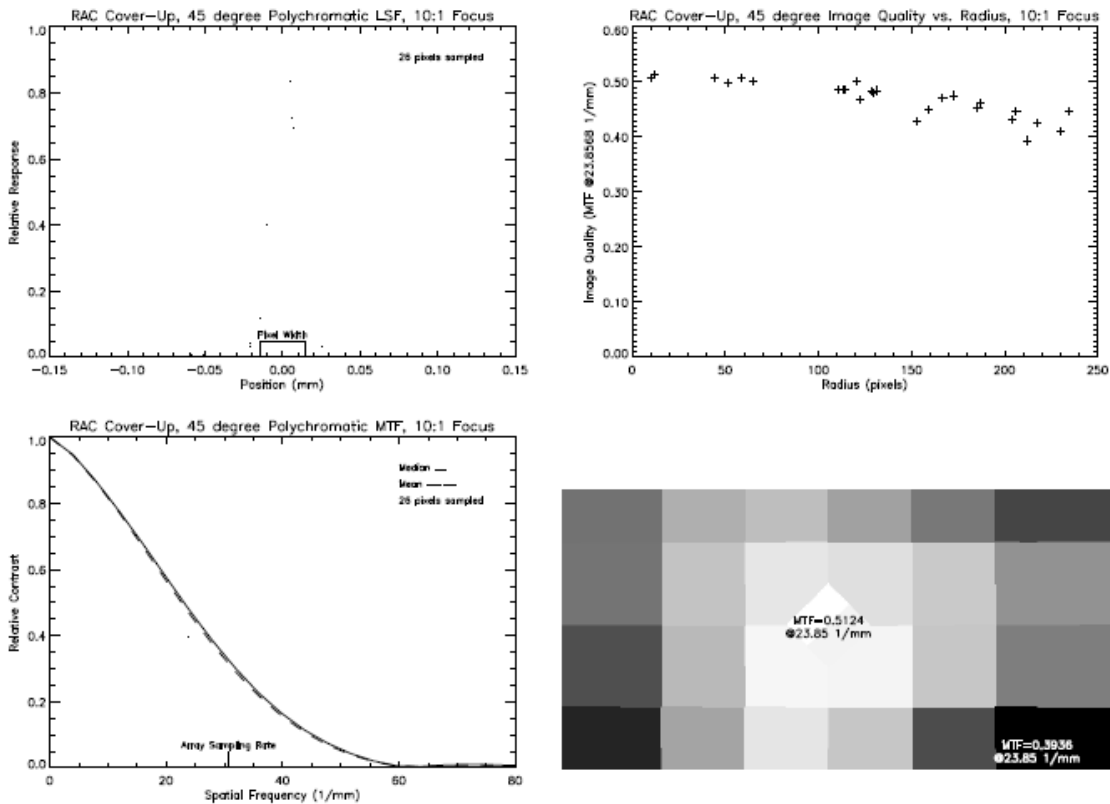
Figure 4.3.3.8 45° MTF measurements at 10:1 focus (focus motor step 279) with RAC cover up.
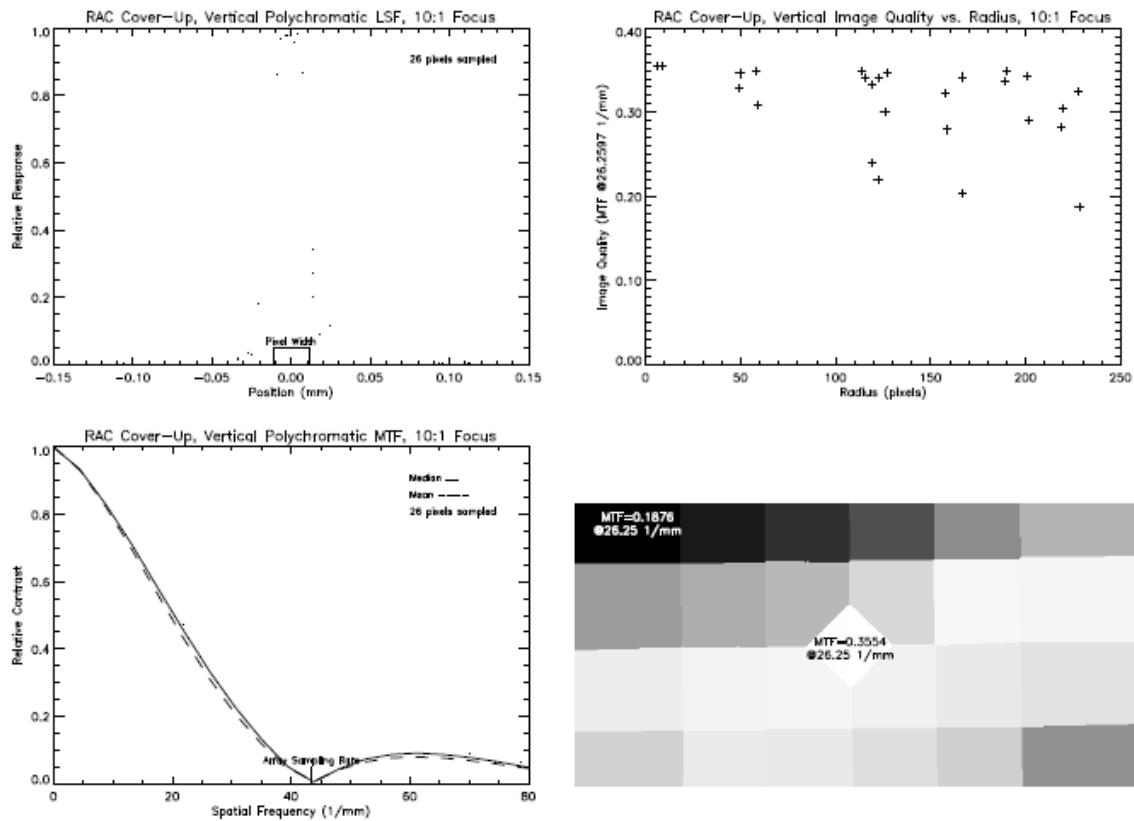
Figure 4.3.3.9 Vertical MTF measurements at 10:1 focus (focus motor step 279) with RAC cover up.
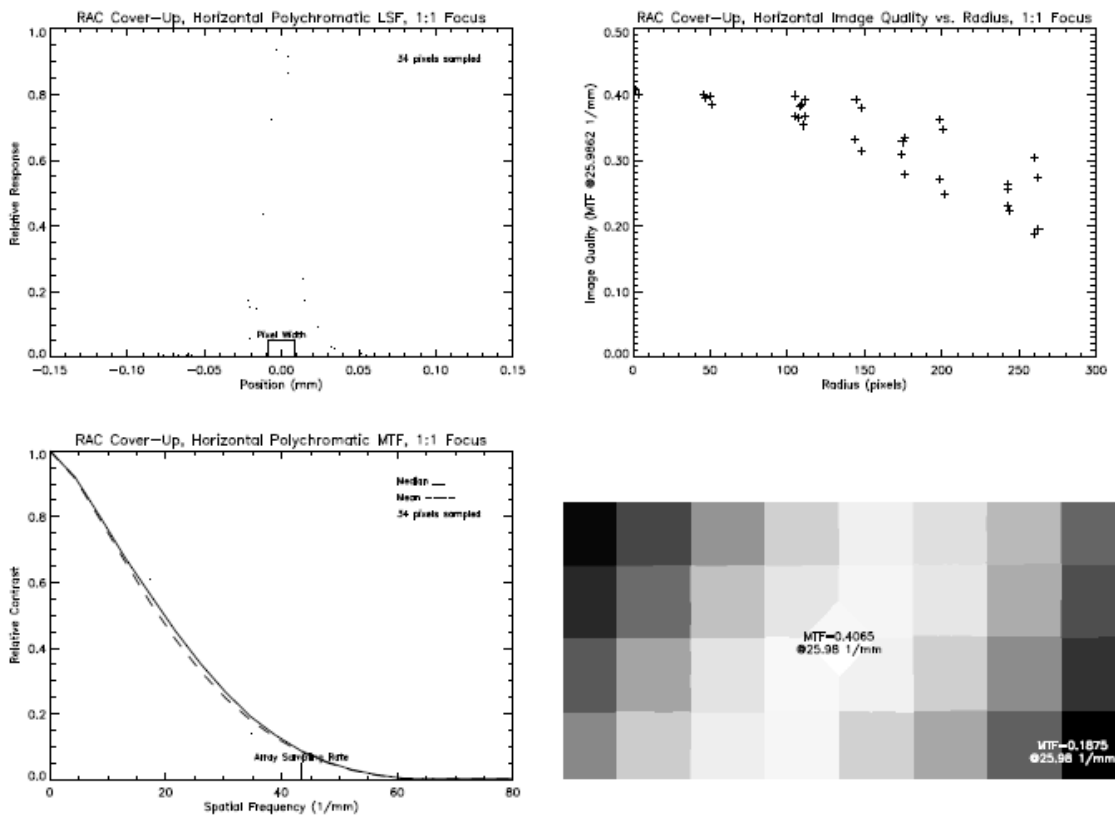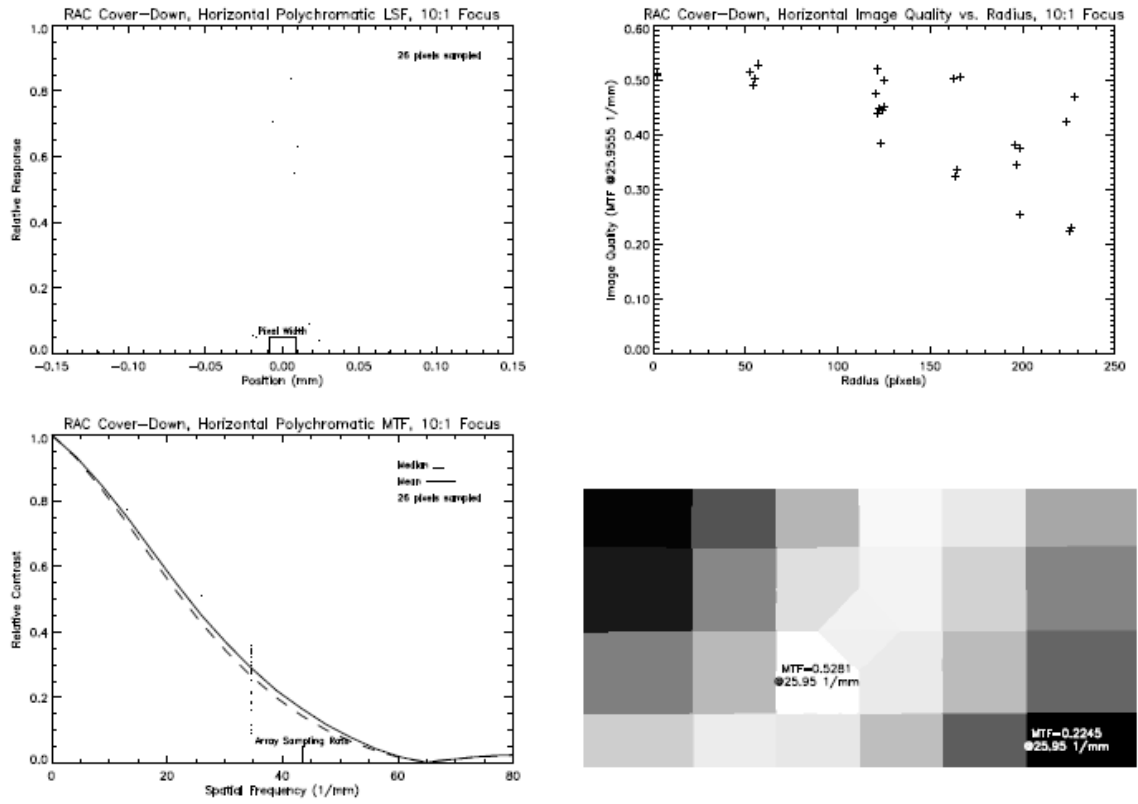
Figure 4.3.3.10 Horizontal MTF measurements at 10:1 focus (focus motor step 279) with RAC cover down.
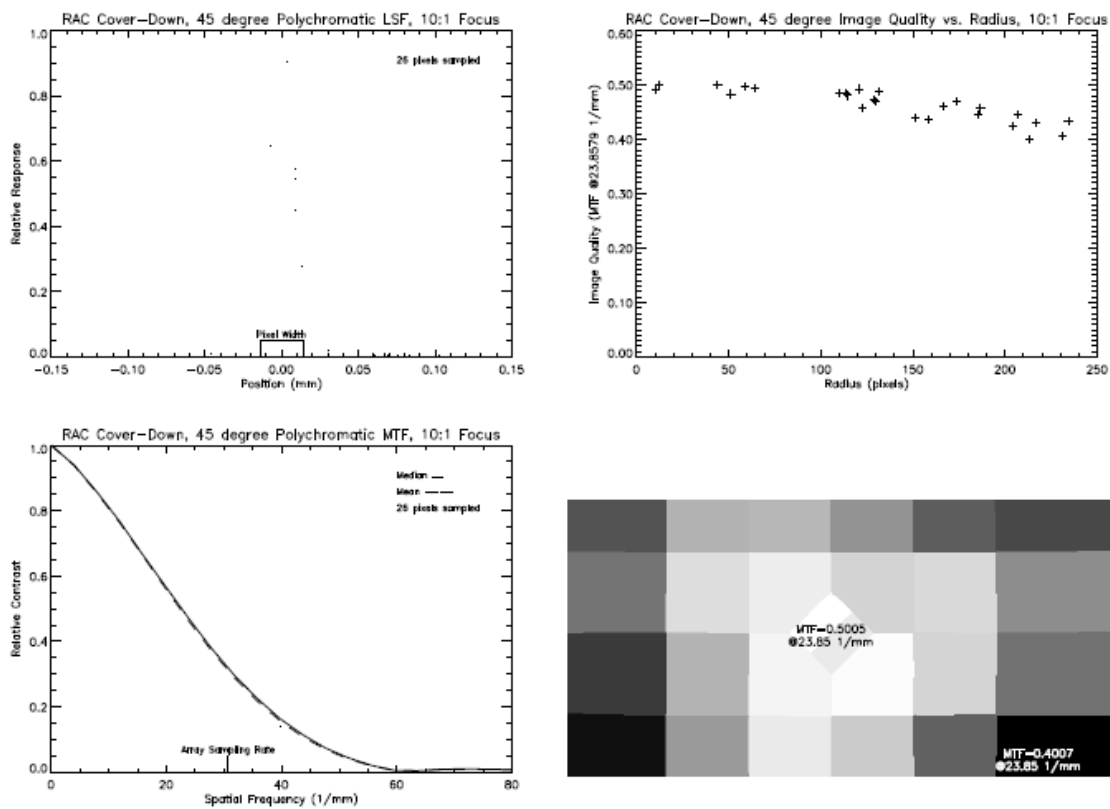
Figure 4.3.3.11 45° MTF measurements at 10:1 focus (focus motor step 279) with RAC cover down.
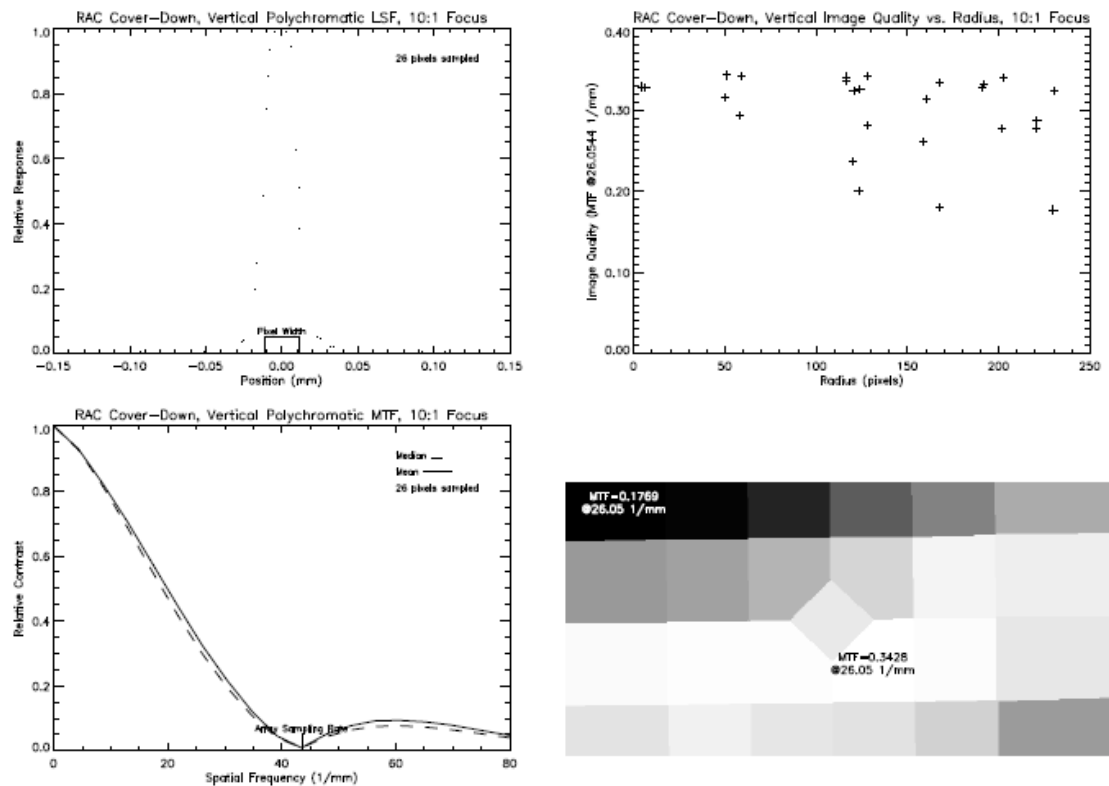
Figure 4.3.3.12 Vertical MTF measurements at 10:1 focus (focus motor step 279) with RAC cover down.

values: the DN offset value subtracted from the raw LSF data and the use of finite size slits. The effect of finite size slits is pretty easy to quantify. For both imaging conditions, the width of the slit image was approximately 2.3 μm. The Fourier transform of a 2.3 μm wide slit function reveals that a slit of this size decreases the measured MTF by 0.59% at 26 1/mm, 1.6% at 43.5 1/mm, and 2.2% at 50 1/mm.

The error introduced by the DN offset value is slightly more difficult to quantify. Unlike the error caused by a finite width slit, the wrong DN offset value can cause us to underestimate or overestimate the MTF. The Fourier transform of a DN offset is a delta function. So a DN offset error propagates into the MTF measurement by increasing the MTF only at $\xi = 0$. This results in a uniform percent error at all other frequencies when the MTF is normalized.

To better understand the amount of error that might be present in the MTF results due to the choice of offset values, we first looked at how much more the MTF's could be improved if the smallest DN value in each LSF was used as the offset. For 1:1 imaging the typical improvement was approximately 2%, for 10:1 1%. Then to get an idea of how much worse the MTF's could be we: calculated the standard deviation of the potential DN offsets, multiplied the standard deviation by 2, and then added that value to the DN offset originally used. This analysis revealed a typical MTF reduction of 3% for 1:1 imaging and 2% for 10:1 imaging. Combining these results with the finite slit width analysis we believe the MTF uncertainty is –1.5 to 3.6% for 1:1 imaging and -0.5% to 2.5% for 10:1 imaging. The 1:1 MTF results are less accurate than the 10:1 due to the presence of more stray light.

The MTF testing results are somewhat surprising based on what we have seen with the IMP and MPL SSI cameras. The spread in the data is unexpected and had not been predicted by the lens design; a drop in MTF of approximately 5-15% from the array center to the corners for 10:1 imaging was the most expected. The testing shows decreases of 20-60%. In addition, image quality is not symmetric about the array center. A peculiar effect seen in all the test set-ups is that in the horizontal and vertical directions the upper left and lower right corners of the image have dramatically lower MTF values than the other two corners of the image. But the 45° MTF results show less spread and the upper left and lower right corners go from having the lowest image quality to having slightly higher image quality than the other two corners. We will cover the causes of this effect in the next section of this report.

Another interesting MTF testing result is that the use of the RAC cover does effect image quality. The data shows a peak MTF drop of 1.4-35.9% for 1:1 imaging when the cover is down and a 0.5-3.5% drop for 10:1 imaging. This result is not surprising since a parallel plate of glass introduced into a diverging beam will produce spherical aberration. It is also not surprising that the effect is dependent on the type of imaging. For 1:1 imaging the beam diverges more than it does with 10:1 imaging so the degradation should be more pronounced for 1:1 imaging. So we recommend taking images with the RAC cover-up whenever possible to acquire the highest quality images. The only imaging situation where the cover should not have an effect on resolution is when imaging objects at infinity (focus motor step 312).

The 10:1 imaging, vertical slice LSF plots show a feature of interest. The LSF

data dips in the center. This phenomenon is also seen in the IMP and SSI MTF data reductions. We believe it is caused by a strip of material laid down horizontally on the array pixels which reduces transmission slightly. This is not seen in the 1:1 imaging data because the blur caused by the lens point spread function is large enough to hide the effect. This is consistent with the MTF testing results which shows the 1:1 imaging resolution is not quite as high as the 10:1.

The final item we would like to highlight is that the MTF testing reveals that during use, the RAC will provide maximum, and nearly constant resolution in a 256 pixel diameter area centered on the array center. So the robot arm should position the RAC such that objects of interest fall on the center of the RAC detector array to achieve maximum resolution.

4.3.4 Cause of Camera Resolution Variability

As described in the previous section, the variability in image quality across the RAC's field of view is unexpected and not the design intent. The non-symmetry seen in the array corners is also troubling. In order to better understand what might be causing such behavior, we decided to investigate the matter further. We wanted to determine if there was an error in the experimental set-up, a problem with the RAC design, or something wrong with this particular RAC.

The first step in our analysis was to revisit the Mars Polar Lander RAC MTF test data. The MPL RAC resolution should be comparable to the new RAC's because their optical designs were identical. The MPL RAC MTF data had been analyzed previously

37

but large variability in image quality was not noticed. To see if our original analysis had

missed anything we decided to re-reduce the MPL RAC data with the new code

rac01_mtf.pro, that we are currently using.
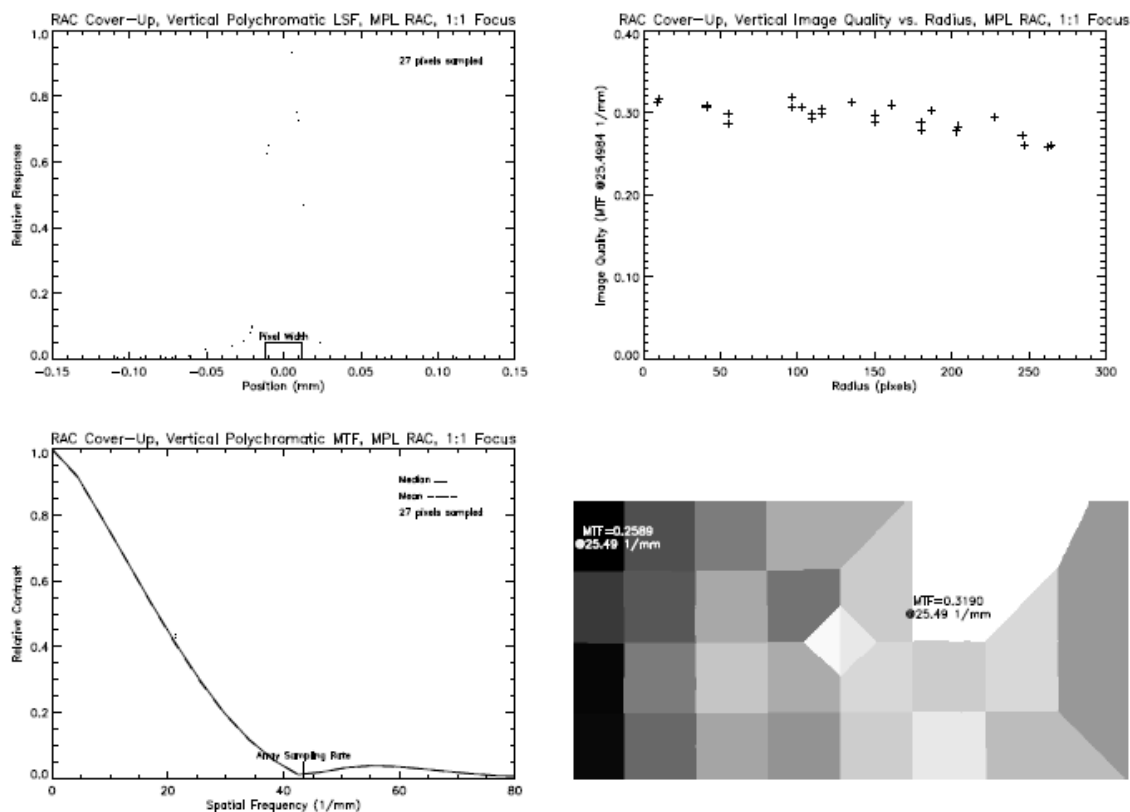
Figure 4.3.4.1 Mars Polar Lander RAC Vertical MTF measurements at 1:1 focus (focus motor step 0) with RAC cover up.

The new MPL RAC MTF analysis does not show the same resolution variability

as the current RAC's. Figure 4.3.4.1 shows an example of the analysis for one

configuration: 1:1 imaging, cover up, vertical MTF. The non-symmetric array corner

effect is not seen in the MPL RAC data and neither is the large variability. The image

quality variation is also in better agreement with the nominal design.

This analysis leads us to believe that the current RAC MTF effects are not

inherent to the RAC design nor are they caused by the MTF test set-up or test personnel –

they were essentially the same for each camera. Given this result, we decided to research

the RAC lens optical design and see what variations in its parameters might cause the

measured effects.

The nominal RAC lens design used in our investigation is shown in Table 4.3.4.1.

We chose to model the 10:1 imaging condition since the effects of interest were most

apparent for that condition. We input this design into the lens design program *Zemax EE*

(9.0) from Focus Software Inc. This program is an easy to use but powerful optical

design and analysis tool. It was essential to our research of the RAC MTF behavior.

Surface	Comment	Radius of Curvature	Thickness	Glass	Diameter
Object	Object	Infinity	99.52		
1	BG40 Window	Infinity	2.06	1.5300,62	28.92892
2		Infinity	21.96406		27.61995
3	1st Lens Element	2.986049	.58641	SK4	2.746358
4		10.33426	.097735		2.409462
5	2nd Lens Element	4.660773	.488675	F4	2.136979
6		2.248062	.5891555		1.547554
Stop		Infinity	.4662385		0.889
7	3rd Lens Element	-2.568266	.488675	F4	1.387797
8		-5.581931	.097735		1.908409
9	4th Lens Element	-25.37031	.58641	SK4	2.161948
10	Lens to CCD	-3.431573	12.03741		2.497242
Image		Infinity			

Table 4.3.4.1 Nominal 10:1 imaging, RAC lens design (all dimensions in mm).

The MTF testing results show that RAC resolution is not symmetrical about the

center of the detector array. Since the RAC lens is designed to be rotationally symmetric,

we tried to envision the most likely scenarios that would destroy the optics' rotational

symmetry. One idea is that it might be feasible for there to be a small relative tilt between the RAC lens and detector array. We also feel it is possible that the RAC lens elements may be tilted relative to each other. These two situations are deemed the most likely. We also considered the possibility that individual lens surface tilts and decenters could be causing the RAC's MTF behavior. This effect is not deemed as probable, however, given the manufacturing tolerances that are standard in the industry.

We examine the effects of a tilt between the RAC lens and array by inputting the design in Table 4.3.4.1 into *Zemax* and inserting coordinate break surfaces into the design. The coordinate break surfaces allow the lens to be tilted in any orientation relative to the array. The diagonal between the two array corners which exhibit high horizontal and vertical MTF values makes a 26.52° angle with horizontal. So we orientate our axis of rotation to be parallel to that. Then we input various rotation angles and calculate lens MTF's to see if the effects we are looking for are there. We find that the design is quite resilient to this type of error. A tilt greater than 3° is required to cause any noticeable change in MTF. Tilts of 4-6° do cause greater degradation in resolution but the effects do not mimic the MTF testing: the point spread functions in the array corners remain quite symmetrical, the MTF values at the poor performing corners are not dramatically lower than those found in the good corners, and the reversal of effect at 45° does not occur. In general, the tilts between the lens cell and the array that we investigated appeared to primarily have the effect of simply defocusing the image in the poor corners. In addition, we are quite confident that a relative tilt between the lens cell and detector array greater than 3° could not have gone unnoticed during the camera

assembly. This leads us to believe that relative tilt between the RAC lens cell and the array is not the cause of the MTF performance measured.

The tilting of lens elements relative to each other is the other likely scenario that we decided to investigate with the *Zemax* lens model. Again, coordinate breaks are inserted into the lens prescription of Table 4.3.4.1. This enables each of the four lenses to tilt about an axis located at their first surfaces. The rotation axis at each element is allowed to rotate about the optical axis. By inputting different tilt angles into this model we discovered that it is possible to mimic most of the MTF testing results.

Given the preliminary encouraging results of this model we proceeded with a full search of the solution space. We do this by making the rotation axis angle and tilt angle of each element an independent variable in the model. Then we create a custom merit function where the optimization parameters are the ratios of various MTF values that we had measured. We are forced to optimize on MTF ratios because *Zemax* cannot currently include the effects of the pixel width and other factors that when multiplied with the lens MTF produce the final system MTF. By using MTF ratios we eliminate the need for this multiplication factor. Also included in the merit function is a weighting of the tilt angles to make them be as small as possible while still reproducing the MTF results. And finally we force *Zemax* to adjust the object space heights so that the light rays fall on the same location on the array independent of the tilt parameters.

We optimize the *Zemax* lens simulation using 9, equally weighted MTF ratios at a spatial frequency of 26 1/mm. The target MTF ratios are computed from the MTF measurements. The MTF calculations are made at the array center (0,0), at the low MTF

array corner (4.6268 mm, -2.6028 mm), and at the high MTF array corner

(-4.2052 mm, -2.6872 mm). These corner locations are chosen to represent the average

locations of the corners measured since the actual MTF tests do not always sample the

same pixel.   The polychromatic MTF calculations are computed using 7 wavelengths

equally spaced from 400 to 700 nm, weighted with the theoretical response of the RAC

camera to a tungsten-halogen lamp.

Optimizing the *Zemax* model to find the target MTF ratios takes a considerable

amount of computing time. Running on a Pentium III PC, it takes *Zemax's* standard

optimization routine over 19 hours to find the tilts that best reproduce the measured MTF

ratios. In addition to this we run Zemax's various global optimization routines for over

48 more total hours. The best solution we find is presented in Table 4.3.4.2.

Lens Element	Rotation Axis Orientation Relative to Horizontal	Tilt Angle
1	45.580374°	0.390631°
2	47.649355°	-0.460789°
3	47.403576°	-0.355370°
4	46.398272°	0.282789°

**Table 4.3.4.2 Element tilt angles for the Zemax, RAC lens model
which best fit the experimental MTF results.**

The first result from the modelling we notice is that the orientation of the rotation

axes are the same for each element. This leads us to consider the possibility that similar

results might be obtained if only one element was allowed to tilt in the model. Modelling

that scenario does prove this out, although tilts on the order of 0.7-2.0° are required when

only one element is allowed to tilt. So, the orientation listed in Table 4.3.4.2 certainly is

not the only model configuration that well-matches the measured MTF results. But this

model is the one that best reproduces the MTF measurements with the smallest amount of

individual element tilt. Figure 4.3.4.1 presents the same type of image quality plots as

shown in Fig. 4.3.3.1-4.3.3.12. Comparison of the image quality pictures in Fig. 4.3.4.1

to those in Fig. 4.3.3.7 and Fig. 4.3.3.9 demonstrates that the tilted lens model is a good

fit. The actual MTF numbers do not agree with the measurements because *Zemax* can

only model the lens effect but the relative behavior matches very well.
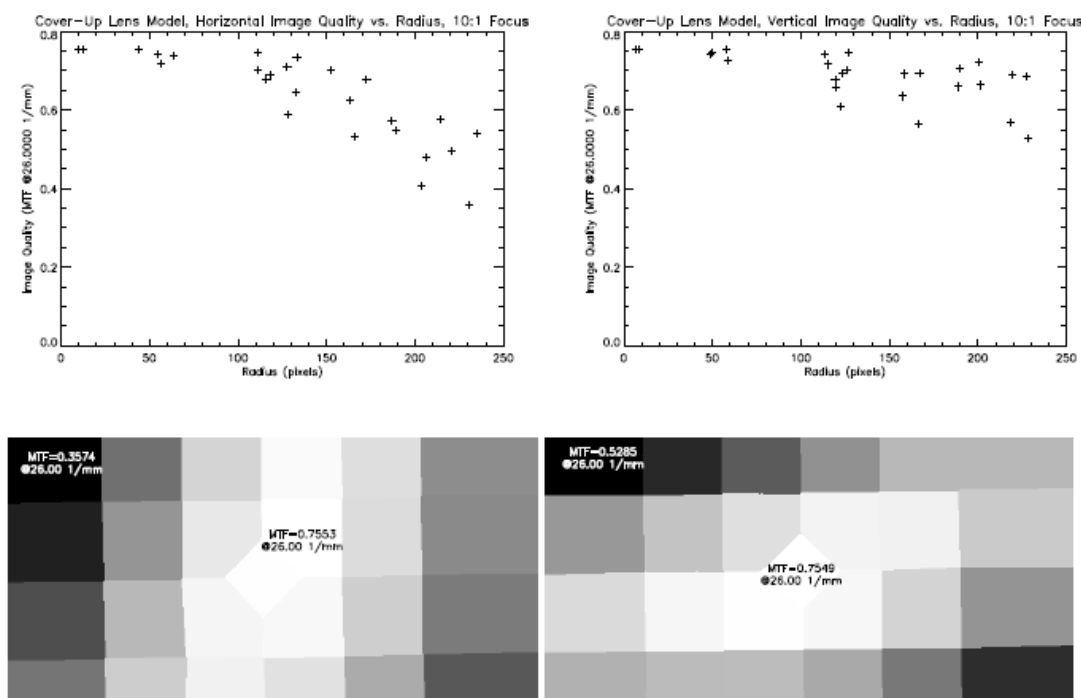
Figure 4.3.4.1 Image quality results from the Zemax tilted elements lens model.

To help better visualize what kind of point spread function (PSF) would cause the rather peculiar MTF behavior, we calculate the lens PSF's using the tilted elements Zemax lens model. These PSF's are shown in Figure 4.3.4.2.
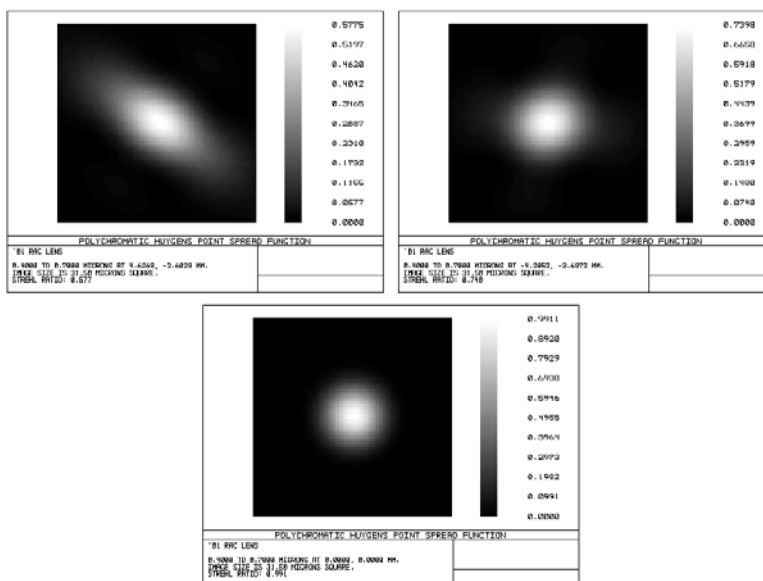
Figure 4.3.4.2 Lens PSF's calculated with the Zemax tilted elements lens model. The upper left plot was the calculation at the low MTF corner, the upper right the high MTF corner and on bottom the on-axis PSF.

Examination of the PSF images reveals what is causing the measured MTF behavior. The PSF in the low horizontal and vertical MTF corner is strongly asymmetric whereas the PSF in the other corner is symmetrical. When a slit is scanned in the horizontal or vertical direction across the asymmetric PSF, the long diagonal extent of the PSF causes the MTF to be low in that corner. But a slit scanned at 45°, lower left to upper right, in the same corner will encounter an effective PSF width that is slightly less than the width at the other corner. This causes the MTF in the asymmetric PSF corner to

be better than the MTF in the other corner. It is interesting to note that if the MTF test had scanned the slits at 45° in the other orientation (lower right to upper left), then the 45° test results would have shown the MTF in the asymmetric PSF corner to be substantially lower than the MTF at the other corner. We should note that even though we only show the PSF's for two of the corners, the PSF's are similarly shaped in the other two corners.

Another item to notice from the Zemax lens model is that even with all of the element tilt in the system, the on-axis PSF still has a Strehl ratio of 0.991. So the on-axis resolution is essentially diffraction limited which is rather surprising. So even if the lens vendor would have measured the lens performance on-axis using an interferometer or similar instrument, no problems would have been detected.

So based on our lens simulation activities we conclude that the unusual MTF performance measured is physically possible and due to the presence of one or more lens element tilts within the four-element RAC lens. Although the element tilts used in the final Zemax lens model are an order of magnitude larger than the typical industry standard (*Shannon* 1997), we believe that due to the small size of the RAC lenses, that larger than typical element tilts are feasible. In fact, the lens manufacturer Applied Image Group/Optics (Tucson, Arizona) believes they can only hold an element tilt tolerance of ±0.2° on their miniature lenses (*personal communication* 2000). Its easy to see why it might be difficult to hold such small lens element tilts tighter. Lens element 4 has the largest lens clear aperture diameter of 2.746 mm according to Table 4.3.4.1. Rounding this up to 3.0 mm and using the lens model's element 1 tilt angle of 0.3906° we find that a

bump, a speck of dust, or some other foreign object on the lens spacer only 20.5 μm thick

could cause the amount of tilt required!

4.3.5 Recommendations for Future Work

Based upon our results and analysis of the RAC MTF, we believe that it would be

beneficial to return the robotic arm camera to the MAGI team at the University of

Arizona so that the MTF performance in the corners of the field can be further critiqued.

Before performing any disassembly we would measure the MTF at 45° in the other

orientation to test the lens model prediction. The extra data could be used to further

refine the lens model.

The RAC MTF data allows the instrument's users to know what the resolving

capabilities of the camera are and how it will image various scenes. But correcting RAC

images using the MTF information directly is not possible. To correct images with the

highest accuracy, the RAC's two-dimensional point spread function (PSF) must be

known. There are several methods the MAGI team is currently considering to convert

the measured MTF profiles into a useful RAC PSF model for deconvolution. Given the

high number of variables in the problem we will be unable to create a simple model

similar to the one we currently use for IMP images (*Reid et al.*,1999). The RAC's 313

focus motor positions will require the PSF model to change with focus. The RAC lens

element tilts will require the PSF model to also be a function of horizontal and vertical

position on the array. And since the PSF is not isoplanatic, a specialized deconvolution

technique will be required. Our current best thought is to invoke the central limit

theorem (*Frieden*, 1983) and model the lens PSF separately as a Gaussian function that is dependent on position and then convolve it with a 17 x 23 μm rectangle function. But more thought will have to go into this activity so that the final product will be as convenient to use as possible.

5.0 Responsivity

5.1 Overview

The RAC camera's raw output has an intensity resolution of 12 bits. So the output from any single pixel lies in the 0-4095 DN range. The raw DN values in a RAC image, though, need to be corrected because they not only depend on an object's radiance but are also sensitive to temperature, image location, dark current, focus position and image readout. In order to convert RAC image DN values into radiometric units, all aspects of the RAC's responsivity were studied by the MAGI calibration team.

The final DN value in a RAC image is affected by many variables. The components of a pixel's DN value located at (i,j) are

$$DN_{i,j} = DN_{Offset} + R_{i,j} L_{i,j} t_{exp} + \frac{t_S}{256} \sum_{k=1}^{j} (R_{i,k-1}, L_{i,k-1} + Dark_{i,k-1})$$

$$+ Dark_{i,j} t_{exp} + t_{AD} \sum_{k=0}^{j} DarkST_{i,k} + \frac{t_{AD}}{256} \sum_{k=i-511}^{0} DarkR_k , \qquad (5.1.1)$$

where DN_{Offset} is the hardware offset value which is temperature dependant, $R_{i,j}$ is the

pixel responsivity which is temperature dependant, $L_{i,j}$ is the radiance of the object, $Dark_{i,j}$ is the signal contributed by the image pixels' dark current, t_{exp} is the exposure time, t_s is the total time to shift the image to the storage array (~0.5 ms), t_{AD} is the time to read out one row of pixels (~8.2 ms), DarkST is the signal contributed by the storage array's dark current and DarkR is the signal contributed by the horizontal shift register's dark current. All the dark current terms are temperature dependent. For scientific analysis the term of interest is $L_{i,j}$. Converting RAC output to $L_{i,j}$ is the subject of this section of the report.

Based on our experience with the IMP, SSI and other cameras, we have found that "shutter correcting" images immediately is the first, most important step in correcting RAC images. We do this by taking a "shutter image" immediately after an image is exposed and subtracting the shutter image from the actual image. A shutter image is a normal image with a 0 s. exposure time. Thus, the DN values of a shutter image consist of

$$DN_{i,j} = DN_{Offset} + \frac{t_S}{256} \sum_{k=1}^{j} (R_{i,k-1}, L_{i,k-1} + Dark_{i,k-1})$$
$$+ t_{AD} \sum_{k=0}^{j} DarkST_{i,k} + \frac{t_{AD}}{256} \sum_{k=i-511}^{0} DarkR_k , \qquad (5.1.2)$$

and subtracting this from Eq. (5.1.1) results in

$$DN_{i,j} = \mathcal{R}_{i,j} L_{i,j} t_{exp} + Dark_{i,j} t_{exp} , \qquad (5.1.3)$$

for the shutter corrected image. Eq. (5.1.2) illustrates why it is so important to shutter correct an image immediately. A shutter image is scene dependent. It depends on $L_{i,j}$.

The next step in correcting an image is to subtract a shutter corrected dark frame. A dark frame is a normal image taken when no light is falling on the detector. Its pixels' values depend on

$$DN_{i,j} = DN_{Offset} + \frac{t_S}{256} \sum_{k=1}^{j} Dark_{i,k-1} + Dark_{i,j} t_{exp}$$
$$+ t_{AD} \sum_{k=0}^{j} DarkST_{i,k} + \frac{t_{AD}}{256} \sum_{k=i-511}^{0} DarkR_k , \qquad (5.1.4)$$

and if the dark image is shutter corrected the dark image values are

$$DN_{i,j} = Dark_{i,j} t_{exp} \qquad\qquad (5.1.5).$$

And so, finally, if we subtract a shutter corrected dark frame, Eq. (5.1.5), from a shutter corrected image, Eq. (5.1.3), we get

$$DN_{i,j} = \mathcal{R}_{i,j} L_{i,j} t_{exp} \qquad\qquad (5.1.6).$$

The exposure time, t_{exp}, is known and so the final step in determining the object's $L_{i,j}$ is dividing $DN_{i,j}$ by $\mathcal{R}_{i,j}$. Notice that the shutter corrected dark does not need to be taken at

the same time as the image. It does not depend on the scene. In fact, on the Martian

surface RAC dark frames will not be able to be acquired for most situations and so

laboratory dark measurements will be required to perform data correction.

5.2 Relative Spectral Response

As previously stated, the RAC is a broadband instrument. The RAC can only

create a color image if the ambient light is low and the RAC's red, green and blue LED's

illuminate the object of interest. Since RAC responsivity at various narrow wavelength

bands was not measured as it was for the IMP and SSI, we calculate the spectral response

based on the detector array's quantum efficiency measured at MPAe (*Hartwig* 1998) and

the theoretical relative transmission of the BG40 filter glass. The results of this
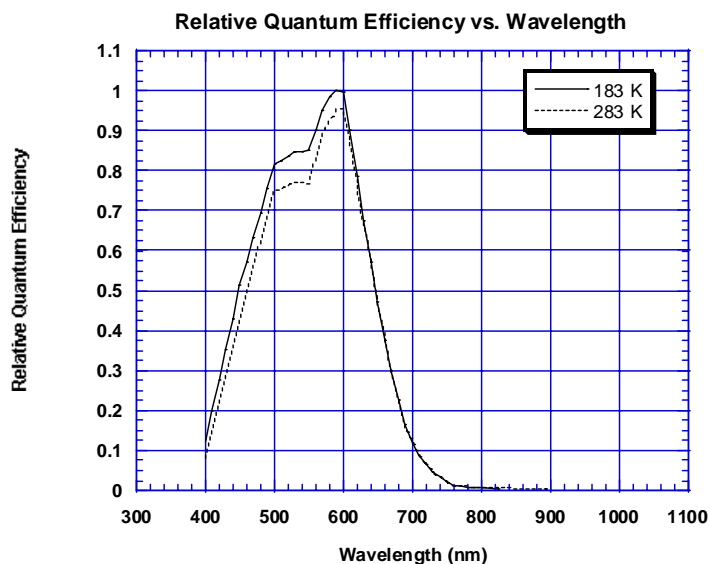
Figure 5.2.1 RAC calculated normalized responsivity.

calculation are shown in Figure 5.2.1.

The responsivity curves in Fig. 5.2.1 demonstrate that the RAC responsivity is a function of both wavelength and temperature. The camera's responsivity is higher at low temperatures than at high temperatures. And the RAC is only sensitive to light from 400-700 nm due to the BG40 filter glass cut-off.

5.3 Absolute Responsivity

5.3.1 Experimental Set-Up

Absolute responsivity calibration is the determination of how the robotic arm camera responds to a known amount of light – the determination of $R_{i,j}$. To perform this measurement we use the experimental arrangement shown in Figure 5.3.1.1.

The RAC is placed inside a vacuum chamber and the chamber pressure is vacuum pumped down to approximately 1×10^{-4} Torr or less. Camera temperature is controlled through contact with a cold plate whose temperature is varied from -115° C to 30° C.

The camera is positioned so that the reflectance panel can be seen through the anti-reflection coated chamber window. The reflectance panel is located inside a light box that has been painted flat black. It is illuminated by a spectral irradiance standard lamp (Oriel Instruments #63355, serial number 5-139) located 0.500 m away. The panel and lamp are mounted on a common machined fixture so that the distance is known accurately. The test proceeds by bringing the RAC to the desired equilibrium temperature and taking shutter corrected images of the illuminated reflectance panel at focus motor step 306. Then a removable light baffle is put into position that just shadows the reflectance panel from the standard lamp and more images are taken. This step is
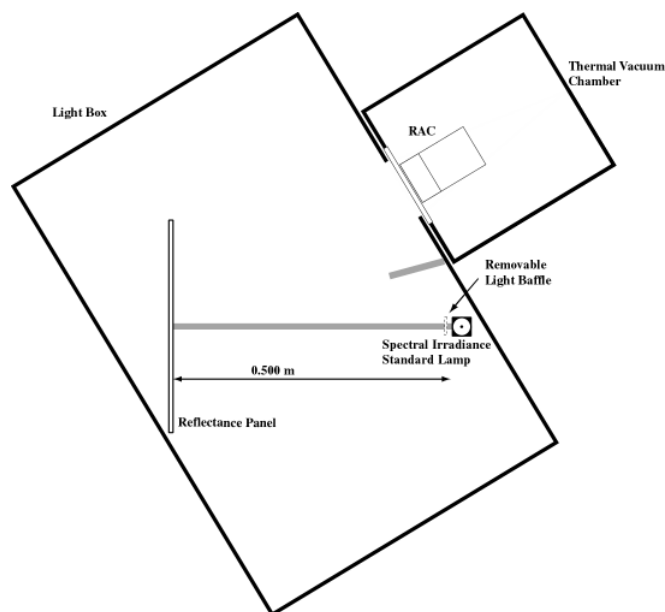
Figure 5.3.1.1 RAC absolute responsivity experimental set-up schematic.

required so that during data reduction, the signal caused by the multiple reflections that

occur inside the light box can be removed from the data.

5.3.2 Temperature monitoring

The RAC has three temperature sensors incorporated into it. One is located on

the CCD chip and the other two are bonded to the rear body of the driver motors. During

the absolute radiometry calibration testing, the RAC CCD temperature in DN was read

out to the "H_CCDTEMP_R" location in the image headers. The conversion of these

counts into Kelvins is 0.083 K/DN.

All three temperature sensors were AD590 two-terminal integrated circuit

temperature transducers from Analog Devices (Norwood, Massachusetts). Each of these

sensors was laser trimmed to achieve a ±0.5° C calibration accuracy over the range –55°

C to 150° C. Since the absolute responsivity testing went below –55° C, we decided to

investigate their linearity throughout our full test range.

During the absolute responsivity testing, not only was the RAC CCD temperature

being read-out from the AD590, but the output from RTD's located at various positions

on the RAC and vacuum chamber were being recorded in the lab book as well. So to

check the accuracy of the integrated CCD temperature sensor over the extended

temperature range, we compared its readings to the measurements recorded with the

sensor at the RAC rear bulkhead. Typically only one rear bulkhead temperature was

recorded per test but when more than one was available their values were averaged.

Figure 5.3.2.1 summarizes the results of the evaluation. As one would expect, no

differences are seen between the cover up and cover down conditions. The linear fit

including all 60 data points represents the data well as does the fit that only includes

temperatures within the -55° C to 150° C range. The fits consistently show that a

temperature offset of 0.71° C exists between the RAC rear bulkhead temperature and the

CCD temperature. The slopes for the two fits also agree with each other to better than

0.5%. So we see no reason to suspect that the recorded CCD temperatures below -55° C

contain any gross error.
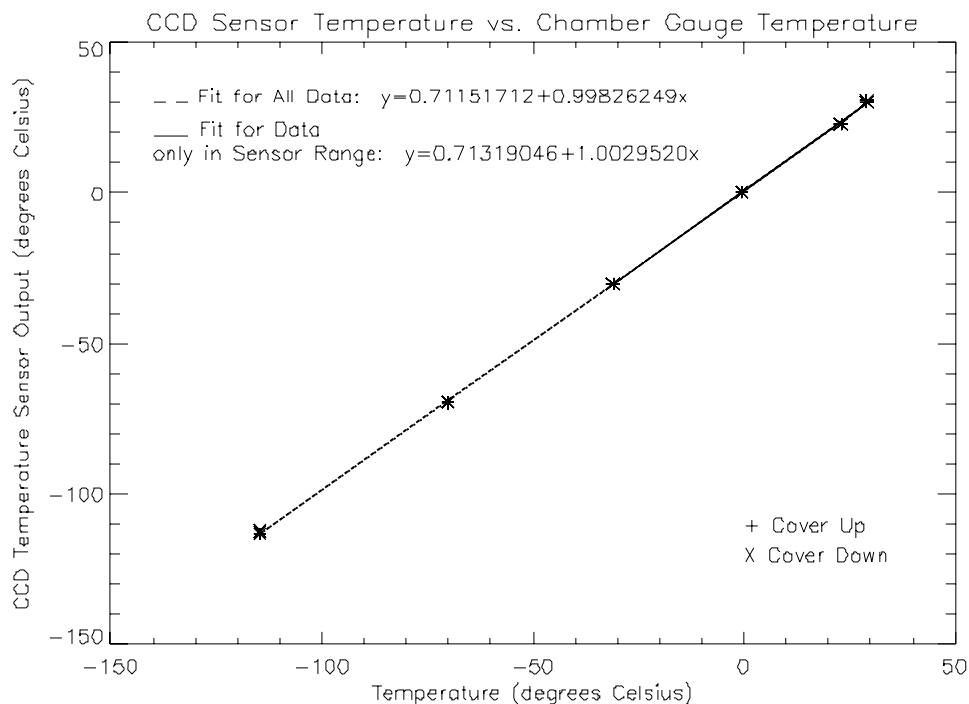
Figure 5.3.2.1 Comparison of the CCD temperature sensor measurement and the temperature recorded at the RAC rear bulkhead.

5.3.3 Data Reduction

Turning the images acquired using the set-up shown in Fig. 5.3.1.1 into absolute responsivity results requires several steps. The first step is to examine each image using IDL and determine where the brightest points in the image are located by utilizing IDL's *profiles* function. The intent of the experimental set-up is to center the reflectance panel in the RAC's field of view. This is difficult to do so some variation from the RAC's center should be expected and requires checking. Our analysis determined that the panel was centered at pixel location (265.5, 188.5) instead of (255.5, 127.5).

The next step in the analysis is to remove the multiple reflection effects for each RAC CCD temperature measured. So the DN at each pixel in a 10x10 pixel square centered at (265.5, 188.5) is averaged over the number of exposures taken when the reflectance panel is in shadow. Then these average DN values are subtracted from the same 10x10 pixel square DN image values when the reflectance panel is fully illuminated. Since both image types were immediately shutter corrected, the subtraction of the blocked values from the unblocked values produces DN values that only depend on $R_{i,j}$, $L_{i,j}$ and t_{exp} as shown in Eq. (5.1.3).

The next step in the reduction is to divide the reflection corrected, mean DN values of the 10x10 pixel blocks by the proper exposure time, t_{exp}. The exposure time in seconds at each temperature was read out to the "H_EXPTIME" location in the RAC image headers during the test so those values are read directly from the image header.

Next we need to determine the correction factor to account for the light loss due to the RAC looking through the chamber window and then multiply the DN/s values by it. The correction factor is determined by: dividing the mean DN/s found at room temperature with the chamber open, by the mean DN/s found at room temperature with the chamber closed for the group of 10x10 pixels centered at (265.5, 188.5). We calculate the correction factor to be 1.025036 when the RAC cover is up and 1.025033 when the cover is down. These values indicate that the vacuum chamber window had a transmittance of 0.976. A transmittance of this value is consistent with a window containing an anti-reflection coating on both sides.

The final step in determining $R_{i,j}$ is to calculate $L_{i,j}$, the spectral radiance of the

reflectance panel image. We calculate this value with the use of Equation (5.3.3.1)

$$L = \frac{\rho E}{\pi} \, , \qquad\qquad (5.3.3.1)$$

where r is the reflectance panel hemispherical reflectivity and E is the standard lamp's spectral irradiance. At 600 nm, $E = 31.51$ W/m^2/μm and $r = 0.991$ which results in $L = 9.948$ W/m^2/ster/μm. This spectral radiance value is actually the spectral radiance at the brightest point on the panel, so $L_{265.5,188.5} = 9.948$ W/m^2/ster/μm. And so the responsivity is defined to be

$$R_{i,j} \equiv \frac{DN_{i,j}/t_{exp}}{L_{i,j}} \qquad\qquad (5.3.3.2).$$

Notice that the responsivity units are in DN/s/W/m^2/ster/μm which is a different type of responsivity than most engineers are familiar with, typically the per μm term would be integrated out. We report responsivity in this way for two reasons: first, it allows RAC data users to easily calculate object spectral radiances by using the simple scale factor, R, no knowledge of the RAC system's spectral response is required and no integrations are necessary; and second, only values that can be known directly from laboratory measurements are required to go in to the calculation.

5.3.4 Results

Figure 5.3.4.1 shows the absolute responsivity final test results. The test results
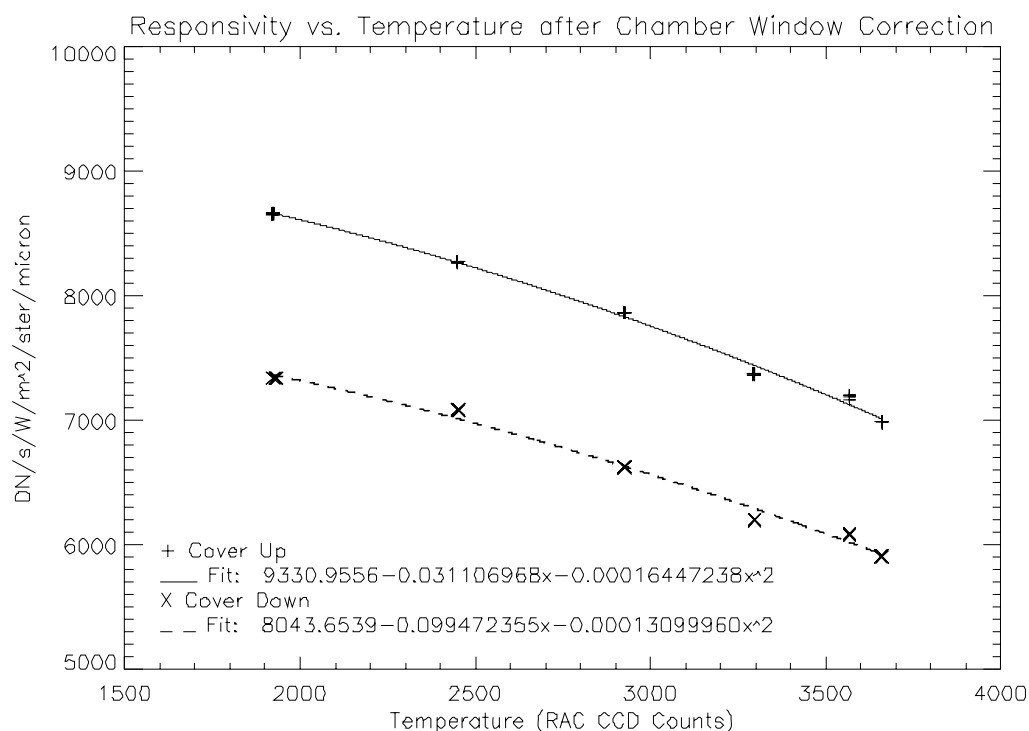
Figure 5.3.4.1 Responsivity of the RAC camera at 600 nm as a function of temperature.

clearly show that the RAC responsivity is a function of temperature. The amount of

change in responsivity with temperature is primarily due to two effects: the temperature

dependence of the photoelectron to voltage conversion efficiency and the change in

quantum efficiency with temperature as shown in Fig. 5.2.1. According to data provided

by the Max-Planck-Institut für Aeronomie, the biggest cause of the effect is the change in

photoelectron to voltage conversion. It goes down 7% from 183 to 283 K. While over

the same temperature interval the array responsivity only goes down 4.5% (Max-Planck-Institut für Aeronomie 1999). Taking these two effects into account together results in an expected responsivity drop of 11.7% from 183 to 193 K. This is consistent with the 12.0% drop measured for the cover-up condition and the 12.5% drop for the cover-down condition.

Following the method used for the IMP and SSI calibrations we fit a second order polynomial to the responsivity versus temperature data as shown in Fig. 5.3.4.1. The cover-up fit is

$$R_{265.5,\,188.5}(T) = 9331.0 - 0.031107\,T - 0.00016447\,T^2, \qquad (5.3.4.1)$$

and the cover-down fit is

$$R_{265.5,\,188.5}(T) = 8043.7 - 0.099472\,T - 0.00013100\,T^2, \qquad (5.3.4.2)$$

where T is in RAC CCD temperature sensor counts (0-4095) and $R_{265.5,\,188.5}$ is the responsivity in DN/s/W/m^2/ster/μm at 600 nm, at RAC focus step 306 and at pixel position (265.5, 188.5) on the array. This array location refers to the position in the image after it is manipulated so that the image is upright and right-handed. In this configuration, position (0, 0) is in the lower left corner of the image and the image runs to (511, 255). For T = 3290.96 counts, which corresponds to 0° C, $R_{265.5,\,188.5}$ = 7,447.3 DN/s/W/m^2/ster/μm. This is 12.6 times larger than the IMP (*Reid et al.*, 1999)

responsivity at the same temperature and wavelength. The dramatic difference in

sensitivity is due to the RAC's much larger bandpass and its faster optical system at focus

motor step 306.

Another useful application of the responsivity versus temperature data is

independent verification of the RAC's sapphire cover window transmission. The vendor

reported a constant transmission value in the RAC's bandpass of 0.845. To check this
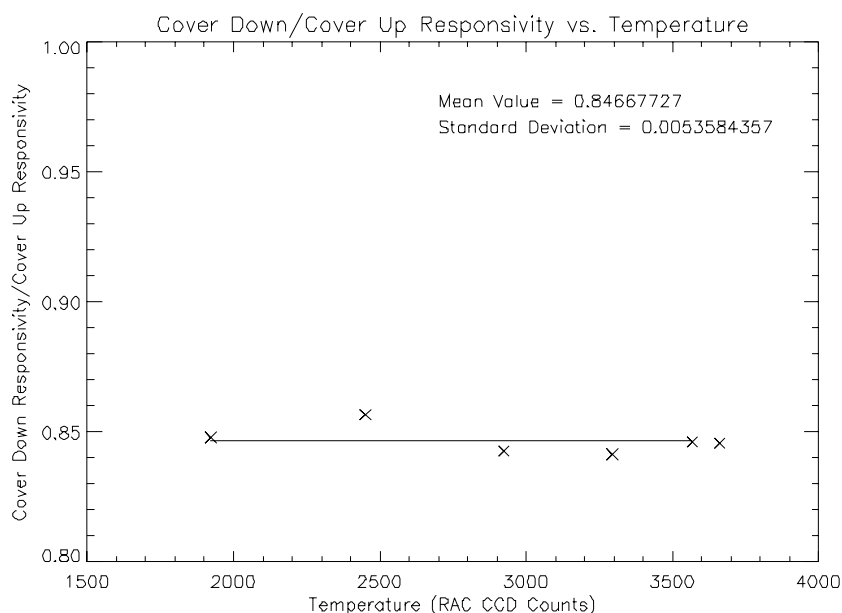
Figure 5.3.4.2 Transmission of the RAC's sapphire window cover versus temperature.

result we take the responsivity versus temperature data and calculate the mean

responsivity at each temperature for the cover-up and cover-down conditions. There are

typically 3 responsivity values at each temperature. Then the cover-down responsivities

are divided by the cover-up responsivities found at the same temperatures to determine

the window transmission. Finally, those 6 transmittance values are averaged together to find a window transmission of 0.8467, which agrees with the reported value to better than 0.25%. The results of this calculation are shown in Figure 5.3.4.2. As expected for a sapphire window, the results do not show a correlation between RAC cover transmittance and temperature.

5.3.5 Uncertainty

The major sources of error in the absolute responsivity results are the standard lamp irradiance calibration accuracy, the uncertainty in the distance between the standard lamp and the reflectance panel and the stray light due to multiple reflections within the light box. According to the Oriel calibration report for our lamp, the 2-sigma uncertainty in the lamp's irradiance calibration in the RAC's waveband is no worse than 1.85%. The uncertainty in the distance between the lamp and the reflectance panel is estimated to be ± 1 mm. Assuming a $1/r^2$ fall-off in irradiance with distance the uncertainty then in the irradiance at the panel 0.5 m away would be 1%.

The most difficult source of error to estimate is the extra light that falls on the reflectance panel due to multiple reflections within the light box. As mentioned earlier, this effect is partially removed by subtracting from the data an image that was exposed while the direct light that falls on the reflectance panel was blocked. This should account for most of the error but the method introduces a small error from the light that bounces off of the light blocker, reflects off the RAC and light box walls and falls back on to the reflectance panel. It also does not account for the light that reflects off the reflectance

panel, bounces around and again hits the reflectance panel during the unblocked imaging. The light blocker and the light box walls are painted flat black. We estimate that the reflectivity of the flat-black surfaces is no greater than 8%. The most direct route for light from the lamp to the reflectance panel when the light blocker is in place involves two reflections. So the maximum amount of light that could possibly make it to the reflectance panel after hitting the light blocker is only 0.49% of the light that can fall on it directly.

Taking all three of these sources of error into account and assuming the worst possible error stack-up we estimate the radiance at the reflectance panel can be known to ±3.5%. The second order polynomial responsivity versus temperature model agrees with all of the measured responsivities to better than ±1.5%. So if this value is used to estimate the uncertainty introduced by the model, we find that the absolute responsivity of the RAC at (265.5, 188.5) is known to ±5.0%. If one is only interested in relative accuracy, such as the ratio of two RAC measurements, than the RAC has an accuracy of better than ±0.5% due to detector noise. This conclusion is drawn from the results of the sapphire window transmission analysis.

An absolute radiometric accuracy of 5.0% is typical for an instrument like the RAC (*Palmer* 1996). However, this level of accuracy is only true when the RAC images objects with certain types of spectra. Due to the RAC's large system bandpass, approximately 171.9 nm at full-width half-maximum, the RAC's output can potentially be the same for a range of spectra with different radiances at 600 nm. To estimate how this effects potential Mars observations, we investigated the response of the RAC to a typical

Mars scene. We conducted this study using a mathematical model of the RAC's response.

The RAC's response to an object was modeled with Equation (5.3.5.1)

$$R = c \int \lambda \; QE \; T \; L_n \; d\lambda \qquad\qquad (5.3.5.1)$$

where R is the camera response in DN/s, c is a constant, l is wavelength, QE is the RAC detector quantum efficiency, T is the RAC filter window's relative transmission and L_n is the spectral radiance in terms of energy of the object, normalized to 1 at 600 nm. We input two different types of relative object spectra, L_n, into the model; the laboratory object spectrum and a typical Martian spectrum based on the reflectance of the rock Flat Top measured by the IMP at the Mars Pathfinder landing site. The laboratory spectra is easy to generate. It is simply the product of the standard lamp calibration curve and the panel reflectance. The Martian spectra is generated by multiplying Flat Top's reflectance by a standard solar spectrum (*Neckel and Labs* 1983). The two spectra are shown normalized to 1 at 600 nm in Figure 5.3.5.1.

In Figure 5.3.5.2 the integrands of Eq. (5.3.5.1) are shown at an array temperature of 183 K and 283 K. The difference in RAC response to the two types of spectra is due to the different areas below the curves. By numerically integrating the curves using five-point Newton-Cotes integration we find that the RAC's response at 183 K to a Martian spectrum will be 11.1% lower than the response to the laboratory spectrum with the same spectral radiance at 600 nm. The drop in response at 283 K would be 11.3%.

62
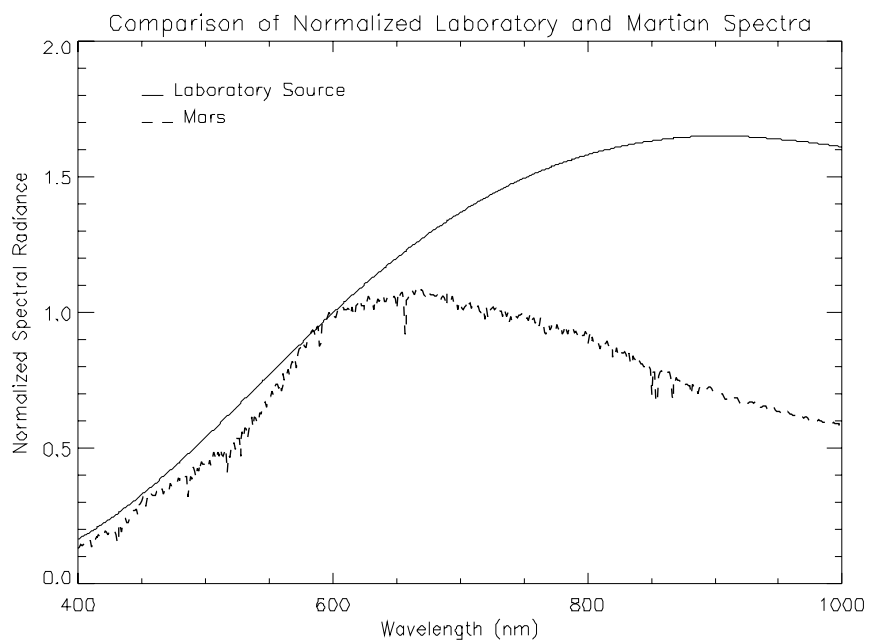
**Figure 5.3.5.1 Comparison of laboratory and Martian spectra
normalized to 1 at 600 nm.**
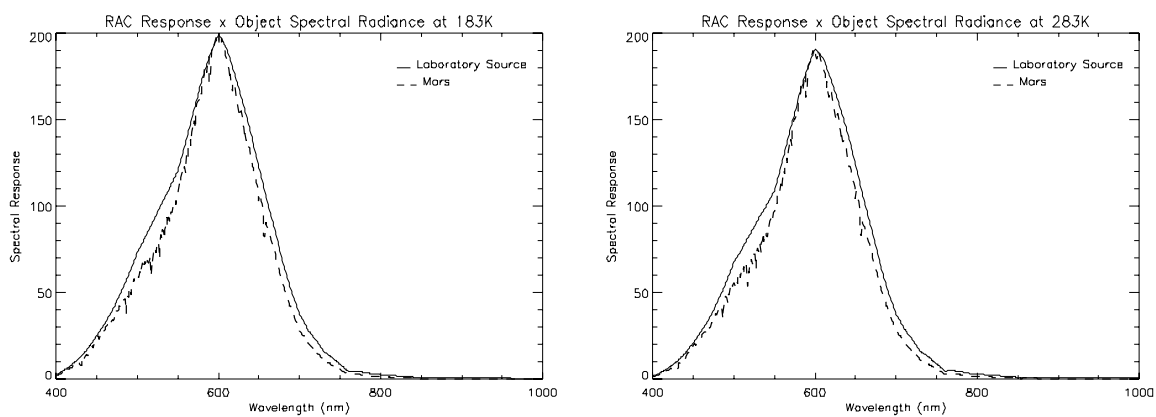
Figure 5.3.5.2 Plots of the integrands in Eq. (5.3.5.1) at 183 Kelvin and 283 Kelvin.

This result indicates that the ±5.0% uncertainty in the RAC's absolute responsivity may be several times greater than that when imaging on the Martian surface, unless the relative spectra of the objects being imaged are known. If the relative spectra of the Martian objects are known, then a correction factor can be applied to the RAC observations to keep the uncertainty on the order of 5%.

In order to further explore this source of potential radiometric error, we created several simulated Martian spectra and calculated the change in response relative to the laboratory spectra using Eq. (5.3.5.1). The simulated Martian spectra were based on deviations made to the laboratory spectrum. The simulated spectrum was made equal to 1.0 for wavelengths ≥600 nm. Below 600 nm the spectrum was simply the laboratory spectrum plus a 1/400 1/nm frequency sinusoid of varying amplitude which extended from 400 to 600 nm. Various spectra were input into Eq. (5.3.5.1) and their responses calculated. The slopes of the spectra at 550 nm were also monitored and recorded. The results of this study are shown in Figure 5.3.5.3. The simulation shows that the RAC response is sensitive to the slope at 550 nm of the simulated Martian spectra. The true Martian spectra derived from the reflectance of Flat Top has a slope at 550 nm of approximately 0.0069 1/nm. Using the plot in Fig. 5.3.5.3 we find a simulated Martian spectrum with that slope would result in a RAC response that is –17% lower than the laboratory response. This agrees approximately with the –11% error found using an actual Martian spectrum. Most of the 6% difference comes from making the simulated spectra equal to 1.0 for all wavelengths ≥600 nm. Changing the flat response to something else will move the line in Fig. 5.3.5.3 up or down, but will not change the

Difference in RAC Response vs. Martian Model Spectra
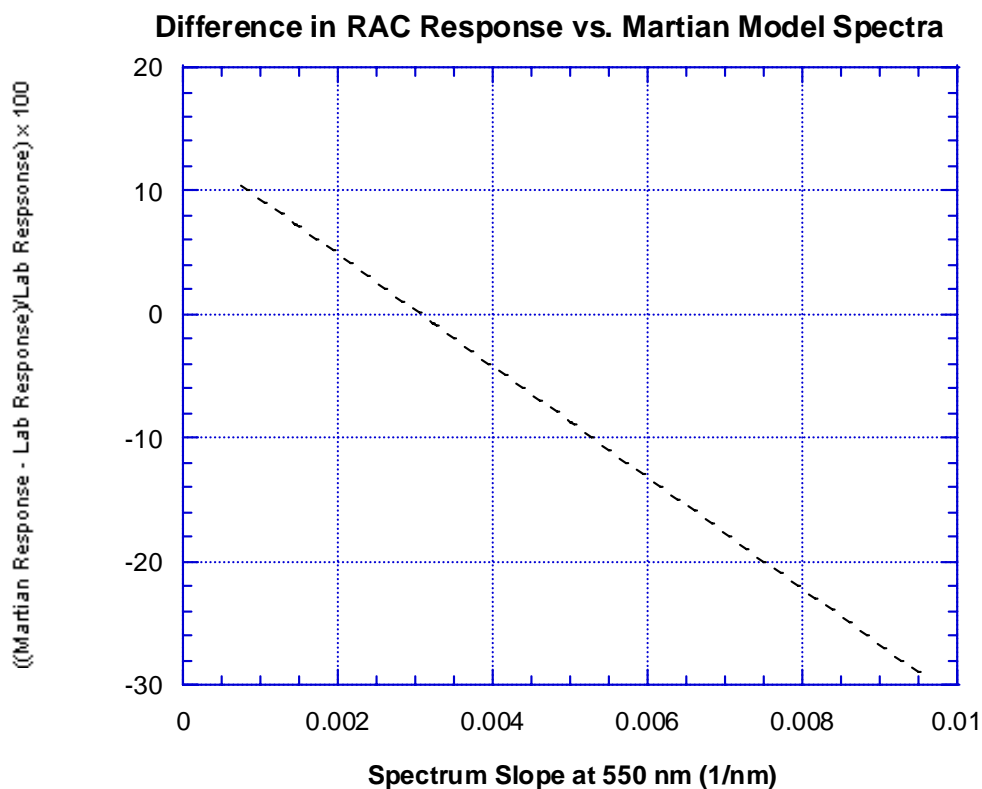
**Figure 5.3.5.3 Sensitivity of the RAC response to simulated
Martian spectra at a camera temperature of 283 K.**

slope of the line. And it is the slope of the line which indicates the RAC's sensitivity to a

spectrum's slope at 550 nm. We believe this can be a useful tool for estimating the added

uncertainty in RAC radiometric measurements caused by the RAC's large bandpass.

5.4 Responsivity with Focus Position

5.4.1 Experimental Set-Up

In the previous section of this report, Section 5.3, we discussed how the absolute

responsivity of the RAC is determined. That procedure only allows us to determine the

responsivity of the RAC at one focus position, focus motor step 306. During an actual

RAC mission, though, the RAC could be at any one of 313 different focus positions. This section of the report covers the calibration work completed to allow the determination of the RAC's responsivity at any focus position.

The experimental set-up for measuring the RAC's response with focus position is shown in Figure 5.4.1.1. The arrangement is similar to the one used in the absolute
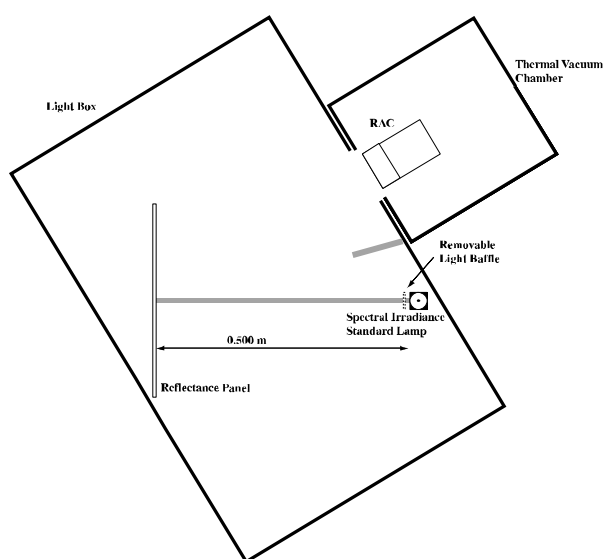
Figure 5.4.1.1. Experimental set-up for measuring RAC response versus focus step.

responsivity with temperature testing. The primary difference is that the chamber window was not in place for this testing and the RAC temperature was not controlled.

The test proceeds by taking images with the RAC cover up at a range of focus motor steps from 0 to 312 with the light baffle in front of the lamp and with it removed. Typically 5 images are taken at each step with the baffle in and out of place. This procedure is then repeated with the RAC cover down. Note that the position of the

reflectance panel is not required to be changed during the testing because it overfills the

RAC's field of view at each focus motor step.

5.4.2 Data Reduction

Turning the images acquired using the set-up shown in Fig. 5.4.1.1 into

responsivity versus focus position data requires several steps. The first step is to examine

each image using IDL and determine where the brightest points in the image are located

by utilizing IDL's *profiles* function. The intent of the experimental set-up is to center the

reflectance panel in the RAC's field of view. This is difficult to do so some variation

from the RAC's center should be expected and requires checking. Our analysis

determined that the panel was centered at pixel location (272.5, 125.5), instead of at the

nominal position (255.5, 127.5), for the cover-up condition and (265.5, 130.5) for the

cover down.

The next step in the analysis is to remove the multiple reflection effects for each

RAC lens position measured. So the DN at each pixel in a 10x10 pixel square centered

on the panel center is averaged over the number of exposures taken when the reflectance

panel is in shadow. Then these average DN values are subtracted from the same 10x10

pixel square DN image values when the reflectance panel is fully illuminated. Since both

image types were immediately shutter corrected, the subtraction of the blocked values

from the unblocked values produces DN values that only depend on $R_{i,j}$, $L_{i,j}$ and t_{exp} as

shown in Eq. (5.1.3).

The next step in the reduction is to divide the stray light corrected, mean DN

values of the 10x10 pixel blocks by the proper exposure time, t_{exp}. The exposure time in

seconds at each temperature was read out to the "H_EXPTIME" location in the RAC

image headers during the test so those values are read directly from the image header.

The mean DN/s values of the 10x10 pixel blocks are then ready to be plotted as a

function of focus motor step.

5.4.3 Results

The final reduced data from the response versus focus motor step testing is

presented in Figure 5.4.3.1. Due to the change in the RAC's working f/#, the response of

the RAC is a function of focus position. It is lowest at focus motor step 0 and highest at

step 312.

In order for the relative response to be accurately known at focus motor positions

other than those tested, we have created a model for the RAC's response which is also

shown in Fig. 5.4.3.1. The model is based on the theoretical on-axis response an imaging

system has for a given working f/#. As is well-known, an imaging system's on-axis

response is proportional to $1/f/\#^2$. The working f/# is equal to the diameter of the

system's exit pupil divided by the distance of the exit pupil to the array. So the model

used to fit the data was

$$R = \frac{a}{(b-MS)^2} \quad , \qquad\qquad (5.4.3.1)$$

where R is the RAC response in DN/s, *a* is a free variable used in the model fit, *b* is a free variable used in the model fit and MS is the focus motor step position. Variable *a* encompasses the RAC response and the image radiance. Variable *b* corresponds to the distance of the RAC's array from the exit pupil. Notice that only values measured directly during the testing need to go into the model. No other auxiliary numbers are required to perform the fit.

DN/s vs. Focus Motor Step

+ Cover Up, Mean Temp. = 3577.5286 cts
— model: 7.0054701e+09/(602.12477−Motor Step)^2

X Cover Down, Mean Temp. = 3622.3600 cts
— model: 5.9033163e+09/(601.13995−Motor Step)^2
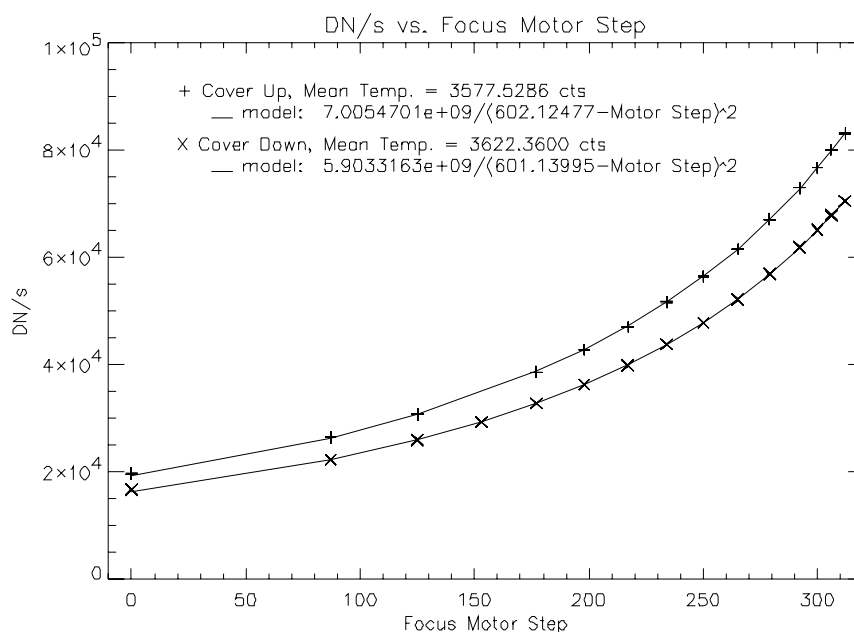
Figure 5.4.3.1 RAC response versus focus motor step.

The best fit to the cover-up data using the Eq. (5.4.3.1) model normalized to the response at focus motor step 306 is

$$R = \frac{87689.88}{(602.125 - MS)^2} \quad , \qquad\qquad (5.4.3.2)$$

and the best fit to the cover-down data is

$$R = \frac{87107.59}{(601.140 - MS)^2} \quad , \qquad\qquad (5.4.3.3)$$

where MS is in focus motor steps. The *b* parameters from the two different fits, the RAC array to exit pupil distances at focus step 0, both agree with the nominal design value to better than 0.75%

A useful result from the response testing is another check on the RAC's sapphire window transmission. As described in the previous section, the vendor reported nominal transmission value in the RAC's passband is 0.845. By taking the average DN/s at each focus motor step for the cover-down condition and dividing by the average DN/s for the cover-up condition at the same focus motor step we calculate 14 different estimates of the window's transmission. The mean value of those estimates is 0.8474. This agrees with the value found in the previous section to better than 0.1% and agrees with the nominal value to better than 0.3%. The results of this calculation are shown in Figure 5.4.3.1.
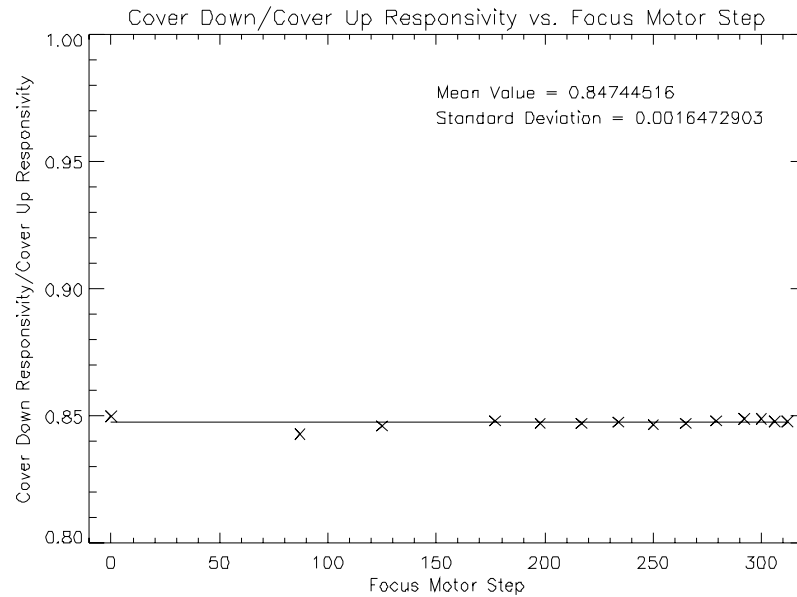
Figure 5.4.3.2 Transmission of the RAC's sapphire window cover versus focus motor step.

5.4.4 Uncertainty

As Fig. 5.4.3.1 shows, our model for the RAC's response as a function of motor step agrees very well with the measured data. To better understand how accurate the model is we have plotted the relative differences between the model and the measured response values versus focus motor step in Figure 5.4.4.1.

The plot reveals that the accuracy of the model is extremely good, better than 0.5%, for focus motor steps 87 and greater. At focus step 0 the disagreement is approximately -1.75% for the cover-up condition and -2.4% for the cover-down condition.

The cause of the larger error at motor step 0 is not completely understood. If the reflectance panel's central bright spot was not close to the RAC's optical axis then it is possible that a cosine effect could be important. But that would cause a larger error when the lens is closest to the array at step 312 – not step 0. And given that the errors are

roughly the same for both cover positions it is unlikely that the source of the error is due to a change in experimental set-up. The only thing that changes during this type of testing is the position of the lens and the cover's position. The cover cannot cause the effect seen in the data so the source of the error must come in the movement of the lens. Focus motor step 0 is the hard stop and initialization position for the RAC focus motor. It is possible that a small amount of focus motor backlash could be responsible for the larger error at motor step 0

If there is any backlash present in the focus motor, the distance between focus step 0 and focus step 87 would be less than the 3.62529 mm that we expect for the nominal condition. Using the measured response values at focus motor step 0 and the model from Eq. (5.4.3.1) we can estimate how much backlash would need to be present in order to reproduce the results. The mean response at motor step 0 for the cover-up condition is 19681.400 DN/s and 16727.134 with the cover down. Plugging these values into the model parameters shown in Fig. 5.4.3.1 indicates that there could be 5.51461 motor steps (0.22979 mm) of backlash present for the cover-up testing and 7.07045 motor steps (0.29463 mm) of backlash with the cover down (0.29463 mm).

This appears to be a reasonable explanation for the discrepancy except that it does not agree with the array to exit pupil distance values in Eqs. (5.4.3.2) and (5.4.3.3) and the nominal design exit pupil to array distance. If approximately 0.25 mm of backlash was present in the motor, then we would expect the exit pupil distance measured to be 0.25 mm greater than the nominal distance of 12.234 mm at motor step 312. But in fact the data shows it to be approximately 0.15 mm less than the nominal condition. It is

certainly possible, considering the tolerances in the lens cell, that the actual lens exit

pupil position is closer to the array than the nominal design by approximately 0.4 mm. If

this is not the case, then the parameters derived from the model are inconsistent with each

other.
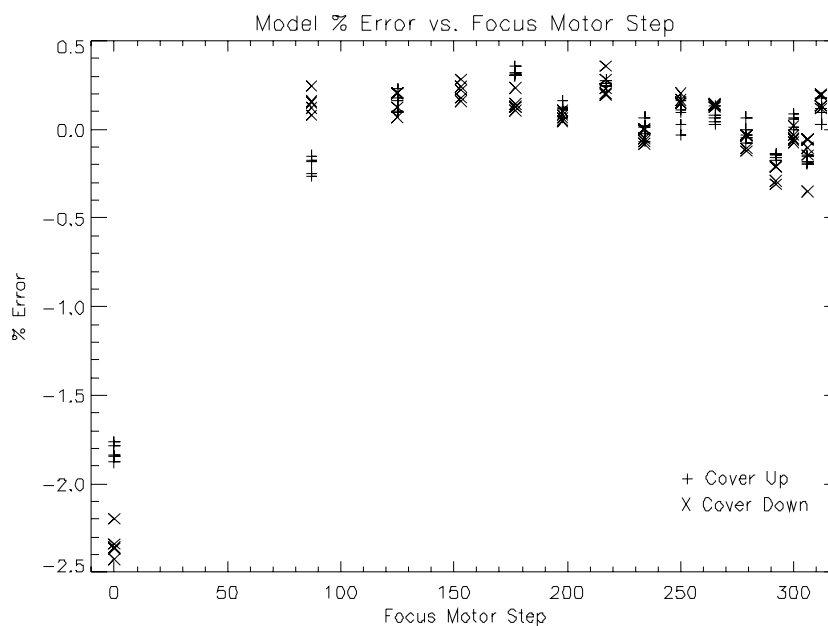
**Figure 5.4.4.1 Relative error between the RAC response versus focus
motor step model and measured values plotted versus focus motor step.**

5.5 Responsivity with Array Position

5.5.1 Overview

In the previous two sections of this report we covered the measurement and

characterization of the RAC's responsivity changes with temperature and focus motor

step. The final piece in the puzzle necessary to completely characterize the RAC's

response is to determine how it is effected by image position on the RAC's CCD. The

process of removing this effect is referred to as flat-fielding (*Reid et al.* 1999). Ideally

one would like the camera response to be uniform across the entire array but this is never

achieved in practice with systems that have any appreciable field of view. Anti-reflection

coatings have different amounts of transmission with different angles of incidence.

Individual array pixels do not all respond the same way to light. Projection effects reduce

system response at the edge of the field of view. This section of the report covers how

we measure all of these effects and how they can be removed from the data.

5.5.2 Experimental Set-Up

The experimental arrangement for determining the change in RAC response with

array position is shown in Figure 5.5.2.1. The RAC is placed facing a 20 cm diameter

exit port of a 50 cm integrating sphere manufactured by Labsphere (North Sutton, New

Hampshire). The sphere is illuminated by a baffled light source. The areas of the exit

port not covered by the RAC are blocked and a black cloth is placed over the entire test

set-up. Then typically 5 shutter corrected exposures are taken at several focus motor

steps: 0, 87, 125, 153, 177, 198, 217, 234, 250, 265, 279, 292, 300, 306 and 312. This

procedure is followed for the both the RAC cover-up and cover-down conditions. Then

without disturbing the arrangement, the sphere's lamp is turned off and 10 shutter-

corrected dark frames are taken at each exposure time used during the test.
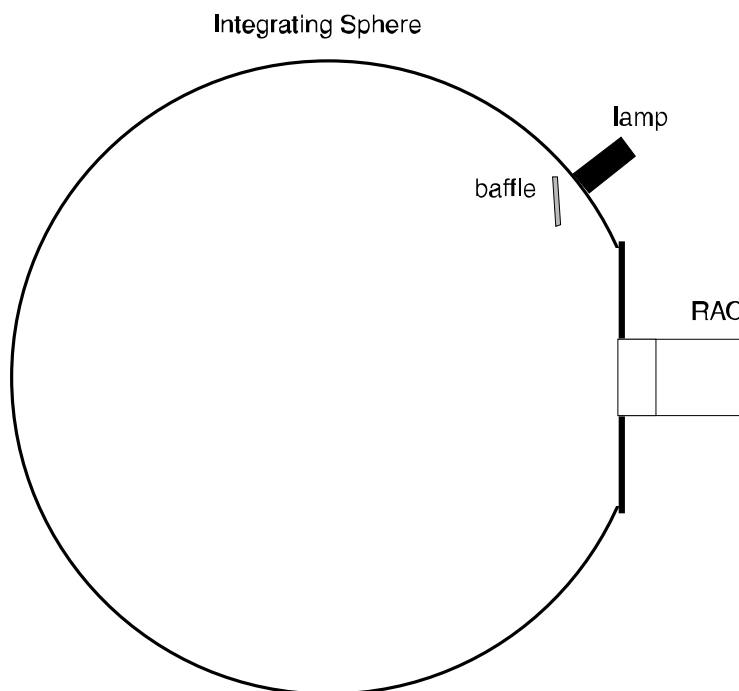
Figure 5.5.2.1 Experimental set-up for flat-field images.

5.5.3 Data Reduction

Reduction of the flat-field images is carried out using the custom IDL programs rac01_uniformity.pro and rac01_uniformity_eval.pro found in the LPL directory /home/lpl/brentb. These programs read in the images and dark frames from the test and create a mean flat field image at each focus motor step and a mean dark frame for each exposure time. Then the mean dark frames are subtracted from the images taken at the focus steps with the same exposure times. The reduced data is saved in the LPL directory /home/mars/brentb/01rac_uniform/uniformity.dat as an IDL variable. There are two sets of flat fields stored as 512x256x15 image cubes, one for each RAC cover condition.

The data acquired using the flat-field set-up in Fig. 5.5.2.1 cannot only be used for obtaining flat-fields, they can also be used to estimate the location of the optical axis relative to the CCD array. Given the high uniformity of the object and the symmetry of the RAC lens, we can estimate the location of the optical axis using two methods. The first method is to find the brightest pixel in the cover-up flat-field at focus motor step 312. Focus motor step 312 is chosen because the flat field at that motor position has the sharpest peak and is the least sensitive to multiple reflections off of the filter glass. Boxcar averages of different sizes are used to reduce the impact of any noise. Using this method we find the horizontal location of the optical axis to be located anywhere from pixel 261-264 (the nominal design location is 255.5) and the vertical location to be located at pixel 115-119 (the nominal design location is 127.5).

The second method and arguably the more accurate way of calculating the optical axis is to use a moments calculation similar to Eq. (4.3.2.2) where the pixel location, x, is now a two-dimensional vector. All 131,072 pixel values are used in the calculation. This method indicates the optical axis is centered on pixel (259.32, 126.84). Which is within a few pixels of the nominal design. Based on these two analysis methods we believe the optical axis is located at pixel (259 ± 5, 127 ± 10).

5.5.4 Uncertainty

We believe the two major sources of error in the flat fields to be the uniformity of the integrating sphere radiance and noise in the flat field images. According to Labsphere, the radiance uniformity of their spheres is 1-2% (Labsphere 2000).

Fortunately the radiance homogeneity of the actual integrating sphere we used has been studied quite extensively (*Rizk* 2001). The area of the sphere imaged by the RAC flat fields has been measured to be uniform to better than 2%.

The flat field at each motor step is the mean of five or more images taken. To estimate the image to image variation we calculate the standard deviation of the images. This reveals that the mean individual pixel response varied from 0.2-0.4% during the flat field testing (to the 2-sigma level). This effect taken together with the integrating sphere uncertainty results in a total flat field, pixel to pixel, relative uncertainty of approximately 3%.

The 3% uncertainty in the RAC flat fields is appropriate for imaging with the RAC cover in the up position. For the cover down condition the uncertainty could be significantly greater due to multiple reflections off the sapphire cover window. As previously stated, the sapphire window is known to be 85% transmissive. Almost all of the light loss is due to Fresnel reflections since the glass is not anti-reflection coated. Careful analysis of the cover-down flat-fields reveals significant structure in the images due to reflections off the RAC lens cell, particularly at the lower number focus motor steps (0-125) but visible throughout the entire range of focus. At focus motor step 0 the additional inhomogeneity is on the order of 6%. That particular flat field is shown with a linear stretch in Figure 5.5.2.2.
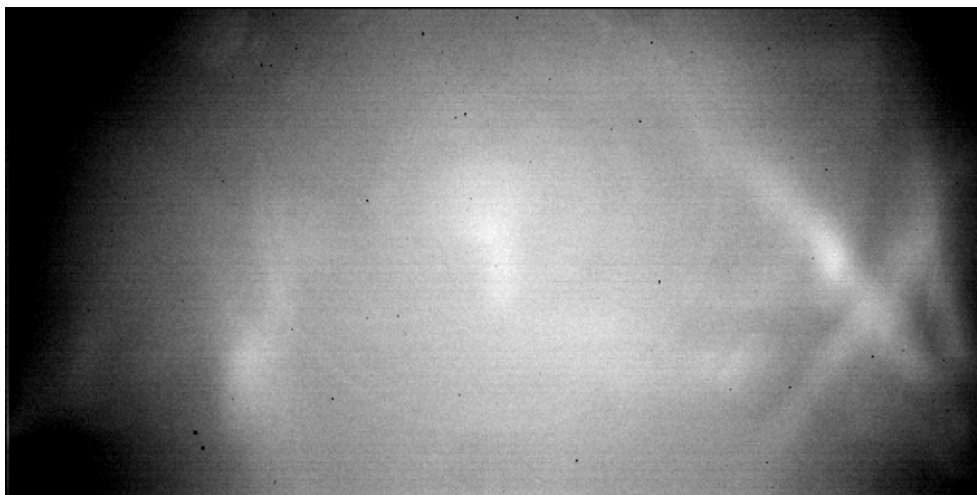
Figure 5.5.2.2 Stretched image of the focus motor step 0 flat-field.

Due to this effect, the cover-down flat-field images acquired in the laboratory may not be appropriate for use on the Martian surface. The flat fields were generated using a source that was uniformly radiant throughout a full hemisphere. If this situation is not closely matched for a particular image, different reflections will occur which will cause significant error when the laboratory flat-field is applied. We recommend obtaining Martian sky images to replace the laboratory flat fields if imaging with the cover down is required.

5.6 Full Radiometric Correction

Sections 5.3-5.5 of this report each covered a different aspect of the RAC's radiometric response. If one is only interested in correcting the relative response within

individual images, then the flat-field result from Section 5.5 is the only necessary component in the analysis. A full radiometric calibration, however, requires several steps and the results of each of the three previous sections. We outline the steps below for images taken with the RAC's cover up.

The first step in fully correcting a RAC image is to subtract from it a shutter-corrected dark frame (all images should be shutter corrected themselves) of the same exposure time. This puts the image DN values into the terms of Eq. (5.1.6). Next, the image DN values are divided by the exposure time t_{exp} to put the data in terms of DN/s.

The next step is to read out the RAC CCD temperature from the image header and determine the proper responsivity value, $R_{265.5, 188.5}$, from Eq. (5.3.4.1). This determines the camera's response at one focus position, 306, and one point on the array (265.5, 188.5). The data in DN/s is then multiplied by the inverse of $R_{265.5, 188.5}$ to put the data in radiometric units, $W/m^2/ster/\mu m$.

At this point it is appropriate to use the result from Section 5.4 found in Eq. (5.4.3.2) and correct for the focus motor step. The focus motor position of the image is read from the image header and input into the equation to determine the correction factor to divide each pixel in the image. For instance, the response of the RAC is higher at focus step 312 then at 306. This means the radiance of an object has to be lower at 312 then at 306 to produce the same DN/s.

The final step in radiometric calibration is to multiply the image by the inverse of a flat-field image that has been normalized to 1 at pixel (265, 188) and taken at the same focus motor step. If one is not available, then a linear interpolation between the two

closest focus steps should be used. At this point the RAC image is completely calibrated in W/m^2/ster/μm at 600 nm.

5.7 Total Radiometric Uncertainty

As discussed in Section 5.3, absolute radiometric measurements made with the RAC on the surface of Mars could be in error by greater than 10% for certain types of Martian spectra. And for those cases, the error due to the RAC's wide bandpass will dominate the total error. For more favorable types of spectra the total error will be due to the combination of the errors discussed in Sections 5.3-5.5. We discuss the total effect of these errors for the RAC cover-up condition below.

The absolute radiometric uncertainty as a function of temperature was found to be 5% in Section 5.3. This uncertainty is only valid at focus motor step 306 and at locations on the array close to pixel position (265.5, 188.5). For image pixel locations near (265.5, 188.5) but at different focus motor positions the result from Section 5.4 must be used to determine absolute radiometric responsivity. The total uncertainty for this scenario is 5.5% for focus steps ≥87. For focus steps less than that the total uncertainty is 7%. If absolute response needs to be known at some other place on the array, then the flat field results from Section 5.5 must be employed. The inclusion of this correction results in a total uncertainty of 9% for pixels far away from the center of the array and focus motor steps ≥87. For motor steps <87 the total uncertainty is 10%.

6.0 Focussing

6.1 Overview

As previously discussed, the RAC has 313 different focus motor positions, 0-312, which allow the camera to image objects which are very close to the camera and those located at infinity. The focus motor moves the RAC lens cell while the detector and front window remain stationary. Focus motor step 0 is the position for imaging objects close to the RAC camera, objects approximately 11 mm away. Motor step 0 is also the initialization point for the focus motor.

In order to correctly interpret RAC images, knowledge of the camera's optical performance with focus motor position is very important. Such information allows us to determine the size of objects and the distance to objects in the scene. It also allows us to pre-determine the optimum focus motor position for imaging items a known distance away, such as pieces of the spacecraft.

6.2 Experimental Set-Up

The RAC focus data are acquired by moving the RAC focus relative to a back-illuminated knife edge. This is achieved either by moving the focus motor to scan the focus point past the knife edge or by physically moving the knife edge through a fixed focus. The back-illumination produces a dark to bright step transition. An image is taken at each step. Several different focus step positions are characterized: focus step 0, 87, 100, 110, 125, 153, 177, 198, 217, 234, 250, 265, 279, 295 (approximately), 305, 309 and 310 (approximately).   The distance from the RAC BG40 filter glass to the knife edge is

measured and recorded. The BG40 filter glass and the RAC's front bulkhead are nominally at the same location. Since the CCD pixels are wider than the effective width of the lens point spread function, image contrast depends on exactly where the knife-edge image falls relative to the pixel edges. If the image of the edge falls exactly at the border of a pixel, then the contrast between the two adjacent pixels will be a maximum. Should the image fall in the middle of a pixel, the contrast will be roughly ½ of the maximum. To accommodate this effect, the knife edge is tilted at a slight angle to cause the image of the knife edge to fall at various positions relative to the edge of the pixels. The "beating" between a row of pixels and the knife edge is explored. Ideally, the tilt of the knife edge is about 3 to 10 pixels across the field of view of the camera. Somewhere along the edge one pixel will line up with the edge of the image and produce the maximum contrast possible. The magnitude of the peak contrast corresponds to the sharpness of focus for each image in a focus run.

6.3 Data Reduction

Images of the knife edge positioned at different distances away from the RAC are analyzed using custom IDL programs we wrote entitled rfoc.pro and snagfiles.pro. These programs can be found in the LPL directory /home/mars/uatest/focus. The main analysis program, rfoc.pro, reads in each image from a set and then spatially differentiates in a direction nearly perpendicular to the knife edge image (along a CCD array row or column, depending on the orientation of the knife edge) and the contrast is calculated. For each set of knife edge images at a given distance, one position of the focus motor or

knife edge produces the highest overall contrast of all the images in the set. These

contrast values are then curve-fit with a 4th order polynomial and the peak of the resulting

curve is defined as the exact focus position at the measured object distance.

6.4 Focus Model

Determining the in-focus object distance for a given motor step position is an

important piece of RAC calibration. But given the finite time available for camera

calibration, only a small fraction of the 313 focus motor step positions can be tested. And

the positions that are tested need to be further studied so that important camera optical

properties can be calculated; properties such as magnification, effective f/# and depth of

field. To address these issues we have developed a RAC camera focus model which

incorporates the RAC nominal optical design model and the knowledge gained from the

focus testing.

We use the optical design program, *Zemax*, to create the RAC focus model (Focus

Software 2000). The initial model entered into the program is the nominal RAC lens

prescription listed in Table 4.3.4.1. Then three dummy surfaces are inserted into the

design. The first dummy surface is inserted in front of the BG40 filter glass window.

This dummy surface is used to represent the position from which the object distances are

calculated in the laboratory. Care is taken to measure directly from the BG40 window

during testing but this is a difficult position to measure from in the laboratory. So the

dummy surface is included to represent the RAC front bulkhead and account for any

offset in the measurement. The second dummy surface is inserted after the BG40 filter

BG40 Filter Glass

CCD Array

Double-Gauss Lens

lens moves this direction with increasing focus motor step

Filter glass to CCD distance is constant with focus motor step

RAC Front Bulkhead
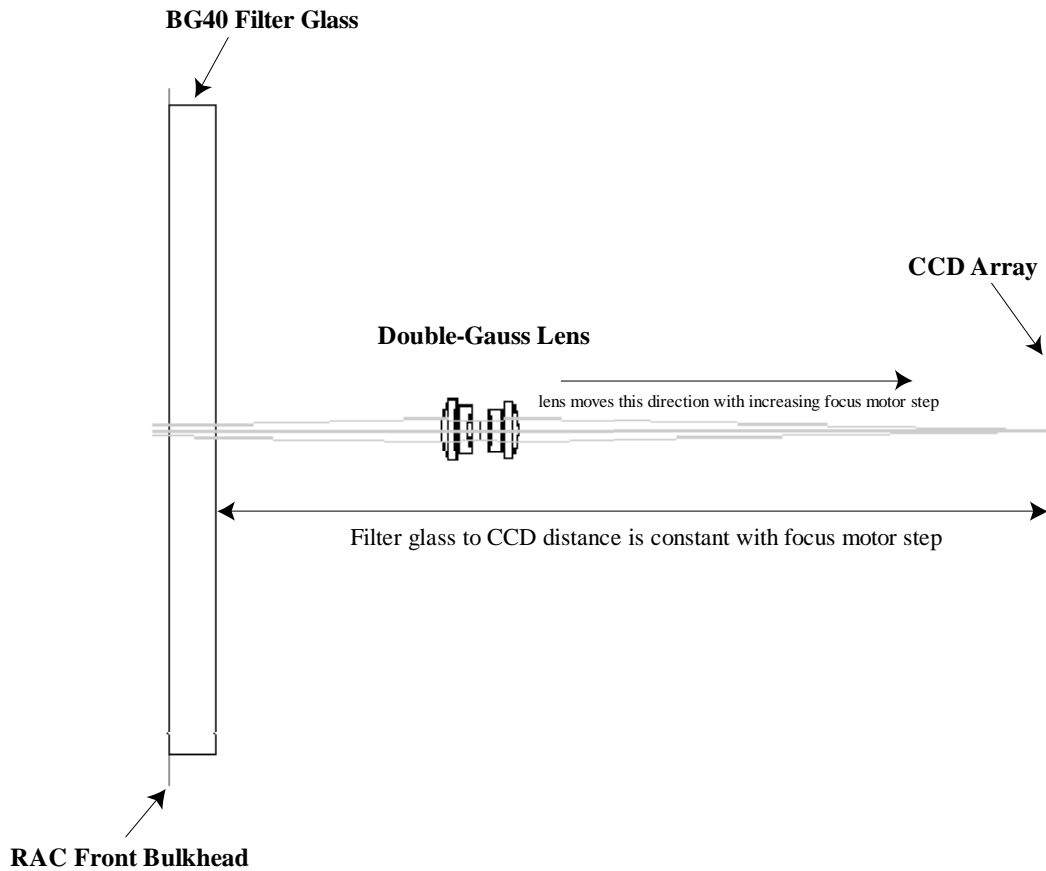
Figure 6.4.1 Zemax optical model layout

glass window to allow the introduction of additional spacing which is created by focus

motor movement. The final dummy surface is inserted in front of the image plane. Its

thickness is always the negative of the second dummy surface's thickness. A thickness

pick-up solve from the second dummy service is used to guarantee this. The third

dummy surface's presence is required to keep the distance between the BG40 filter glass

and the CCD constant.

The next step in the RAC focus model development is to incorporate the object

distance and focus step measurements. This is done by opening Zemax's configuration control window and creating 17 different lens configurations, the same procedure used in designing a zoom lens. Then the object distance and corresponding focus position measurements are entered into each configuration.

The final step in the development of the model is to identify three optimization variables and create a merit function. The first optimization variable is the thickness of the first dummy surface, since the exact position from which the object distance measurements are made is unknown. The second optimization variable is the distance from the BG40 filter glass to the second dummy surface. This distance has quite a bit of uncertainty associated with it since it cannot be measured once the camera is assembled. And the final optimization variable is the distance from the last lens surface to the third dummy surface.

Creating the merit function to optimize the three variables is straightforward. The merit function is set-up to calculate the lens MTF at a spatial frequency of 30 1/mm. The resulting MTF value is then weighted to force Zemax's optimization algorithms to find the values of the three variables that cause the MTF to be the largest. This is done across all configurations so that the final values for the three variables represent the best compromise for all of the measured data. To best determine these values we use both the standard Zemax optimization routine and the hammer optimization routine which is a genetic algorithm form of global optimization.

Evaluation of the initial results reveal that the data entered for focus motor steps 294.83 and 305 cause considerable error. The lens model cannot by reconciled with the

laboratory data at those two points and still agree with the data at the 15 other motor steps. So those two positions are left out for the final model optimization. We assume those laboratory measurements contain gross error. After standard optimization and 20.5 hours of global optimization, we find that the value which best fits the first optimization variable is 0.05061825 mm. This is the distance from the RAC front bulkhead to the filter glass. The reference point for the distance measurements is quite close to the filter window's front face. And the best fit value for the second variable (the distance from the back surface of the filter glass to the lens at motor step 0) is 10.01221 mm. The third variable's value is 23.71527 mm. This implies a total distance from the outside face of the filter glass to the CCD of 39.188514 mm which agrees well with the nominal design value of 39.0 mm.

We can also check the accuracy of the model by comparing the model's optical parameters to measurements made in other calibration testing. According to the Zemax model, the distance from the CCD to the exit pupil at focus step 0 is 25.2867 mm. The RAC response versus focus step testing (section 5.4) found this distance to be 25.090539 mm. So the model agrees with this to 0.78%. And as part of the MTF testing, image magnification was measured to determine the proper image scale. The mean magnification at focus step 0 was measured to be 1.0411765. The Zemax model found a value of 1.060276, in agreement with the measurement to 1.8%. And at focus step 279, the mean magnification was measured as 0.1178109 whereas the model finds a value of 0.1177811, an agreement of 0.025%! We believe the final RAC Zemax model is quite accurate for most applications.

Object Distance vs. Focus Motor Step
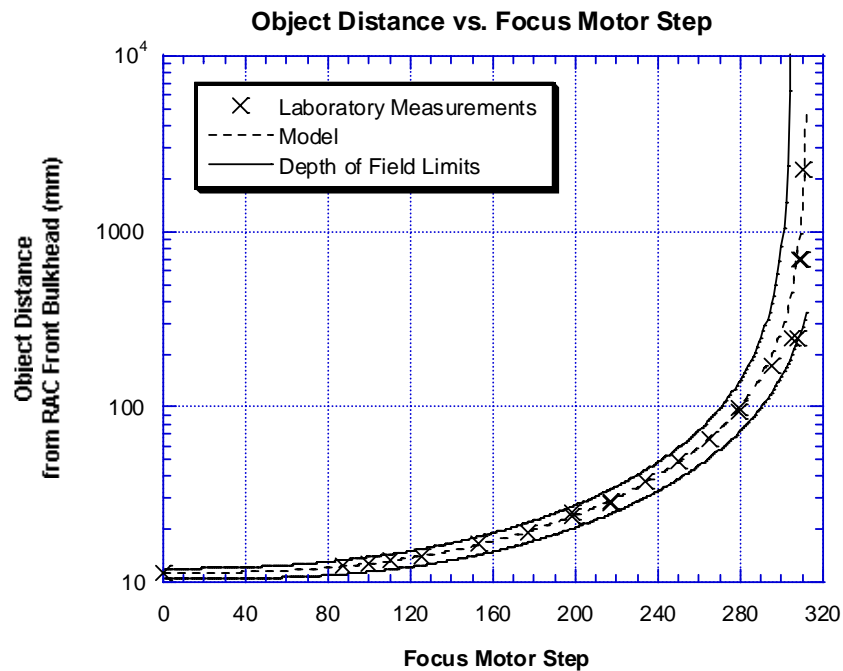
Figure 6.4.2 RAC focus results.

Using the results from the Zemax focus model optimization, we generate a

complete table of optical parameters with the Zemax focus model. Since there are 313

different focus positions, we use Zemax's macro programming language to create the

RAC focus table, Table 6.4.1.

The Zemax macro programming language is similar to the well-known

programming language BASIC (Focus Software 2000). It allows the user to command

Zemax to run through a set of instructions autonomously. For this situation, we create a

program which moves the RAC lens to the desired focus motor position, optimizes the

RAC bulkhead to object distance to maximize the MTF at 30 1/mm, then reads out the

lens position, working f/# and magnification to a text file. Then the near and far depth of

Focus Motor Step	Near Depth of Field (mm)	Object Distance (mm)	Far Depth of Field (mm)	Working f#	Magnification	Focus Motor Step	Near Depth of Field (mm)	Object Distance (mm)	Far Depth of Field (mm)	Working f#	Magnification
0	10.603	11.371	11.954	22.923	1.0527	80	10.958	12.125	13.079	19.932	0.78312
1	10.596	11.368	11.953	22.885	1.0493	81	10.978	12.152	13.113	19.894	0.77975
2	10.589	11.364	11.953	22.848	1.0459	82	10.998	12.18	13.148	19.857	0.77638
3	10.583	11.361	11.953	22.811	1.0426	83	11.019	12.208	13.184	19.819	0.77302
4	10.577	11.359	11.954	22.773	1.0392	84	11.040	12.238	13.220	19.782	0.76965
5	10.571	11.356	11.954	22.736	1.0358	85	11.062	12.267	13.257	19.744	0.76628
6	10.565	11.354	11.955	22.699	1.0325	86	11.085	12.298	13.295	19.707	0.76291
7	10.559	11.352	11.956	22.661	1.0291	87	11.108	12.329	13.333	19.669	0.75955
8	10.554	11.35	11.958	22.624	1.0257	88	11.132	12.36	13.373	19.632	0.75618
9	10.549	11.348	11.960	22.587	1.0223	89	11.156	12.392	13.413	19.595	0.75281
10	10.544	11.347	11.962	22.549	1.0190	90	11.181	12.425	13.453	19.557	0.74944
11	10.539	11.346	11.964	22.512	1.0156	91	11.206	12.459	13.495	19.520	0.74608
12	10.535	11.345	11.967	22.475	1.0122	92	11.232	12.493	13.537	19.482	0.74271
13	10.531	11.345	11.970	22.437	1.0089	93	11.259	12.528	13.580	19.445	0.73935
14	10.527	11.345	11.973	22.400	1.0055	94	11.286	12.564	13.624	19.407	0.73598
15	10.523	11.345	11.977	22.363	1.0021	95	11.313	12.600	13.669	19.370	0.73261
16	10.520	11.345	11.981	22.325	0.99875	96	11.342	12.637	13.714	19.332	0.72925
17	10.516	11.346	11.985	22.288	0.99538	97	11.371	12.675	13.761	19.295	0.72588
18	10.514	11.347	11.990	22.251	0.99201	98	11.400	12.714	13.808	19.258	0.72251
19	10.511	11.349	11.995	22.213	0.98864	99	11.431	12.753	13.856	19.220	0.71915
20	10.508	11.35	12.000	22.176	0.98527	100	11.462	12.793	13.905	19.183	0.71578
21	10.506	11.352	12.006	22.138	0.98190	101	11.493	12.834	13.955	19.145	0.71241
22	10.504	11.354	12.012	22.101	0.97853	102	11.525	12.876	14.006	19.108	0.70904
23	10.503	11.357	12.018	22.064	0.97516	103	11.558	12.918	14.057	19.070	0.70568
24	10.501	11.359	12.024	22.026	0.97179	104	11.592	12.961	14.110	19.033	0.70231
25	10.500	11.363	12.031	21.989	0.96842	105	11.626	13.005	14.164	18.995	0.69894
26	10.500	11.366	12.039	21.952	0.96504	106	11.661	13.05	14.218	18.958	0.69557
27	10.499	11.37	12.046	21.914	0.96167	107	11.697	13.096	14.274	18.920	0.69221
28	10.499	11.374	12.054	21.877	0.95830	108	11.733	13.143	14.330	18.883	0.68884
29	10.499	11.378	12.063	21.839	0.95493	109	11.770	13.19	14.388	18.845	0.68548
30	10.499	11.383	12.071	21.802	0.95156	110	11.808	13.239	14.446	18.808	0.68211
31	10.500	11.388	12.080	21.765	0.94819	111	11.847	13.288	14.506	18.770	0.67874
32	10.501	11.393	12.090	21.727	0.94482	112	11.886	13.338	14.566	18.733	0.67537
33	10.502	11.399	12.100	21.690	0.94145	113	11.926	13.389	14.628	18.695	0.67201
34	10.503	11.405	12.110	21.652	0.93808	114	11.967	13.441	14.691	18.658	0.66864
35	10.505	11.411	12.120	21.615	0.93471	115	12.009	13.494	14.755	18.620	0.66527
36	10.507	11.418	12.131	21.578	0.93134	116	12.052	13.548	14.820	18.583	0.66190
37	10.510	11.425	12.143	21.540	0.92797	117	12.095	13.603	14.886	18.545	0.65854
38	10.512	11.432	12.155	21.503	0.92460	118	12.139	13.659	14.953	18.508	0.65517
39	10.515	11.44	12.167	21.466	0.92123	119	12.184	13.715	15.021	18.470	0.65180
40	10.519	11.448	12.179	21.428	0.91786	120	12.230	13.773	15.091	18.433	0.64844
41	10.522	11.457	12.192	21.391	0.91449	121	12.277	13.832	15.162	18.395	0.64507
42	10.526	11.466	12.206	21.353	0.91112	122	12.325	13.892	15.234	18.358	0.64170
43	10.531	11.475	12.220	21.316	0.90776	123	12.373	13.953	15.307	18.320	0.63833
44	10.535	11.485	12.234	21.279	0.90439	124	12.423	14.016	15.382	18.283	0.63497
45	10.540	11.495	12.249	21.241	0.90102	125	12.473	14.079	15.458	18.245	0.63160
46	10.546	11.505	12.264	21.204	0.89765	126	12.525	14.143	15.535	18.208	0.62823
47	10.551	11.516	12.279	21.167	0.89428	127	12.577	14.209	15.613	18.170	0.62487
48	10.557	11.527	12.295	21.129	0.89091	128	12.630	14.275	15.693	18.133	0.62150
49	10.564	11.539	12.312	21.092	0.88755	129	12.684	14.343	15.775	18.095	0.61813
50	10.570	11.551	12.329	21.054	0.88418	130	12.740	14.412	15.857	18.058	0.61477
51	10.577	11.563	12.346	21.017	0.88081	131	12.796	14.483	15.941	18.020	0.61140
52	10.585	11.576	12.364	20.980	0.87744	132	12.853	14.554	16.027	17.983	0.60804
53	10.593	11.589	12.382	20.942	0.87407	133	12.912	14.627	16.114	17.945	0.60467
54	10.601	11.603	12.401	20.905	0.87071	134	12.971	14.701	16.203	17.908	0.60131
55	10.609	11.617	12.420	20.867	0.86734	135	13.032	14.776	16.293	17.870	0.59794
56	10.618	11.631	12.440	20.830	0.86397	136	13.093	14.853	16.384	17.833	0.59457
57	10.628	11.646	12.460	20.793	0.86060	137	13.156	14.931	16.478	17.795	0.59121
58	10.637	11.662	12.481	20.755	0.85723	138	13.220	15.01	16.573	17.758	0.58785
59	10.647	11.677	12.502	20.718	0.85386	139	13.285	15.091	16.669	17.720	0.58448
60	10.658	11.694	12.524	20.680	0.85049	140	13.351	15.173	16.767	17.683	0.58112
61	10.669	11.711	12.547	20.643	0.84713	141	13.418	15.257	16.867	17.645	0.57775
62	10.680	11.728	12.569	20.605	0.84376	142	13.487	15.342	16.969	17.608	0.57438
63	10.692	11.745	12.593	20.568	0.84039	143	13.557	15.429	17.072	17.570	0.57102
64	10.704	11.764	12.617	20.531	0.83702	144	13.628	15.517	17.178	17.533	0.56765
65	10.716	11.782	12.641	20.493	0.83365	145	13.700	15.606	17.285	17.495	0.56429
66	10.729	11.802	12.666	20.456	0.83028	146	13.774	15.698	17.394	17.457	0.56092
67	10.743	11.821	12.692	20.418	0.82691	147	13.849	15.79	17.505	17.420	0.55756
68	10.756	11.841	12.718	20.381	0.82354	148	13.925	15.885	17.617	17.382	0.55419
69	10.771	11.862	12.745	20.343	0.82018	149	14.003	15.981	17.732	17.345	0.55083
70	10.785	11.883	12.772	20.306	0.81681	150	14.082	16.079	17.849	17.307	0.54746
71	10.800	11.905	12.800	20.269	0.81344	151	14.162	16.178	17.968	17.270	0.54410
72	10.816	11.927	12.828	20.231	0.81007	152	14.244	16.28	18.089	17.232	0.54073
73	10.832	11.95	12.858	20.194	0.80670	153	14.327	16.383	18.212	17.195	0.53737
74	10.849	11.973	12.887	20.156	0.80333	154	14.412	16.488	18.337	17.157	0.53400
75	10.865	11.997	12.918	20.119	0.79996	155	14.499	16.595	18.465	17.120	0.53063
76	10.883	12.022	12.949	20.081	0.79659	156	14.587	16.703	18.595	17.082	0.52727
77	10.901	12.046	12.980	20.044	0.79323	157	14.676	16.814	18.727	17.045	0.52390
78	10.919	12.072	13.013	20.006	0.78986	158	14.767	16.926	18.862	17.007	0.52054
79	10.938	12.098	13.045	19.969	0.78649	159	14.860	17.041	18.999	16.969	0.51717

Table 6.4.1 RAC Focus Table

Focus Motor Step	Near Depth of Field (mm)	Object Distance (mm)	Far Depth of Field (mm)	Working f#	Magnification
160	14.954	17.158	19.138	16.932	0.51381
161	15.050	17.276	19.280	16.894	0.51044
162	15.148	17.397	19.424	16.857	0.50708
163	15.247	17.52	19.572	16.819	0.50371
164	15.349	17.645	19.722	16.782	0.50035
165	15.452	17.773	19.874	16.744	0.49698
166	15.557	17.903	20.030	16.707	0.49362
167	15.664	18.035	20.188	16.669	0.49025
168	15.773	18.169	20.349	16.631	0.48689
169	15.883	18.306	20.513	16.594	0.48352
170	15.996	18.446	20.680	16.556	0.48016
171	16.111	18.588	20.851	16.519	0.47680
172	16.228	18.732	21.024	16.481	0.47343
173	16.347	18.88	21.201	16.444	0.47007
174	16.468	19.03	21.381	16.406	0.46670
175	16.591	19.182	21.565	16.369	0.46334
176	16.717	19.338	21.752	16.331	0.45998
177	16.845	19.497	21.943	16.293	0.45661
178	16.975	19.658	22.137	16.256	0.45325
179	17.108	19.823	22.335	16.218	0.44988
180	17.243	19.990	22.537	16.181	0.44652
181	17.381	20.161	22.743	16.143	0.44316
182	17.521	20.335	22.953	16.105	0.43979
183	17.664	20.513	23.167	16.068	0.43643
184	17.810	20.693	23.386	16.030	0.43306
185	17.958	20.878	23.608	15.993	0.42970
186	18.109	21.066	23.835	15.955	0.42634
187	18.263	21.257	24.067	15.918	0.42297
188	18.420	21.452	24.304	15.880	0.41961
189	18.580	21.651	24.545	15.842	0.41624
190	18.743	21.855	24.791	15.805	0.41288
191	18.909	22.062	25.042	15.767	0.40952
192	19.078	22.273	25.299	15.730	0.40615
193	19.250	22.488	25.560	15.692	0.40279
194	19.426	22.708	25.828	15.654	0.39942
195	19.605	22.932	26.100	15.617	0.39606
196	19.788	23.160	26.379	15.579	0.39270
197	19.975	23.394	26.664	15.542	0.38933
198	20.165	23.632	26.955	15.504	0.38597
199	20.358	23.875	27.252	15.466	0.38261
200	20.556	24.123	27.555	15.429	0.37925
201	20.758	24.376	27.865	15.391	0.37588
202	20.963	24.635	28.182	15.354	0.37252
203	21.173	24.899	28.507	15.316	0.36915
204	21.387	25.169	28.838	15.278	0.36579
205	21.606	25.444	29.177	15.241	0.36243
206	21.828	25.725	29.523	15.203	0.35906
207	22.056	26.013	29.878	15.166	0.35570
208	22.288	26.307	30.241	15.128	0.35234
209	22.525	26.607	30.612	15.090	0.34898
210	22.767	26.914	30.992	15.053	0.34561
211	23.015	27.227	31.381	15.015	0.34225
212	23.267	27.548	31.779	14.978	0.33889
213	23.525	27.876	32.187	14.940	0.33552
214	23.788	28.212	32.605	14.902	0.33216
215	24.057	28.555	33.033	14.865	0.32880
216	24.332	28.906	33.472	14.827	0.32544
217	24.613	29.265	33.921	14.789	0.32207
218	24.900	29.633	34.382	14.752	0.31871
219	25.194	30.010	34.855	14.714	0.31535
220	25.494	30.395	35.340	14.677	0.31198
221	25.801	30.790	35.837	14.639	0.30862
222	26.115	31.195	36.348	14.601	0.30526
223	26.436	31.609	36.872	14.564	0.30190
224	26.764	32.034	37.410	14.526	0.29853
225	27.100	32.469	37.963	14.488	0.29517
226	27.444	32.915	38.530	14.451	0.29181
227	27.796	33.373	39.114	14.413	0.28845
228	28.156	33.843	39.714	14.375	0.28508
229	28.525	34.324	40.330	14.338	0.28172
230	28.903	34.819	40.965	14.300	0.27836
231	29.290	35.326	41.618	14.263	0.27500
232	29.687	35.847	42.290	14.225	0.27163
233	30.094	36.382	42.982	14.187	0.26827
234	30.510	36.932	43.694	14.150	0.26491
235	30.938	37.497	44.429	14.112	0.26155
236	31.376	38.077	45.186	14.074	0.25819
237	31.825	38.674	45.966	14.037	0.25482
238	32.286	39.289	46.771	13.999	0.25146
239	32.760	39.920	47.603	13.961	0.24810
240	33.245	40.571	48.461	13.924	0.24474
241	33.744	41.241	49.347	13.886	0.24137
242	34.256	41.930	50.263	13.848	0.23801
243	34.783	42.641	51.210	13.811	0.23465
244	35.324	43.374	52.190	13.773	0.23129
245	35.880	44.129	53.204	13.735	0.22793
246	36.451	44.909	54.254	13.698	0.22457
247	37.039	45.713	55.343	13.660	0.22120
248	37.645	46.544	56.470	13.622	0.21784
249	38.267	47.401	57.641	13.585	0.21448
250	38.909	48.288	58.855	13.547	0.21112
251	39.569	49.204	60.116	13.509	0.20776
252	40.249	50.152	61.427	13.472	0.20439
253	40.951	51.133	62.790	13.434	0.20103
254	41.674	52.149	64.209	13.396	0.19767
255	42.420	53.201	65.687	13.359	0.19431
256	43.190	54.292	67.227	13.321	0.19095
257	43.985	55.424	68.834	13.283	0.18759
258	44.806	56.597	70.511	13.246	0.18423
259	45.654	57.816	72.264	13.208	0.18087
260	46.531	59.084	74.098	13.170	0.17750
261	47.439	60.401	76.017	13.133	0.17414
262	48.377	61.773	78.028	13.095	0.17078
263	49.349	63.201	80.138	13.057	0.16742
264	50.356	64.688	82.355	13.019	0.16406
265	51.400	66.241	84.685	12.982	0.16070
266	52.482	67.861	87.138	12.944	0.15734
267	53.606	69.553	89.724	12.906	0.15397
268	54.772	71.323	92.453	12.869	0.15061
269	55.984	73.176	95.338	12.831	0.14725
270	57.244	75.117	98.392	12.793	0.14389
271	58.555	77.153	101.630	12.756	0.14053
272	59.920	79.291	105.070	12.718	0.13717
273	61.343	81.538	108.730	12.680	0.13381
274	62.826	83.904	112.630	12.643	0.13045
275	64.374	86.396	116.800	12.605	0.12709
276	65.992	89.026	121.260	12.567	0.12372
277	67.683	91.807	126.050	12.529	0.12036
278	69.452	94.747	131.210	12.492	0.11700
279	71.306	97.865	136.770	12.454	0.11364
280	73.250	101.18	142.780	12.416	0.11028
281	75.291	104.70	149.310	12.379	0.10692
282	77.436	108.45	156.420	12.341	0.10356
283	79.692	112.46	164.190	12.303	0.10020
284	82.070	116.74	172.720	12.265	0.096839
285	84.578	121.34	182.120	12.228	0.093479
286	87.228	126.29	192.540	12.190	0.090117
287	90.031	131.62	204.150	12.152	0.086757
288	93.001	137.38	217.160	12.115	0.083398
289	96.154	143.63	231.850	12.077	0.080036
290	99.506	150.44	248.56	12.039	0.076676
291	103.08	157.87	267.73	12.001	0.073316
292	106.89	166.01	289.94	11.964	0.069956
293	110.96	174.99	316.00	11.926	0.066595
294	115.33	184.92	346.98	11.888	0.063235
295	120.03	195.98	384.43	11.850	0.059874
296	125.09	208.34	430.60	11.813	0.056515
297	130.56	222.28	488.94	11.775	0.053155
298	136.48	238.11	564.97	11.737	0.049794
299	142.93	256.23	668.19	11.700	0.046435
300	149.96	277.19	816.33	11.662	0.043074
301	157.66	301.70	1046.9	11.624	0.039714
302	166.14	330.75	1455.0	11.586	0.036355
303	175.51	365.73	2374.2	11.549	0.032994
304	185.93	408.64	6372.4	11.511	0.029634
305	197.57	462.54	infinity	11.473	0.026274
306	210.67	532.24	infinity	11.435	0.022915
307	225.51	625.93	infinity	11.398	0.019555
308	242.47	758.53	infinity	11.360	0.016194
309	262.04	960.55	infinity	11.322	0.012835
310	284.87	1305.9	infinity	11.284	0.009475
311	311.84	2030.5	infinity	11.247	0.006116
312	344.18	4521.3	infinity	11.209	0.002756

Table 6.4.1 RAC focus table cont.)

field distances are found and read-out to the same text file. This process is repeated for all 313 focus motor positions until all table entries are completed.

We should note that the near and far depth of field distances are determined by varying the Zemax model object distance until the geometric point spread function RMS radius grows to 11.5 μm, half the size of the CCD array's pixel pitch. Choosing such a focus criterion does result in a loss of image contrast for any object distance beyond nominal, as would any criterion. The Zemax model predicts, for focus step 0, a near depth of field drop in image contrast of 39% at 25 1/mm and a far depth of field drop of 17%. At focus step 279 the drop in contrast at 25 1/mm is predicted to be 51% at the near depth of field and 38% at the far depth of field. And at focus step 312 image contrast is expected to drop 53% at the near depth of field and 0.54% at the far depth of field. This amount of image contrast reduction is similar to the drop in contrast we measured in a single image in Section 4.3.3 of this report. This choice of focus criterion also causes the model to predict that the hyperfocal position occurs at focus motor step 305, very close to our initial nominal design estimate of 306.

A review of Table 6.4.1 shows that only 13 different focus motor steps are required to image an entire scene with acceptable image quality from an object distance of 10.603 mm to infinity. For the RAC user's convenience, recommended focus motor positions are highlighted in Table 6.4.1. In addition, we have illustrated for the standard focus motor positions, based on the focus model results, where the various RAC object planes are located relative to the 2001 robot arm and scoop in Figure 6.4.3. One final item of interest, the distances recorded in Table 6.4.1 are the object distances from the
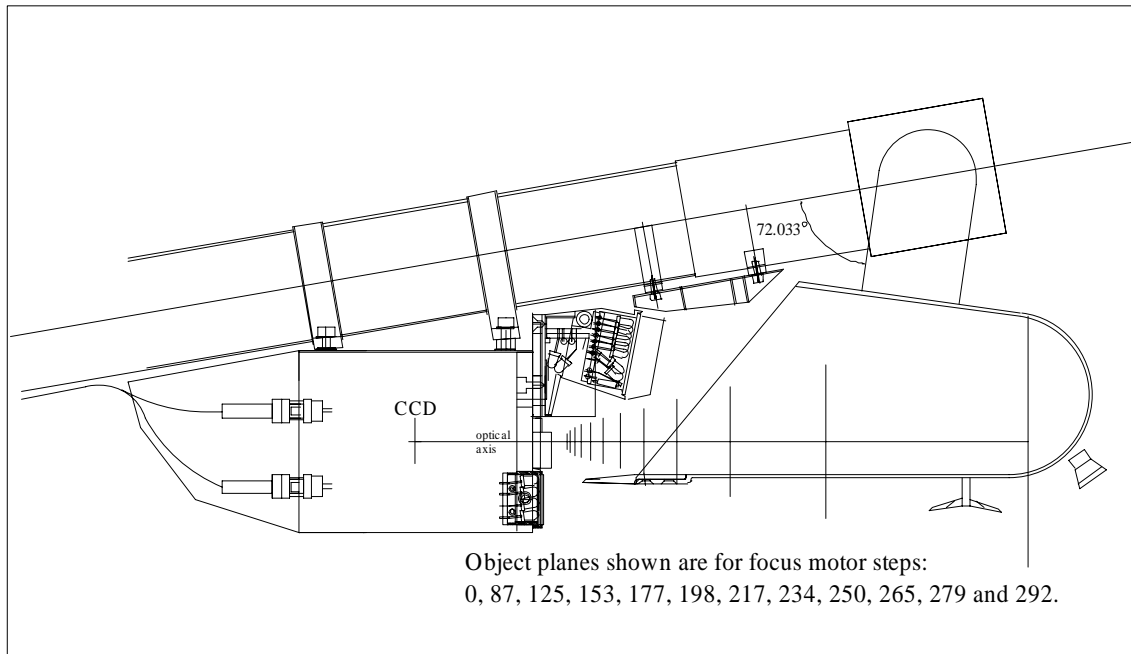
Figure 6.4.3 The location of object planes for standard focus motor steps relative to the 2001 robot arm and scoop.

RAC front bulkhead. The object distance to the RAC filter glass is an additional

0.05061825 mm.

For investigators who prefer not to use the focus table, we also have derived an

equation which accurately reproduces the Zemax model generated object distances to

better than 0.05% for most focus steps and never disagrees more than 0.22% for any

focus position. The equation is derived from the well-known Gaussian lens equation

$$\frac{1}{So} + \frac{1}{Si} = \frac{1}{f} \quad , \qquad (6.4.1)$$

where *f* is the lens effective focal length, So is the distance from the object to the lens

front principal plane and Si is the distance from the rear principal plane to the image

plane. For the RAC lens modelling we use the following relationships

$$\text{So} = \text{Do} + \text{Xo} + \text{MS} \cdot \Delta \quad , \qquad (6.4.2)$$

and

$$\text{Si} = \text{Xi} - \text{MS} \cdot \Delta \quad , \qquad (6.4.3)$$

where: Do is the object distance from the RAC front bulkhead, Xo is the distance from

the RAC front bulkhead to the front principal plane at focus step 0, MS is the motor step,

Δ is the distance moved per motor step and Xi is the distance from the rear principal

plane to the CCD at focus step 0. Inserting Eqs. (6.4.2) and (6.4.3) into Eq. (6.4.1) and

solving for Do produces

$$\text{Do} = \frac{f(\text{Xi} - \text{MS} \cdot \Delta)}{\text{Xi} - \text{MS} \cdot \Delta - f} - \text{Xo} - \text{MS} \cdot \Delta \qquad (6.4.4).$$

We plug in the nominal values for each variable as a starting point and then allow the

variables to change to best fit the Zemax model object distances. We find the best fit

when: $f = 12.462$ mm, $\Delta = 0.041733$ mm, Xi $= 25.517$ mm and Xo $= 12.985$ mm.

6.5 Uncertainty

The two primary sources of error in the RAC focus results come from the measurement of the object distance and the insufficient knowledge concerning the final state of the RAC lens. Based on the agreement between the RAC Zemax model and the various laboratory measurements, we estimate that object distances from the front bulkhead of the RAC camera can be known to better than 1.5% for most focus step positions. An error of 1.5% is a reasonable estimate for the magnification uncertainty as well.

7.0 Lamps

7.1 Overview

The LED lamps on the RAC serve two purposes: to illuminate objects close to the camera when the ambient illuminance is low and to enable the acquisition of color images. As described earlier, the RAC has an upper and lower assembly of LED lamps. The lower assembly consists of 8 red, 8 green and 16 blue LED's. The upper assembly has 16 red, 16 green and 32 blue LED's aimed to illuminate the RA scoop and 4 red, 4 green and 8 blue LED's pointed down to illuminate the RA scoop blade and other close-up objects. In order to completely understand the images acquired with the RAC lamps on we have characterized the uniformity of their radiation pattern and their change in output with temperature.

7.2 Lamp Flat-Fields and Response

7.2.1 Experimental Set-Up

Unlike the flat-field work of Section 5.5, the RAC lamp flat-field target needs to be in-focus when the measurement is made. But since the RAC functions as a medium power microscope when imaging nearby objects, a special technique for obtaining RAC lamp flat-fields is required. This is necessary because commercially available reflectance panels are not highly uniform when imaged under magnification. Texture can be seen.

The procedure to get around this problem is to take images of a reflectance panel

Reflectance
Panel

RAC w/
lamps on

Panel is scanned left and
right and up and down.

Distance set so panel is in focus
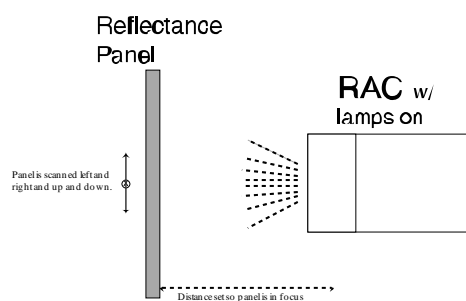
while the RAC lamps are on with the reflectance panel in different locations, up and down, left and right, with respect to the camera. Then when these images are added

Figure 7.2.1.1 RAC Lamp Flat-Field Set-Up

together and averaged the structure in the image is reduced, yielding a higher quality lamp flat-field.

So the laboratory procedure is to set-up a reflectance panel a known distance from the RAC so that it is in focus. Then take 3 shutter corrected images. Next, move the

panel to the left and take another 3 shutter corrected images. Move the panel up and take

3 more shutter corrected images. And finally, move the panel to the right and take

another 3 shutter corrected images. This process is completed individually for the red,

green and blue lamps and at various focus motor steps. In addition, testing is carried-out

when both the upper and lower assembly lamps are on and when just the upper lamps are

on. Since it is impossible to control the upper and lower lamp assemblies separately,

opaque tape is placed over the lower assembly lamps during the upper lamps only test.

This type of test is required because it is possible during operations on the Martian

surface that the RA scoop might keep the lower lamp light from illuminating an object.

For our testing we use focus motor steps: 0, 87, 125, 153, 177, 198, 217, 234, 250, 265,

279, 292 and 300 for testing with both lamp assemblies on. And we use focus motor

steps: 0, 87, 125, 153, 177, 198, 217, 234, 250, 265, 279 and 292 for testing using only

the upper lamp assembly light. Figure 7.2.1.1 shows a schematic for the test set-up.

7.2.2 Data Reduction

The RAC lamp flat field data reduction is conducted using the custom IDL codes

rac01_lamp_flat.pro, rac01_lamp_flat_eval2.pro and rac01_lamp_flat_eval3.pro. These

codes read in the image data for each focus motor step, each lamp color and each lamp

assembly. Then the data for each configuration are averaged and a shutter corrected dark

frame is subtracted to produce the final lamp flat fields. The images are stored in the

LPL directory /home/mars/brentb/01rac_lamp_flat as IDL variables. In addition, the

image exposure times, sample size and standard deviations are calculated and saved as

well.

Figure 7.2.2.1 shows a plot of the lamp flat fields' DN/s versus motor step for 3 different pixel locations when both lamp assemblies illuminate the target. Figure 7.2.2.2 shows the same plot for when only the upper lamp assembly illuminates the reflectance panel. The shape of each individual curve as a function of the focus motor step is effected by: the reduction in working $f/\#$ with increasing motor step, the fall-off in lamp illumination with increasing focus motor step, the RAC field of view, the RAC lamps area of illumination and off-axis cosine effects. Figure 7.2.2.3 presents the same data as Figs. 7.2.2.1 and 7.2.2.2 except object distance is on the horizontal axis in place of focus motor step.

Generally the response curves show that the RAC's response to a white object is highest using the blue LED lamps, almost 2 times higher than when using the green lamps and 2.5 to 3 times higher than when using the red lamps. The plots also demonstrate that illumination uniformity is best for lower focus motor steps. We must note here that lamp flat fields do not exist for the two upper corners of the RAC's field of view for motor steps 154-249. This is due to the use of a circular reflectance panel during the lamp flat field testing at motor steps 0-234. At focus steps 177, 198, 217 and 234 the field of view of the RAC was larger than the target could accommodate and so there is not any flat field information for the corner pixels. The lamp flat field that is missing the most information is the one obtained for focus motor step 217 which corresponds to an object distance of 29.265 mm. That flat field for when both the upper and lower red lamp assemblies are on is shown in Figure 7.2.2.4 If possible, we
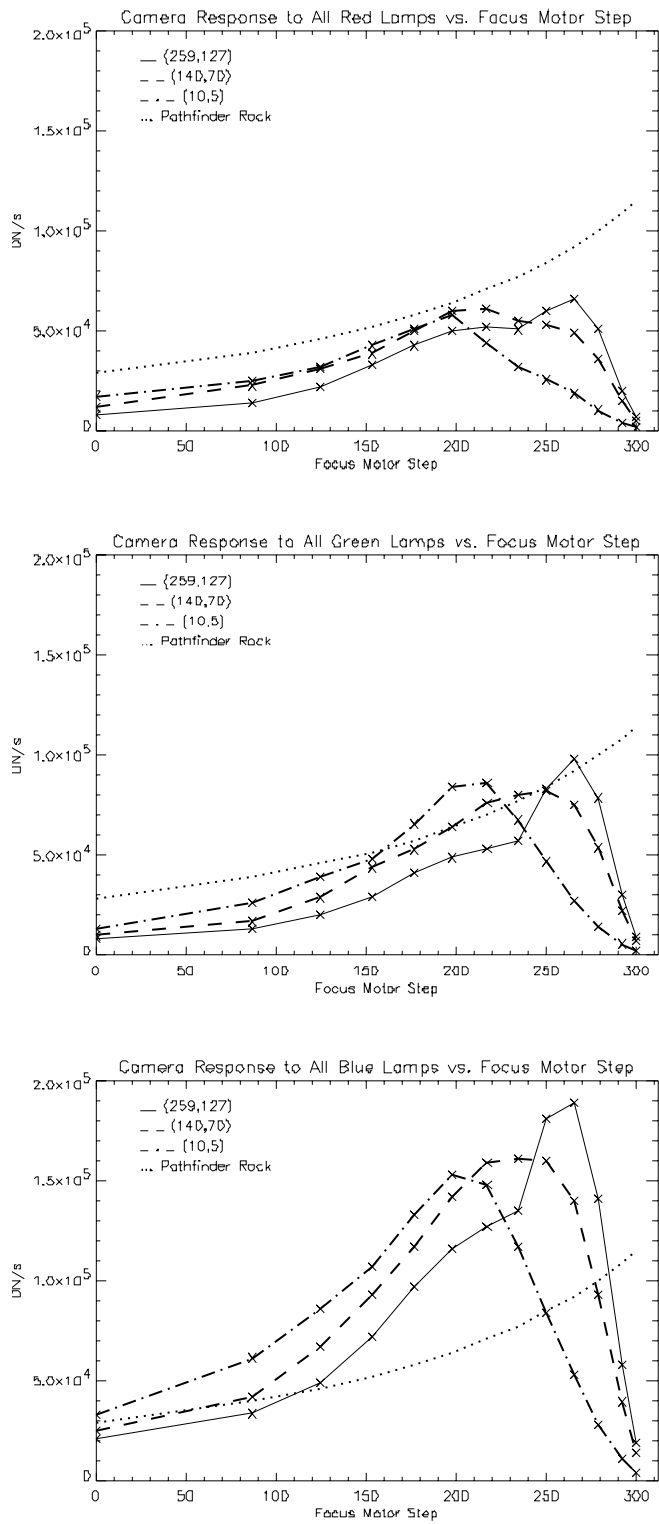
Figure 7.2.2.1 The RAC response to a white object (0.99 reflective) at three positions on the array with illumination from the upper and lower lamp assemblies, compared with the on-axis response to a Mars rock under ambient illumination.
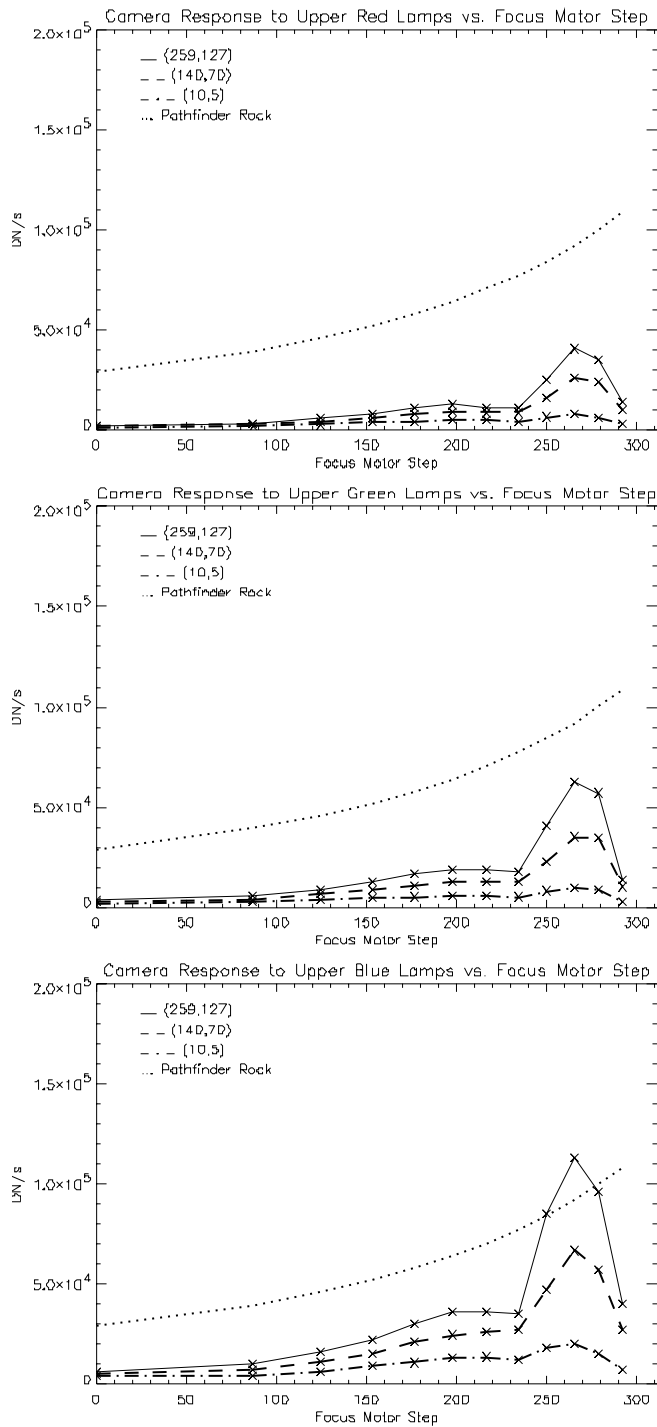
Figure 7.2.2.2 The RAC response to a white object (0.99 reflective) at three positions on the array with illumination from the upper lamp assembly alone, compared with the on-axis response to a Mars rock under ambient illumination.
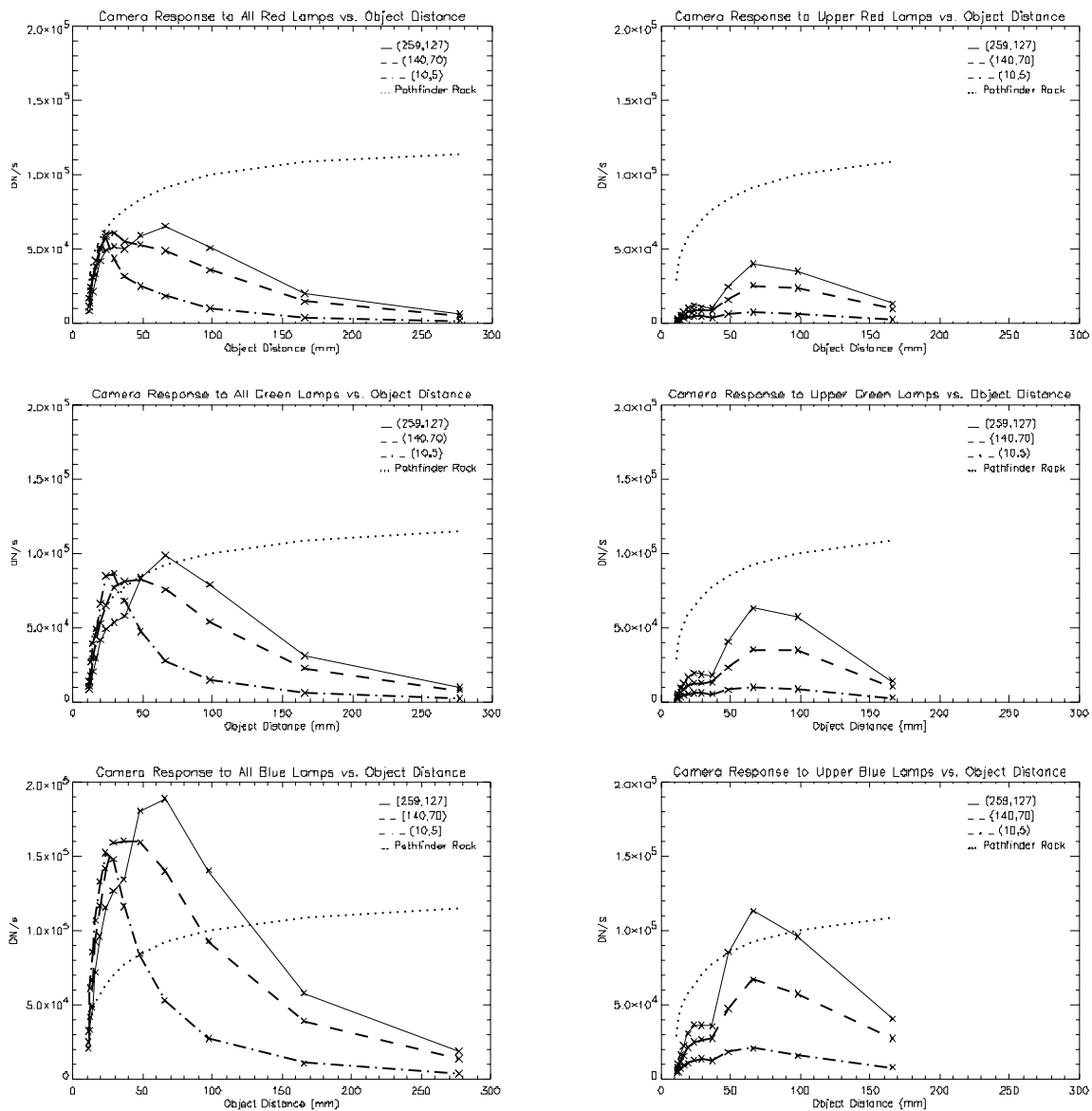
Figure 7.2.2.3 A second presentation of the data shown in Figures 7.2.2.1 and 7.2.2.2 showing the camera to object distance on the horizontal axis in place of focus motor step.

recommend the return of the RAC to the Lunar and Planetary Laboratory before flight so that lamp flat fields can be obtained for motor steps 177, 198, 217 and 234 using a small, rectangular target.

The peak response of the RAC, when only its own lamps provide illumination, occurs for pixels near the center of the array in the focus motor step range of 250-265 which, according to focus table 6.4.1, corresponds to object distances of 48.288-66.241 mm. Beyond that range the increasingly large illumination distance causes the RAC's response to its lamps to fall-off quickly.

Some more interesting information can be gleaned from the lamp flat field data which pertains directly to the operation of the camera on the Martian surface. Figures 7.2.2.1-7.2.2.3 include the predicted response of the RAC to a typical Martian rock under Mars ambient light. This was calculated by using the published typical Martian rock
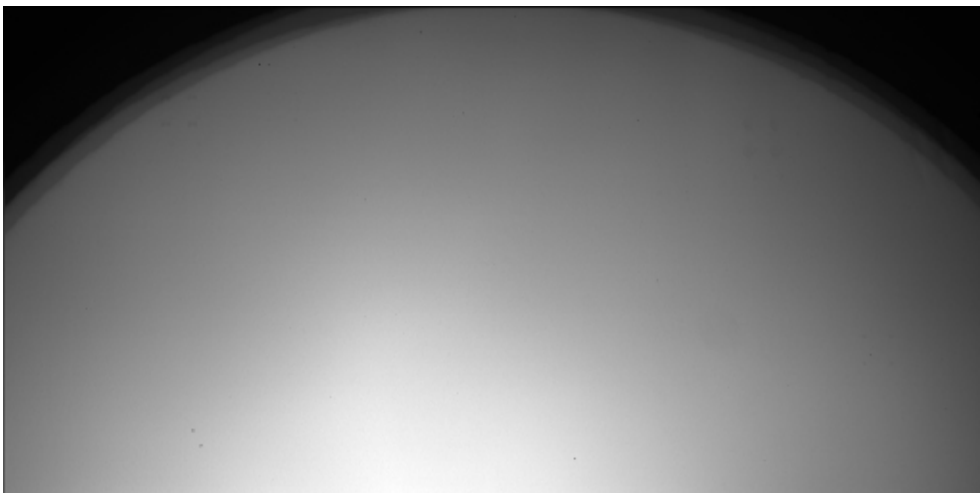
Figure 7.2.2.4 Upper and lower red lamp flat field at focus motor step 217 (object distance of 29.265 mm) which demonstrates the worst case of missing flat field data.

spectral radiance that was measured during the Mars Pathfinder mission (Maki *et al*.

1999). The value was 16 W/m^2/ster/μm at 600 nm. Then we used the results from

Section 5 of this report for the absolute responsivity of the RAC (Eq. 5.3.4.1) and the

response with focus motor step (Eq. 5.4.3.2) to calculate the curve at a CCD temperature

of 0° C. The resulting Mars rock, RAC response curve is: the response the RAC would

have on axis if the rock was illuminated by direct sunlight and able to be illuminated by

roughly the entire hemisphere of the Martian daylight sky if the RAC was at a

temperature of 0° C. And so the Mars rock response curve can be thought of as an

absolute maximum response.

To get an idea of how effective the RAC lamps will be on the Martian surface, we

can use the Mars rock response curve and the lamp flat field results to predict how the

RAC will respond to the Martian landscape. We will look at the situation for when we

use the RAC to image rocks on the Martian surface where we want to dig a trench. To be

in focus, the focus motor step would have to be somewhere between 265 and 300. We

will choose 265 for this calculation. And for this scenario the Martian rocks would be in

almost full view of the sun and sky. According to the information shown in Figures

7.2.2.1-7.2.2.3, the RAC response to the rock would be 9.1936 x 10^4 DN/s and the

response to a white target with all the red lamps on would be 6.5396 x 10^4 DN/s. Two

further calculations are required here. In Section 5.0 of this report we described how the

response of the RAC to a Martian spectra could be 11.3% lower than the calibration

showed. If we include this, then the rock response would be 8.15 x 10^4 DN/s. The

laboratory response was for a 0.990 reflective object in the red. But based on our Mars

Pathfinder results for a typical Martian rock we would expect it to be approximately 0.33 reflective in the red. So, the RAC response to a rock illuminated by only the upper and lower red lamp assemblies would be 2.18×10^4 DN/s.

As previously discussed, the maximum DN possible for a RAC image is 4095. So the maximum RAC exposure time for an image of the Martian rock with all the red lamps on would be 39.6 ms. Such an image could contain no more than 864 DN of information on the spectral response of the rock. This is better resolution than a standard 8-bit image offers but not as good as a 10-bit. This is based on the response of the RAC to the red lamps at room temperature. We did not take into account the change in RAC response with temperature and the LED output change in temperature for the lamp data since it is unavailable at this time.

If we follow the same calculation through as the previous one, at a focus motor step of 300, we find there would only be 88 DN of information able to be obtained concerning the red response of the rock. Therefore we conclude that obtaining 12-bit color images of the Martian surface will be impossible during the day. In addition, beyond motor step 265 the RAC response to the lamps falls off dramatically as the response to the ambient light illuminated Martian rock goes up, making good color images very difficult to obtain of objects further than 66.241 mm away. So for the best color resolution of the surface we recommend taking exposures during nighttime.

Of course it is not hard to imagine situations where rock or soil of interest might be in a substantial shadow. This would be particularly true of objects deep in a trench dug by the robot arm. In that situation we would expect to be able to resolve color

information with 10-bit resolution. In particular, we should be able to do quite well

imaging objects in the RAC scoop which are shadowed by the robot arm, the side baffles

and the RAC itself. We can use Figure 7.2.2.2 to develop a rough worst case scenario for

how much color information could be obtained using the same calculation method as

described above. Doing such a calculation at focus motor step 0 reveals that we would be

able to retrieve 92 DN of red color information using only the upper lamp assembly even

if the object was in complete view of the sun and sky, which we know it would not be.

And if we make a conservative estimate for the blocking effect of the RAC, the robot arm

structures and the scoop, say that they would block 65% of the light reported from the

Pathfinder results, then we would be able to obtain almost 8-bits of information (254

DN). These are rough, first order calculations. For a more accurate analysis we would

need to account for the change in RAC response and LED output with temperature and

separate the direct sunlight and skylight effects on the Mars rock and integrate over the

amount of sky visible to the rock. But that would go beyond the scope of this work. And

so, based on our approximate calculations, we recommend scoop imaging with RAC,

robot arm and scoop geometries that shade the robot arm scoop from as much of the sun

and sky as possible. We caution, however, that even when imaging in these scenarios,

that it is still possible that stray light could make it into the scene and make it difficult to

interpret the images due to uncontrolled changes in the ambient light.

7.2.3 Error and Uncertainty

The primary source of error in the RAC lamp flat fields at low to intermediate

focus motor steps is the structure visible in the reflectance panel under magnification, as

described in Section 7.2.1. To estimate how much error is associated with the lamp flat

fields we calculate the standard deviation of the mean for each pixel in the flat fields

using all the image samples acquired during calibration, there are typically 12 samples.

To understand the level of uncertainty for each flat field we calculate the median percent

error in a pixel value based on a $2\sigma_m$ (2 standard deviations of the mean) level. The

results for when both lamp assemblies provide illumination are listed in Table 7.2.3.1 and

Table 7.2.3.2 contains the results for when only the upper lamp assembly provides

illumination.

The most troubling result from the uncertainty calculations is the 3.42%

uncertainty for a single pixel when illuminating with all the red lamp assemblies at focus

motor step 198. This large amount of error is caused by an unknown source and is not

consistent with the trends seen in the data nor is it consistent with the camera's behavior

when using the green and blue lamps. Individual inspection of the images for that data

point does not reveal any glaring errors that would make the source of the large error

obvious. The camera was at the proper focus motor step for all the images at that point

Focus Motor Step	Red $2\sigma_m$ % Error	Green $2\sigma_m$ % Error	Blue $2\sigma_m$ % Error
0	1.01	1.15	0.957
87	0.877	0.901	0.746
125	0.860	0.710	0.605
153	0.635	0.605	0.537
177	0.739	0.540	0.498
198	3.42	0.534	0.515
217	0.869	0.671	0.540
234	0.612	0.440	0.419
250	0.714	0.570	0.550
265	0.694	0.498	0.493
279	0.714	0.406	0.417
292	0.494	0.325	0.330
300	0.563	0.304	0.315

**Table 7.2.3.1 Typical uncertainty at one pixel in lamp flat
fields when all lamp assemblies provide illumination.**

Focus Motor Step	Red $2\sigma_m$ % Error	Green $2\sigma_m$ % Error	Blue $2\sigma_m$ % Error
0	2.51	2.67	2.71
87	2.06	2.17	2.21
125	1.53	1.61	1.64
153	1.18	1.22	1.25
177	0.974	0.962	0.976
198	0.873	0.816	0.830
217	0.775	0.650	0.654
234	0.863	0.713	0.696
250	0.990	0.951	0.914
265	0.766	0.673	0.673
279	0.587	0.424	0.432
292	0.571	0.525	0.329

**Table 7.2.3.2 Typical uncertainty at one pixel in lamp flat fields
when only the upper lamp assembly provides illumination.**

and all the images were taken with the same exposure time. The order of the data

acquisition at focus motor step 198 is: take 3 images with red lamps on, take 3 images

with green lamps on, take 3 images with blue lamps on, then move the target and repeat

the procedure until 12 images are obtained for each color. If something in the

experimental set-up had changed during the course of this test, then the data taken after

the red lamp data for the other 2 lamp colors should also exhibit larger uncertainties. Our

best thought at the moment for the larger uncertainty is that one set of 3 images was

obtained using illumination from the blue lamps instead of the red lamps but this cannot

be verified from the information read out to the image headers during the calibration

testing.

Another aspect one should notice of the lamp flat field uncertainty results is that

the error goes down with increasing focus motor step. This is due, as previously

mentioned, to the disappearance of the panel structure as it is moves further away from

the RAC. At larger focus motor steps the single pixel uncertainty of the lamp flat fields

approaches the 0.4% level, comparable to the standard flat field single pixel uncertainty

of Section 5.5.

The data also show for lower focus motor steps that the uncertainty in the upper lamp assembly flat fields is substantially larger than the uncertainty when both lamp assemblies provide illumination. This is most likely due to the longer exposure times used when acquiring the upper lamp assembly data. The exposure times were approximately 5 times longer with only the upper lamps on at low to moderate focus motor steps.

One final issue concerning this data is that if possible, it would be advantageous to return the RAC to LPL to re-calibrate the RAC lamp flat fields to try and achieve higher accuracy at the lower focus motor steps. We believe this could be achieved with a slight modification to the original test set-up in which the reflectance panel is continuously moved during the duration of an exposure. Reflectance panel movement could be achieved through rotation or vibration of the panel. In any case, such a re-test would also allow the acquisition of a higher quality, all red lamp assemblies on, flat field at focus motor step 198 which has more uncertainty associated with it than expected.

7.3 Lamp Responsivity with Temperature

7.3.1 Experimental Procedure

The RAC was tested in the thermal vacuum chamber for lamp responsivity changes with temperature by imaging a Spectralon target, which was outside the chamber. The set-up was similar to the one described in Section 5.3.1. The RAC LED lamps illuminated the Spectralon. Five shutter corrected images were taken at each of the

test temperatures with the shutter window up and down. After taking a set of images at room temperature, the cover of the thermal vacuum chamber was removed and another set of images taken again. These second images were used to remove the effect of the window on the imaging. The effects were the reduction in effective illumination distance and the reflection loss from the window. The chamber window is 25 mm thick and reduces the effective illumination distance by 8.5 mm. The target was at a distance of 109 mm from the face of the camera and the lens was set at 275 steps focus distance, which was best focus for the target. When the cover was on, the effective distance was 101 mm. The illumination levels were fairly high, the typical exposure was 15 to 70 milliseconds.

7.3.2 Data Reduction

The images were dark subtracted and medium combined to create a set of calibrated images. A typical image is shown in Figure 7.3.2.1. The center portion Spectralon was used for analysis, the portion free of reflected images of the LEDs in the upper and lower lamp assembly. This area was about 200 x 86 pixels in the middle of the frame.
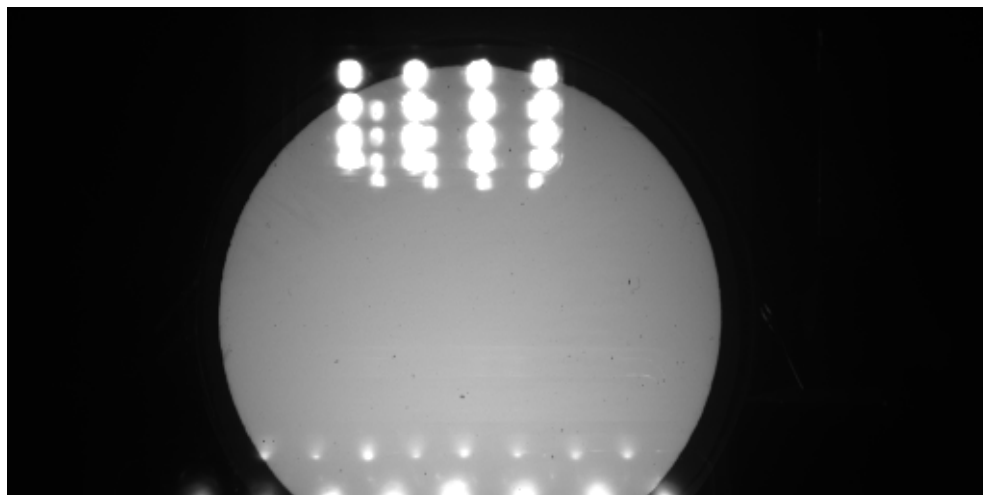
Figure 7.3.2.1 Sample image from the RAC inside the thermal vacuum chamber looking at the Spectralon target.

The analysis was done using the average of the central 10 x 10 pixels (pixels 251:260,123:132). The data was divided by the exposure to convert the data into Data Numbers (DN) / sec. The cover down averages were divided into the cover up averages for comparison. The loss was relatively constant at 14-15% independent of temperature. This loss is due to the reflection loss of the uncoated sapphire cover window. Since the loss was constant, the cover down data was multiplied by the average ratio and curve fit along with the cover up data. The data was further calibrated by dividing by the reflectivity of the Spectralon (99%) and multiplying by the ratio of the vacuum chamber cover off / on ratio. This ratio was .861 (Red), .873 (Green), to .91 (Blue). The resulting data was fit with a third order polynomial and the results are shown in Figures 7.3.2.2a-c. In these plots the cover down data is multiplied by the average cover up/down ratio and

plotted along with the cover up data. Table 7.3.2.1 lists the resulting coefficients and the

ratio of cover up to cover down to convert the curves to cover down data.

Color	C [0]	C [1]	C [2]	C [3]	Sigma from fit	Cover down / cover up ratio
Blue	135051	-514.128	1.21592	.0357287	1094	.8695
Green	76477.5	-220.509	.455685	.0210156	615	.8554
Red	54104.9	-502.654	2.96976	.0324108	1194	.8677

Table 7.3.2.1 RAC lamp responsivity vs. temperature results, equation is DN/sec=C [0] + C [1]*T + C [2]*T^2 + C [3]*T^3, where T is temperature in degrees C. This is for cover up imaging. Multiply result by cover down ratio to get DN/sec for cover down images.
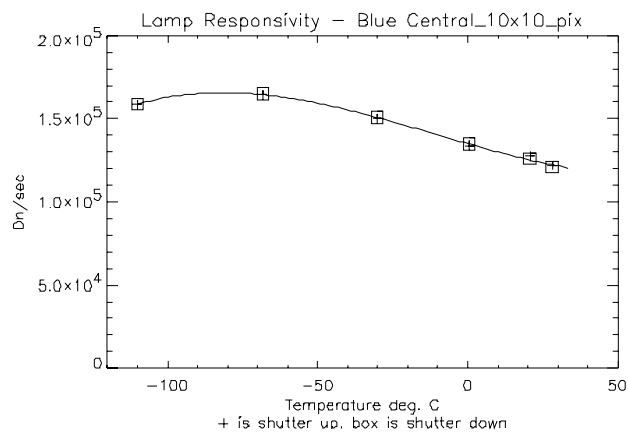
Figure 7.3.2.2a Change in Responsivity of the Blue LEDs with temperature.
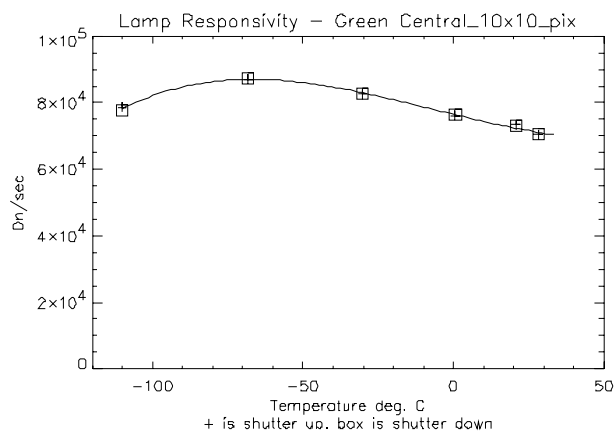
Figure 7.3.2.2b Change in Responsivity of Green LEDs with temperature.
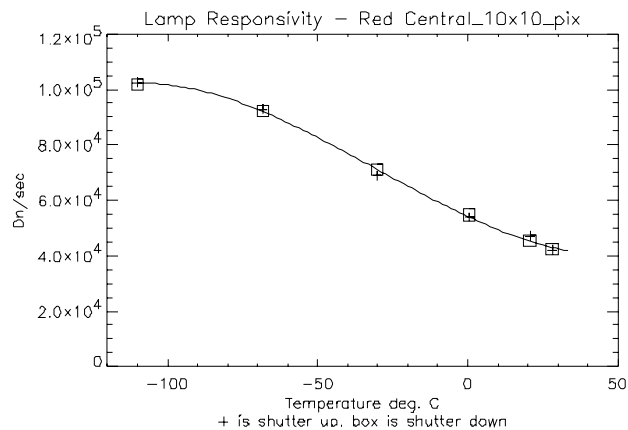
Figure 7.3.2.2c Change in Responsivity of the Red LEDs with temperature.

7.4 Lamp Spectral Shape with Temperature

The 2001 RAC lamps use Red LED's from HP and Blue and Green LED's from Nichia for the illumination rather than incandescent lamps as used on the 1998 Mars Polar Lander RAC. The spectral shapes of the red lamps at approximately –94 degrees C and 15.5 degrees C are shown in Figures 7.4.1 and 7.4.2. The green and blue lamps at similar temperatures are shown in Figure 7.4.3-7.4.6. Because of the under sampling of the data, the peak wavelengths were estimated by fitting with a gaussian plus single order polynomial, which is also shown in the figures. The fit is only good for the points shown, the tails of the spectrum are sinple exponential roll offs and are not fit well with the gaussian form.

As can be seen, the peak wavelength of the red LED's drops significantly in wavelength with temperature, (-18.4 nm). The green and blue LED's drops are much smaller, (green, – 1.8 nm, blue, – 2.7 nm). The temperature shown is the temperature of the lamp housing after reaching steady state during thermal vacuum testing. The lamp housing heats up from the power being dissipated by the LED's and current regulating resistors. For example with the camera body at –115 degrees C, the lamp housing warmed 14.7 degrees for the green LED's which the dissipate the least power, and 23.1 degrees for the blue LED's which dissipate the most power. During normal operation, the lamps would only be on for a few seconds and the temperature would relatively constant. These spectrums would be representative of these temperatures for short exposures.

Linear interpolation between data points was used to determine the 50% irradiance point. The change in the peak wavelength and the upper and lower 50%

wavelength over temperature were fit with 2nd order polynomials. The results are shown

in Figures 7.4.7-7.4. 9. The polynomials were used to generate peak wavelengths and +-

50% points at some typical temperatures and are shown in Table 7.4.1. The bandwidth

listed is the difference in the 50% wavelengths. Also listed is the position of the peak as a

percent of the bandwidth from the lower 50% wavelength. The red LEDs show the

largest change in this parameter. It can be seen the shape of the red spectrum at the higher

temperatures, it shows an asymmetric profile, becomes more symmetric at lower

temperatures. The change in this peak position is plotted for all three colors in Figure

7.4.10.

Temperature (degrees C)	-50% Wavelength (nm)	Peak Wavelength (nm)	+50% Wavelength (nm)	Bandwidth (nm)	Position of Peak (% of BW from lower 50%)
Red Lamps					
-95	619.2	626.6	633.5	14.3	51.7
-75	621.2	629.3	636.4	15.3	53.1
-55	623.1	631.9	639.3	16.2	54.2
-35	625.2	634.6	642.3	17.1	55.1
-15	627.2	637.3	645.2	18.0	55.9
5	629.3	640.0	648.2	18.9	56.5
25	631.5	642.7	651.2	19.7	57.0
Green Lamps					
-95	509.1	522.9	541.4	32.2	42.6
-75	508.8	522.9	541.6	32.7	42.9
-55	508.6	523.0	541.9	33.3	43.1
-35	508.4	523.2	542.4	33.9	43.4
-15	508.3	523.5	543.0	34.7	43.8
5	508.2	523.9	543.7	35.5	44.1
25	508.2	524.3	544.5	36.4	44.5
Blue Lamps					
-95	454.2	463.5	474.4	20.2	45.7
-75	454.2	463.8	475.2	21.0	45.7
-55	454.1	464.1	476.0	21.8	45.7
-35	454.1	464.5	476.8	22.6	45.8
-15	454.2	464.9	477.5	23.4	45.9
5	454.2	465.3	478.4	24.1	46.0
25	454.4	465.8	479.2	24.8	46.1

Table 7.4.1 RAC lamp peak and 50% points (from polynomial fits).
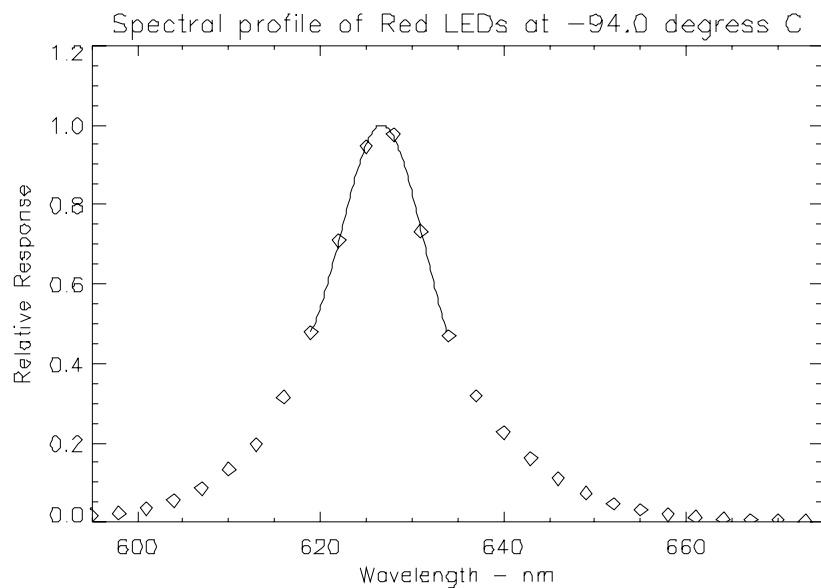
**Figure 7.4.1 Spectral Profile of Red
LED's at –94.0 C.**
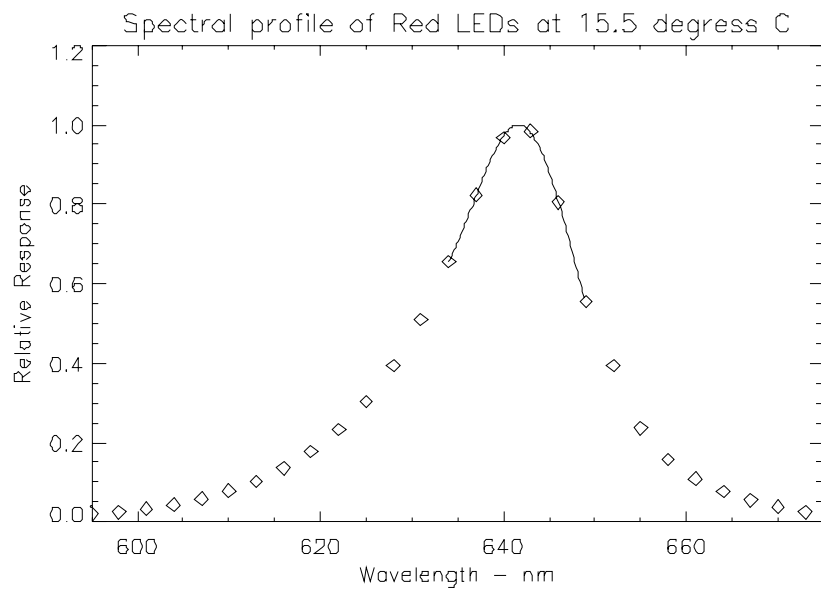
**Figure 7.4.2 Spectral Profile of Red
LED's at 15.5 C.**
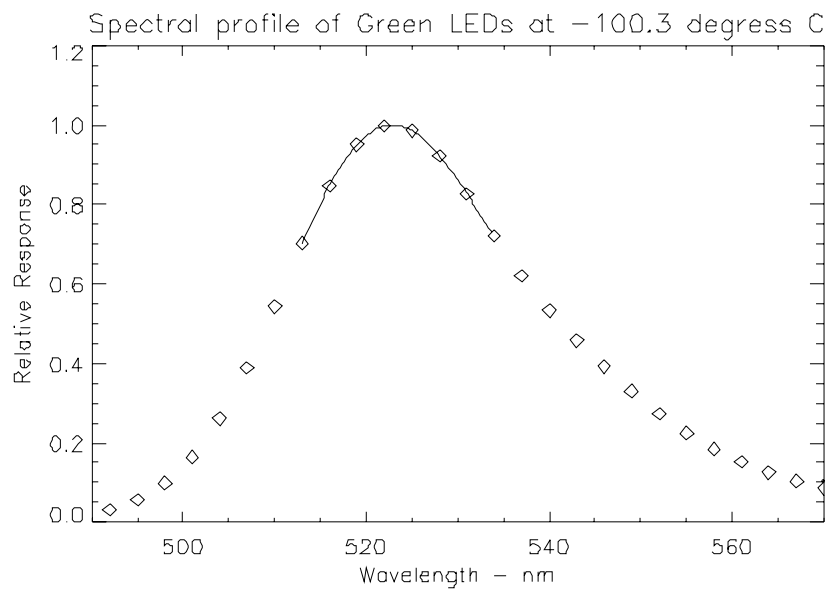
Figure 7.4.3 Spectral Profile of Green LED's at –100.3 C.
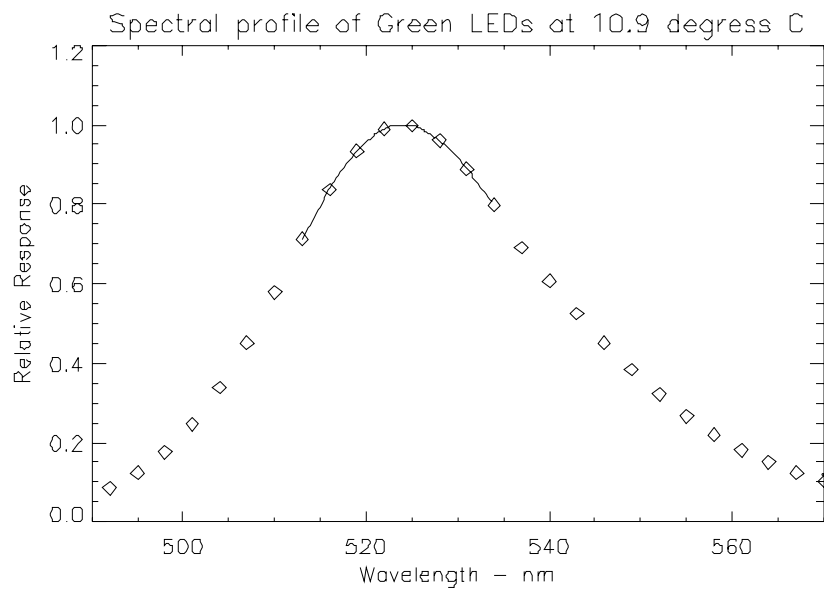
Figure 7.4.4 Spectral Profile of Green LED's at 10.9 C.
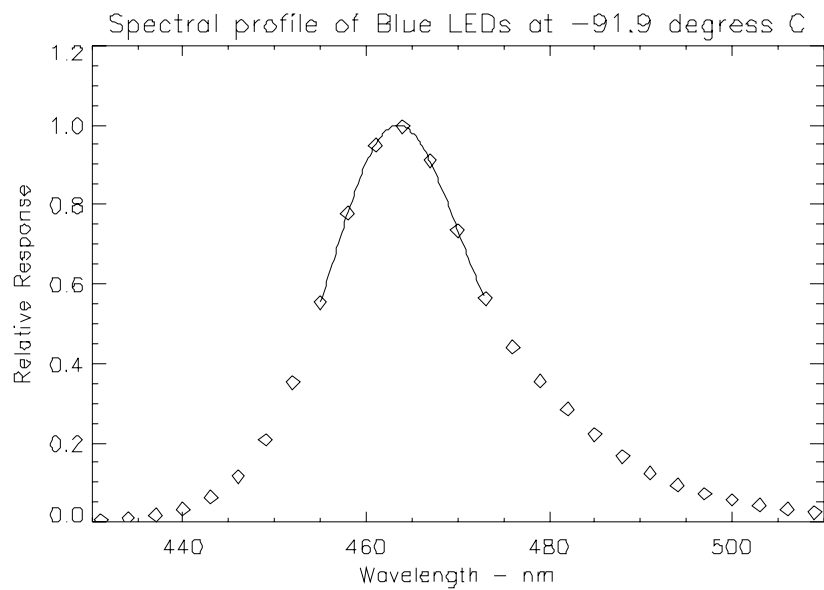
**Figure 7.4.5 Spectral Profile of Blue
LED's at –91.9 C.**
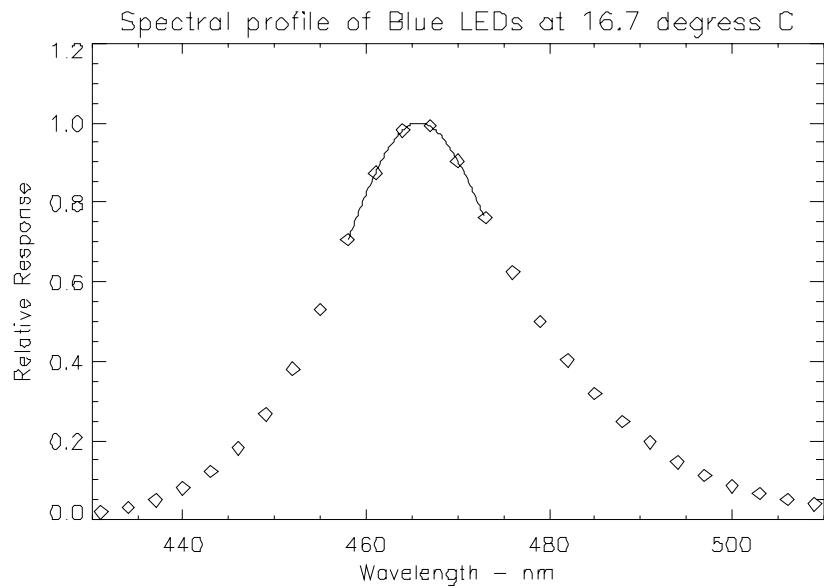
**Figure 7.4.6 Spectral Profile of Blue
LED's at 16.7 C.**
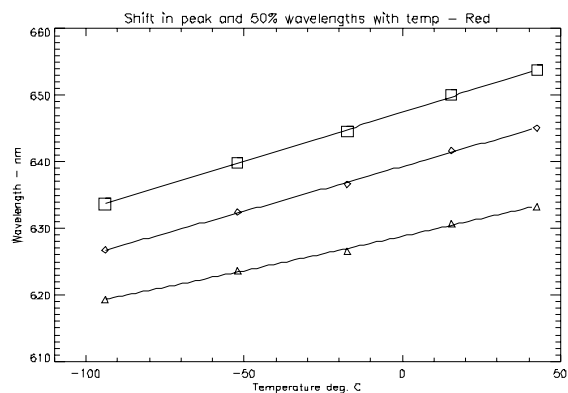
Figure 7.4.7 Shift in peak wavelength and 50% points with temperature for the red LEDs.
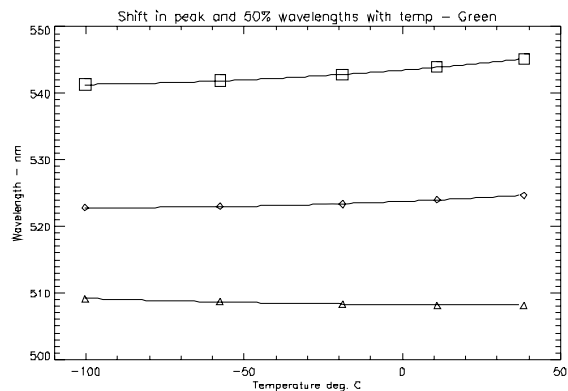
Figure 7.4.8 Shift in peak wavelength and 50% points with temperature for the green LEDs.
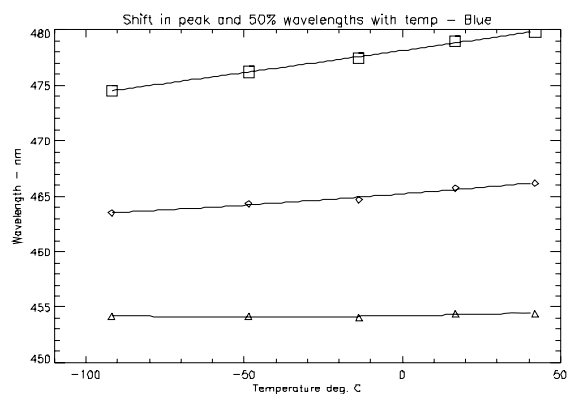
Figure 7.4.9 Shift in peak wavelength and 50% points with temperature for the blue LEDs.
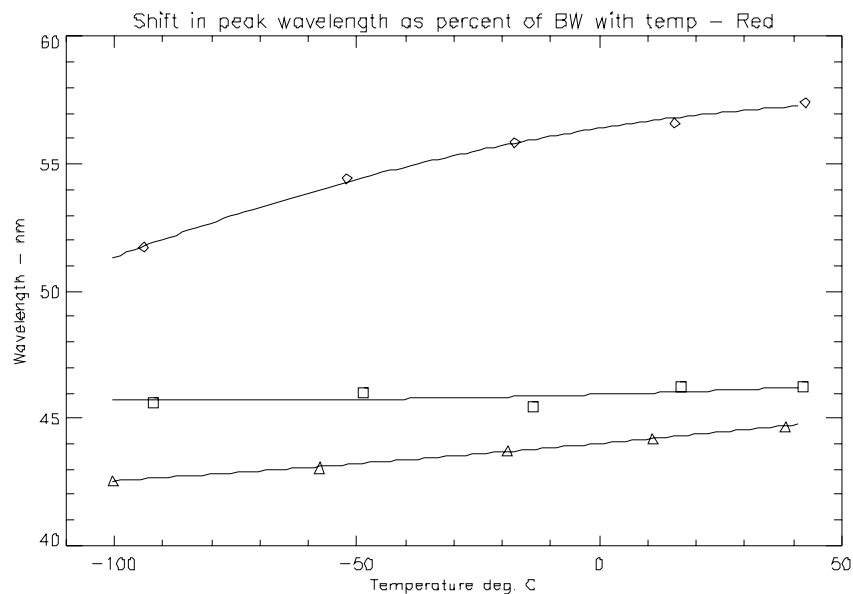
**Figure 7.4.10 Shift in peak wavelength
as a percent of the bandwidths for the
three lamp colors.**

8.0 Distortion

8.1 Experimental Set-Up

Due to the inherent symmetry of a double-Gauss lens, and its use in the RAC, the

distortion present in a RAC image is expected to be very small. At 1:1 imaging with a

perfectly symmetric lens no distortion should be apparent. A review of the optical

prescription in Table 4.3.4.1 shows that the RAC lens is roughly symmetric about the

aperture stop. However, the RAC is to be used for more than just 1:1 imaging scenarios

so it is possible that a small amount of measurable distortion could be present in RAC

images.
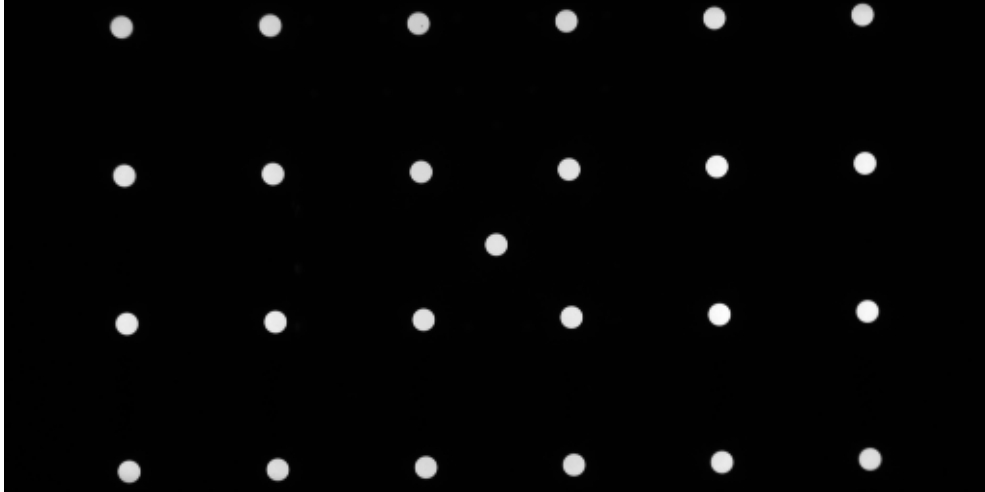
Figure 8.1.1 RAC image of distortion target.

To test for distortion in RAC images we use a target of equally spaced holes manufactured out of photo-etched chrome on glass using the same method used to make masks for coarse pitch integrated circuits. This target is shown in Figure 8.1.1. The target is back-lit and mounted on a translation stage 94 mm away from the RAC. Then a shutter corrected image is taken with the target centered and the RAC lens at focus motor step 279. Next the target is moved 10 mm to the side and imaged again. After that the target is moved 1 mm back toward the center, an image exposed and the target moved another 1 mm. This procedure is repeated until the target is 10 mm off center on the other side of the camera. This scan is conducted in order to have a method of determining image scale.

8.2 Data Reduction

The reduction of the distortion target images into distortion data is carried out using the custom IDL code rac01_distort.pro found in the LPL directory /home/lpl/brentb. The first program function is to read in the image data and correct it for the presence of stray light. This is done by creating a binary threshold image from the data such that where the data DN values are less than 50, the threshold image is given a DN of 0. Everywhere else a value of 1 DN is assigned. This threshold image is then used as a multiplying filter on the original image data to remove the DN values that are not due to the target hole images.

Next the program displays the distortion data image to the user using 2x magnification. Then using the computer mouse, the user clicks near the center of one of the circular dots in the image. The program accepts the user defined position and uses a 31x31 pixel square (less if the image falls too close to the edges of the array) sample about that point to calculate the center position of the dot using a moments calculation similar to Eq. (4.3.2.2). This center position is then read out to a text file and the user continues selecting positions until all the center points in the distortion target have been calculated. The user needs to be careful to select only symmetric circles which are uniformly illuminated, otherwise the center determination using the moments calculation will be in error.

We have found this method to produce very repeatable results as long as the user clicks somewhere on the dot image. Even if one does not click directly in the center, the position measurement result is exactly the same due to the size of the square sample and

the fall-off to 0 DN outside the circle images, which are about 14 pixels in diameter.

Once the target locations are found for all the distortion target images, the analysis proceeds by computing the distances of the various spot images to the center spot image when the target is centered. These distances are then compared to what they would be if no distortion was present in the image using the standard definition of distortion as found in *Smith* (1990).

$$\text{Percent Distortion} = \frac{H'-h'}{h'} \, 100, \qquad (8.2.1)$$

where H' is the actual image height and h' is the paraxial image height. We determine the h' value for each hole position by using the average distance of the four holes closest to the center hole multiplied by the scale factor for each hole. For instance, the scale factor for the four outermost holes is $17^{1/2}$. H' is the actual target center to hole distance measured in the data as described above.

8.3 Results

Initially our measurements of the amount of distortion present in RAC images at focus motor step 279 appeared inconclusive. According to the nominal RAC lens design, including updated thicknesses from the focus model results of Section 6.0, the RAC should exhibit −0.059% distortion at the image position of the target hole furthest from the center for the distortion testing arrangement. Unfortunately this small amount of

distortion was unable to be seen above the scatter in the initial results.

Figure 8.3.1 shows the design intent of the RAC distortion target. Each hole is an equal distance away from every other hole in the target except for the center hole. This distance we denote as D. To understand how image scale changes with detector position we plot the various D values measured for each hole as a function of distance from the center hole in Figure 8.3.2. The value D is not calculated using the distance from the nearest hole but by using the total distance from the center hole divided by the proper scale factor for that hole. For instance, to find D for any one of the four innermost holes, the distance from that hole to the center hole would be divided by $2^{-1/2}$ to obtain D.
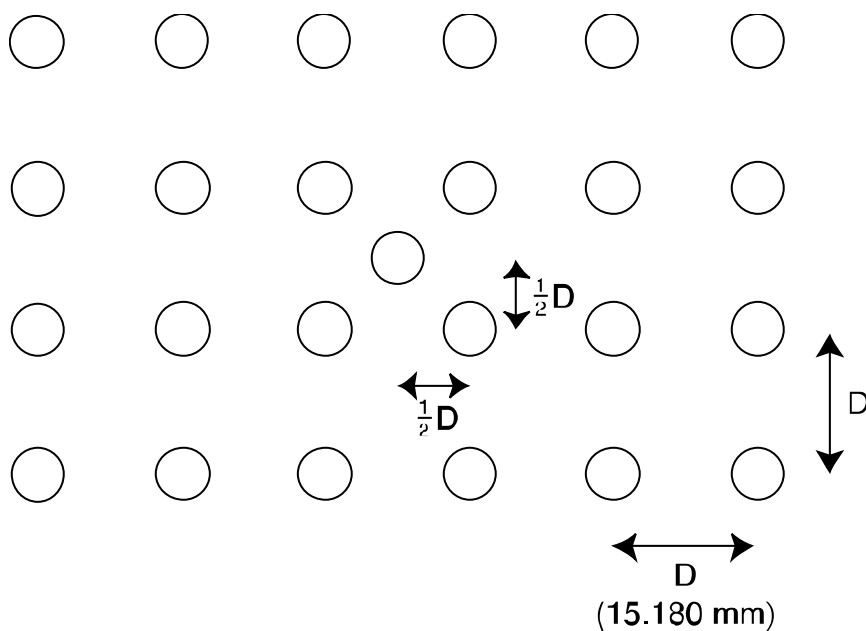
Figure 8.3.1 Schematic of Distortion Target

Figure 8.3.2 shows a tremendous amount of spread in the measurements, beyond

Distance D vs. Distance from Target Center
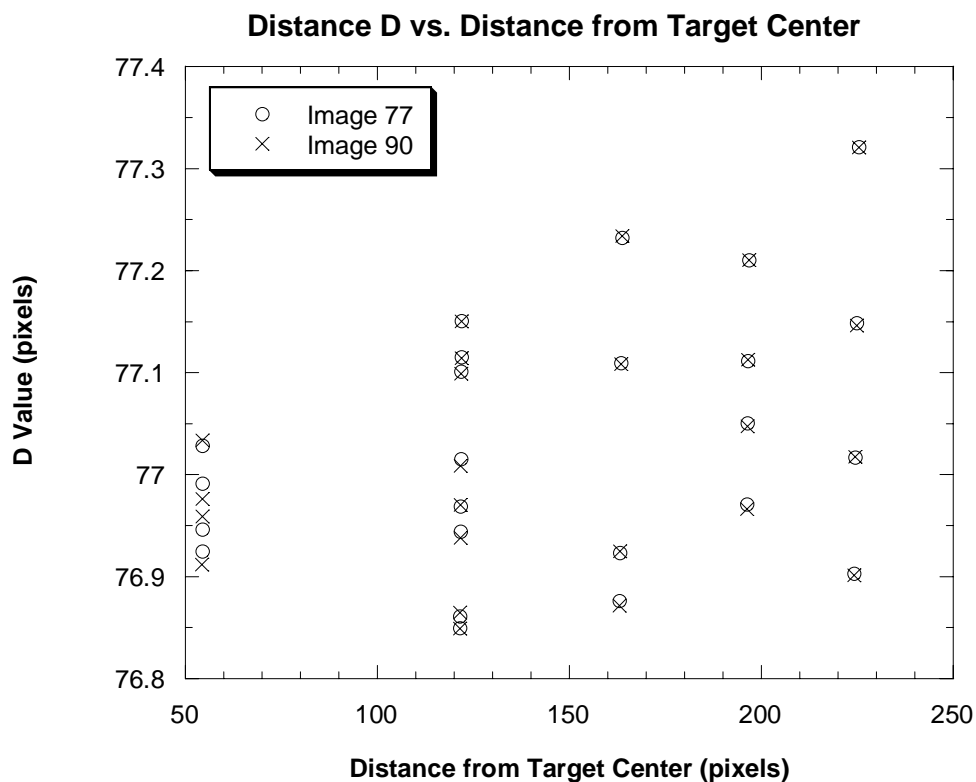
Figure 8.3.2 Initial distortion testing results.

that expected from random error. The spread, in fact, is almost exactly repeatable.

Image 90 was acquired several minutes after image 77 and after the target had moved

completely across the RAC's field of view and then returned to the center position. The

results for the two separate images are almost identical. An analysis of the measurements

reveals that the measurements made from the upper left corner of the target are

consistently larger than those made from the lower right. Apparently a systematic error

was present in the distortion test set-up. To verify this even further a plot similar to

Figure 8.3.2 was made using data from image 88. The image 88 data showed the same

data spread even though this image was taken with the target offset 10 pixels (in image space) from the RAC's optical axis. We knew the effect could not be due to any kind of distortion caused by the RAC lens.

Initially we believed that the data spread was most likely due to some error in target fabrication. An increase in target hole spacing with position, while moving from the lower right to the upper left target corner, would explain the measured spread. Fortunately the actual target used in the testing was still available for inspection. In addition, we also had access to a measuring microscope with approximately 0.75 micron lateral resolution. So we used the measuring microscope to check the spacing between adjacent target holes. Due to the size of the target and the microscope supporting structure we were only able to measure 9 hole spacings but they were spread out over the entire target. The measurement results are shown in Table 8.3.1.

Measurement	Hole Spacing (mm)
1	15.1790
2	15.1835
3	15.1721
4	15.1682
5	15.1768
6	15.1854
7	15.1765
8	15.1872
9	15.1898

Table 8.3.1 Distortion Target Hole Spacing Measurements

The target measurements indicate that the hole spacings are not consistently small

or consistently large for any particular portion of the target. The distances are randomly

spread about the nominal design value of 15.180 mm. It appears that distortion target

fabrication error is not responsible for the data spread.

The only other possible issue with the test arrangement could be target tilt. Figure

8.3.3 shows a simplified schematic of a tilted distortion target. The height, *y'*, of
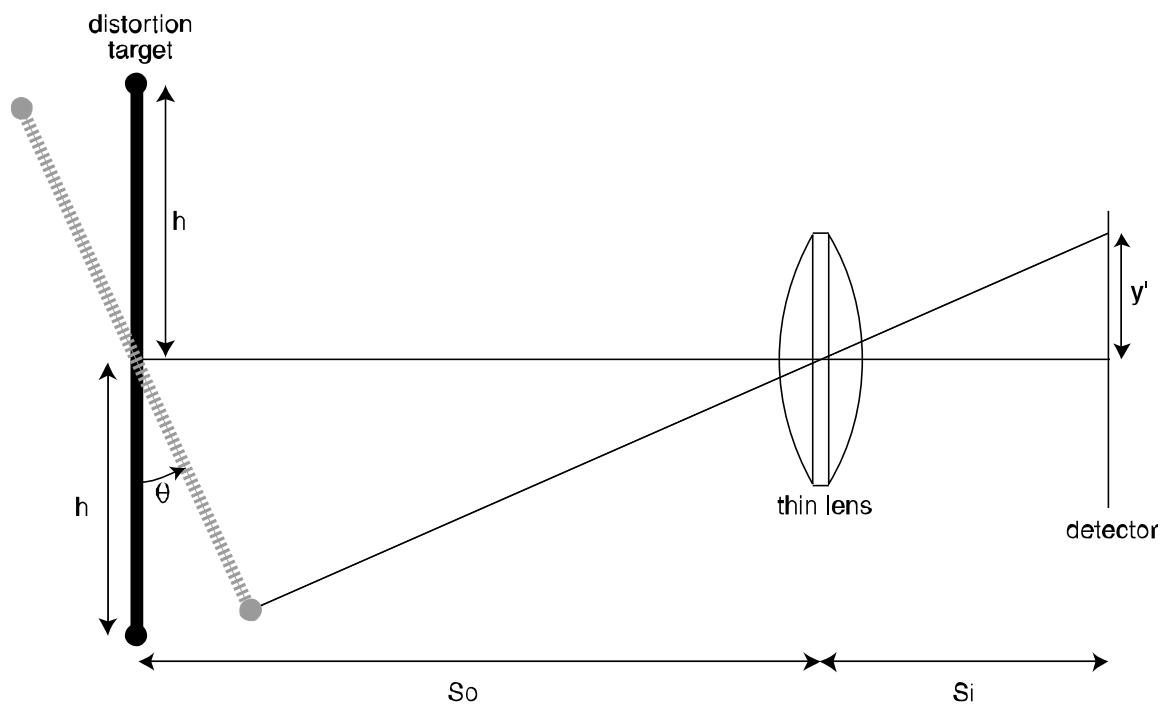
Figure 8.3.3 Illustration of distortion target tilt.

the image follows the equation

$$y' = Si \cdot \frac{h \cdot \cos(\theta)}{So + h \cdot \sin(\theta)} \, , \qquad\qquad (8.3.1)$$

where *h* is negative for the positions below the optical axis. If the rotation, θ, of the

target is small then the following approximation can be made

$$y' = Si \cdot \frac{h}{So + h \cdot \theta}$$
(8.3.2).

For the purposes of this discussion, only the absolute value of the distance from the optical axis is of interest. So for the target position that gets rotated towards the lens shown in Figure 8.3.3 the image distance to the optical axis, L_{in}, is

$$L_{in} = Si \cdot \frac{|h|}{So - |h| \cdot \theta} \quad ,$$
(8.3.3a)

and when the target position is rotated away from the lens

$$L_{out} = Si \cdot \frac{|h|}{So + |h| \cdot \theta}$$
(8.3.3b).

A comparison of Equations 8.3.3a and 8.3.3b reveals that the image of the target point rotated toward the lens and detector will always be further away from the optical axis than for the image of the point rotated away. And both distances are different from the nominal value

$$L_{nom} = Si \cdot \frac{|h|}{So}$$
(8.3.4).

So for any small target rotation, the effect on the image will be an increase in image scale for positions on the target rotated closer to the camera and a reduction in scale for points rotated further away. This type of effect explains the spread observed in the distortion

test data.

Since target rotation could explain the spread in the initial analysis, we decided to attempt a correction of the data based on the paraxial model of the RAC lens and a tilted target plane. The correction applied was a simple shift to the target hole image position based on an assumed amount of tilt. The paraxial model input parameters were: the distance of the target from the entrance pupil, the distance from the exit pupil to the detector plane (not necessarily the image plane) and the ratio of the object space and image space chief ray angles. A small amount of variation was allowed in these "constant" parameters to allow for experimental uncertainty. The unknown, variable parameters were: horizontal target offset, vertical target offset, the target's angle of rotation and the inclination of the target's axis of rotation.

The unknowns were determined by tracing a chief ray through the paraxial lens system to the detector plane at a given target rotation, for each of the distortion target hole positions. The image heights were then compared to what the image heights would be if no rotation were present. From this an image height correction was calculated for each laboratory measurement. Then the target orientation variables were changed to reduce the standard deviation of the corrected laboratory measurements for each type of center to hole distance. The optimizer utilized the Generalized Reduced Gradient (GRG2) nonlinear optimization code developed at the University of Texas at Austin and Cleveland State University, made commercially available by Frontline Systems (2000).

The paraxial model results indicate that the distortion target's upper left corner, as viewed from the camera side, was rotated toward the camera by 0.55°. The axis of

rotation was determined to be at an angle of approximately 18° relative to the horizontal

(or long) axis of the RAC CCD. The corrected results based on those target angles are

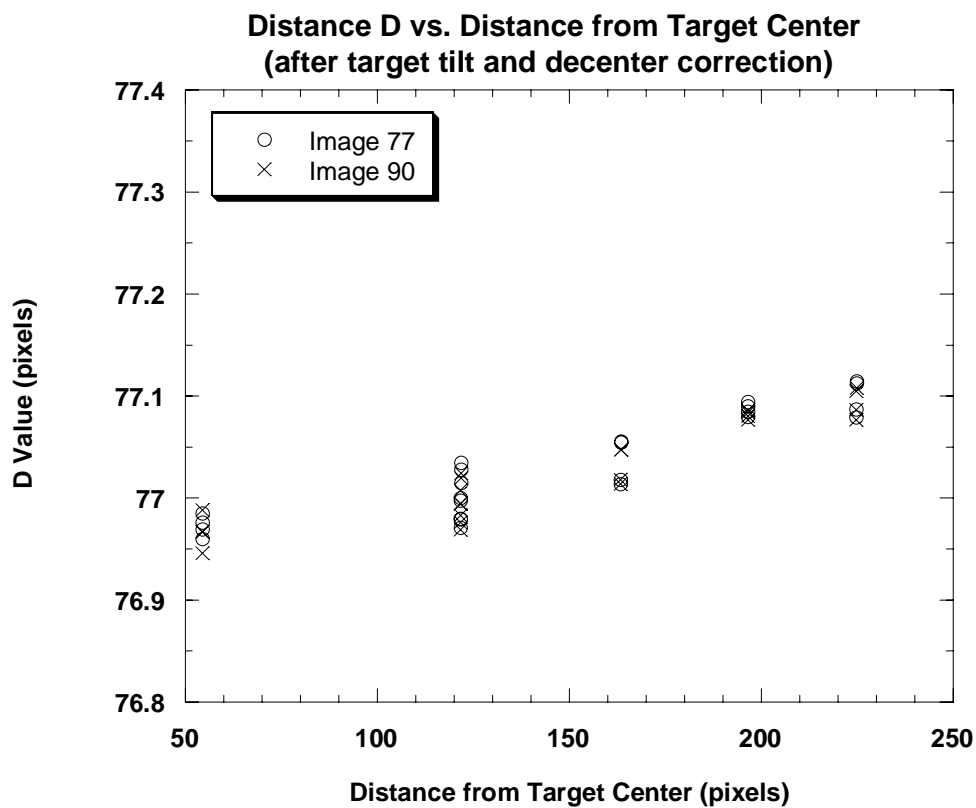shown in Figure 8.3.4 plotted on the same scale as Fig. 8.3.2. The remaining spread in

Figure 8.3.4 Corrected distortion testing results.

the data can be attributed to random error in target fabrication and image center

determination.

The data trend of increasing image scale with distance from the target center

shown in Fig. 8.3.4 could be seen in the original, uncorrected results but the reduction in

data spread allows the confirmation of that effect. Based on the equation for distortion as

given in Eq. 8.2.1, this result is surprising since for negative distortion the data would

have a negative slope. As stated earlier, the nominal RAC optical design predicted a

small amount of negative distortion would be present, -0.055%, at the position of the

target hole farthest from the center. The actual percent distortion measured based on the

corrected results are presented in Figure 8.3.5.
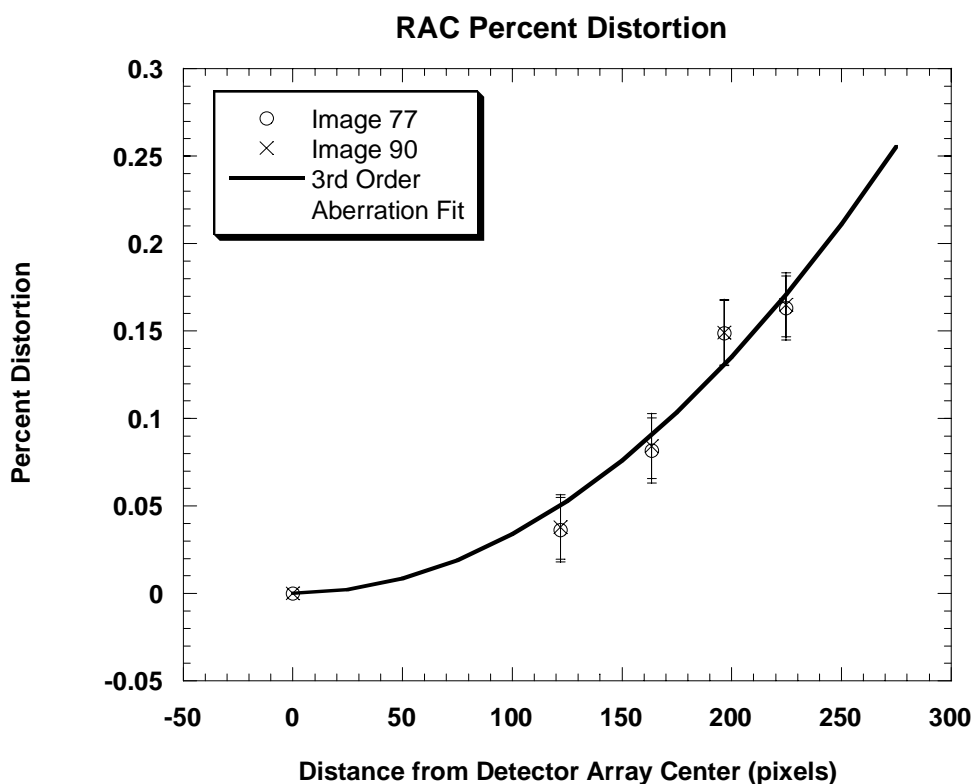
**Figure 8.3.5 The amount of distortion present in a RAC image
at focus motor step 279.**

The positive distortion result was relatively surprising but could not be ignored.

Following this result we explored variations on the RAC nominal lens design using

Zemax (Focus Software 2000). With this lens design code we utilized its standard optimization algorithm to search for new lens to lens spacings that produced the largest amount of positive distortion, while at the same time forcing the prescription to maintain the nominal focal length and image quality. The results were rather startling. For lens to lens distance changes of less than 0.0493 mm from nominal, the RAC lens could have as much as 0.1531% distortion at the position of the target hole corner image. This is similar to the amount of distortion we measured.

According to Shannon (1997), lens to lens spacing accuracy of 0.05 mm is approximately the capability of a commercial to precision level optical fabricator. To get down to 0.001 mm accuracy one needs to use a high precision shop. Similar manufacturing information has been provided by Applied Image Group/Optics of Tucson, Arizona. Their best lens to lens spacing accuracy is ±0.05 mm (Applied Image Group/Optics 2000). So the level of lens spacing error needed to achieve the amount of positive distortion measured is consistent with known optical shop practices. In addition, the RAC lens certainly has other fabrication errors which also could change the amount of distortion measured.

So the sign and amount of distortion we measured in the laboratory is not inconsistent with the RAC lens design and its associated tolerances. The amount of distortion present in the nominal design was so small that variations within fabrication tolerance could result in distortion of either sign being present. One final point concerning the *Zemax* investigation; we found that at focus step 312 the amount of distortion present in the corner of the CCD chip could be as large as 0.29%.

The error bars shown in Figure 8.3.5 are 1 sigma values based on the target hole to hole vertical and horizontal spacing tolerance of ± 10 microns and the uncertainty in measuring target hole image centers on the CCD, ± 0.005 pixels. The errors were assumed to be uncorrelated and were propagated per Bevington and Robinson (1992). The error bars were not calculated using the remaining spread in the corrected distortion data. This would have produced error bars of noticeably smaller extent. Our error propagation analysis reveals that our laboratory set-up, data reduction technique and data correction model allows us to measure distortion of roughly magnitude 0.04% or greater. So, even if the RAC lens had more closely followed the nominal design, our test would have been able to just detect the –0.055% distortion.

The final characteristic of note concerning the distortion results is that they agree with a purely 3rd order or Seidel distortion fit (Born and Wolf 1980). Higher order terms might be important for higher focus motor steps but they are not required for a reasonable fit at motor step 279. The fit is the following

$$\text{RAC \% Distortion} = 3.3786 \times 10^{-6} \cdot (\text{Dist. from Center})^2 , \qquad (8.3.5)$$

where the distance from the center is measured in pixels.

Based on the distortion testing and analysis, we recommend that the RAC be returned to the University of Arizona for further distortion testing. It would be useful to verify the amount of distortion observed in the current data set by conducting more distortion testing. These new tests would be carried out with a larger distortion target, located further away from the RAC so that the effect of target tilt would not be important.

This would require testing with the RAC set at a larger focus motor step to bring the target into focus. Such testing at a larger focus motor step would also be useful in order that we might gain a better appreciation of just how much distortion is present for objects located further away. Extrapolating Eq. 8.3.5 beyond the measurements it is fitted to is not recommended.

9.0 Dark Current Characterization

9.1 Introduction

In Section 5 of this report we discussed the responsivity of the RAC and described in detail how it was determined. Part of that discussion included how the thermal excitation of electrons can lead to measurable pixel signal values even when there are no photons impending on the active section of the CCD. This portion of the report discusses how we measure the dark current of the RAC and develop an accurate model to predict it.

9.2 Experimental Set-Up and Procedure

The experimental set-up to measure thermal dark current is similar to that described and shown in the Absolute Radiometry Section 5.3. In fact, the dark current and absolute radiometry data were all taken as part of the same set of experiments due to their dependence on temperature. The RAC and flight electronics boards were placed inside a thermal vacuum chamber where the temperature was varied from approximately -115-30° C and the pressure was held to around 10^{-5} Torr. Data were acquired at 6 different temperatures in the stated temperature range.

The experimental procedure is to start the test with the RAC at a temperature of approximately -115° C by controlling the temperature of the cold plate in the thermal vacuum chamber. Our testing began after the RAC and flight boards had already been through their flight qualification hot and cold soaks. The soaks ended at -115° C and so it was possible to proceed directly into the dark current testing without having to take the time to bring the chamber temperature down.

With the chamber temperature at -115° C the testing proceeds by placing a cover over the thermal vacuum chamber window the RAC looks through and turning the room lights off. Then take 5 images at the maximum allowable exposure time (32.7675 s), without shutter corrections on, but with the dark strip and null frame options selected. Then take another 5 images with a 0 s exposure, again, without shutter corrections on, but with the dark strip and null frame options selected. Then change the chamber cold plate temperature to approximately -70° C following a rate of 1.25° C/minute. Take the same exposures as before and set the chamber cold plate temperature to -30° C with a warm-up of 1.25° C/minute.

At -30° C increase the number of exposures to 10 to compensate for the increasing variance but otherwise take the same types of images as before. Then repeat this procedure at 0° C, 30° C and room temperature. One issue to be aware of at the 2 warmer temperatures is to make sure there are not any saturated pixels (pixels with a DN of 4095) in the image. If there are, reduce the exposure time until the saturated pixels disappear.

9.3 Data Reduction and Modelling

Data reduction on the RAC dark current data was carried out using the following custom IDL routines located in the /home/lpl/brentb directory: rac01_dark_model.pro, rac01_dark_shutter.pro, rac01_dark_null.pro, dark_model2.pro, dark_model4.pro and rac01_dark_model_sat.pro.

Our modelling approach was slightly different than that used by the MAGI team in the past. According to Reid et al. (1999) and Smith et al. (2001), the theoretical dark current model used for the Imager for Mars Pathfinder, the Mars Polar Lander Surface Stereo Imager and the Mars Polar Lander Robotic Arm Camera followed this form,

$$DN(T, t, x, y) = A_D \, t \, e^{(B_D \, T)} \, D(x, y) + A_S \, e^{(B_S \, T)} \, S(x, y)$$
$$+ A_N \, e^{(B_N \, T)} + \text{Offset}, \qquad (9.3.1)$$

where t is exposure time, T is temperature, (x, y) is the pixel location and the other factors represent measured coefficients. A review of the best current CCD literature reveals that this dark current model is incomplete. And so we derive the following RAC dark current model from Buil (1991) and Janesick (2001),

$$DN(T, t, x, y) = A_D \, t \, T^{1.5} \, e^{(-E_g/(2\,k\,T))} \, D(x, y) + A_S \, T^{1.5} \, e^{(-E_g/(2\,k\,T))} \, S(x, y)$$
$$+ A_N \, T^{1.5} \, e^{(-E_g/(2\,k\,T))} + \text{Offset}, \qquad (9.3.2)$$

where t is exposure time in seconds, T is temperature in Kelvin, (x, y) is the pixel location, E_g is the silicon bandgap energy, k is Boltzmann's constant in eV/K and *Offset* is the CCD

hardware offset in DN. The A_D, A_S and A_N parameters are still determined from the experimental data as before but their values are proportional to pixel area and the dark current figure of merit. Notice that we have eliminated 3 unknowns from the previous dark current model, B_D, B_S and B_N, and replaced them with the well-known silicon bandgap energy, E_g. The silicon bandgap energy is a known function of temperature and is given by Pankove (1971)

$$E_g = 1.1557 - \frac{7.021 \text{x} 10^{-4} \text{ T}^2}{1108 + \text{T}}, \qquad (9.3.3)$$

where *T* is again temperature in Kelvin.

Equation (9.3.2) encompasses the same effects as described in Section 5.3 of this report and specified in Equation (5.1.1). The form of Eq. (9.3.2), however, allows easier analysis for the type of dark current experimentation we performed. The equation includes all the effects that go into a dark current image frame: the hardware offset, the thermal noise generated during the readout process, and the dark current accumulated during an exposure.

In Eq. (9.3.2) there are three unknown coefficients to be determined, A_D, A_S and A_N; two unknown 512x256 normalized arrays, *D(x,y)* and *S(x,y)*; and an unknown hardware offset value, *Offset*. The determination of each unknown involves analyzing different types of images so that the various effects can be separated out.

The first unknowns to be calculated are A_N and *Offset*. These are found by taking the null frames saved at the various temperatures during the experiment and fitting the

last two terms of Eq (9.3.2) to the null frame data while forcing the first two terms to be zero. We believe that the null data should only be affected by the thermal noise in the readout pixels and the hardware offset. The null data is read-out as a 256x4 array but physically it is only comprised of 4 electron wells. And so each null frame is averaged to create a mean value for each frame at each temperature. We perform the model fit using IDL's (*Research Systems* 1999) built-in gradient expansion algorithm to compute a non-linear, least squares fit to the data. Notice, that although the hardware offset is slightly temperature dependent, we ignore this in the fit following the approach used in the past. We also should note that we investigated including a constant temperature offset factor in the model of Eq. (9.3.2). It is conceivable for the CCD silicon temperature to be at a slightly different temperature than the temperature recorded by the CCD temperature sensor. Following the approach of Frieden (1983), we found to a confidence level between 10 and 25% that an added temperature offset variable was statistically insignificant. This is not a high confidence level but it is not low enough to warrant including the temperature offset term according to Frieden. Figure 9.3.1 shows a plot of the theoretical model and the null frame response versus temperature data. The best-fit model parameters are: $A_N = 4.6973 \times 10^6$ DN/K$^{3/2}$ and *Offset* = 8.7247 DN.

Once the A_N and *Offset* variables are known, one can proceed to determine the A_S and $S(x,y)$ variables. The A_S variable is simply a coefficient like the one found for the null data with units of DN/K$^{3/2}$. The $S(x,y)$ variable is a normalized, two-dimensional array which represents the shutter response of each individual pixel as a fraction of the A_S variable. The effect we are trying to quantify here is the amount of dark current that

accumulates in the imaging and storage sections of the CCD during read-out alone. So to

calculate these two variables we use the dark frame data with 0 second exposure times
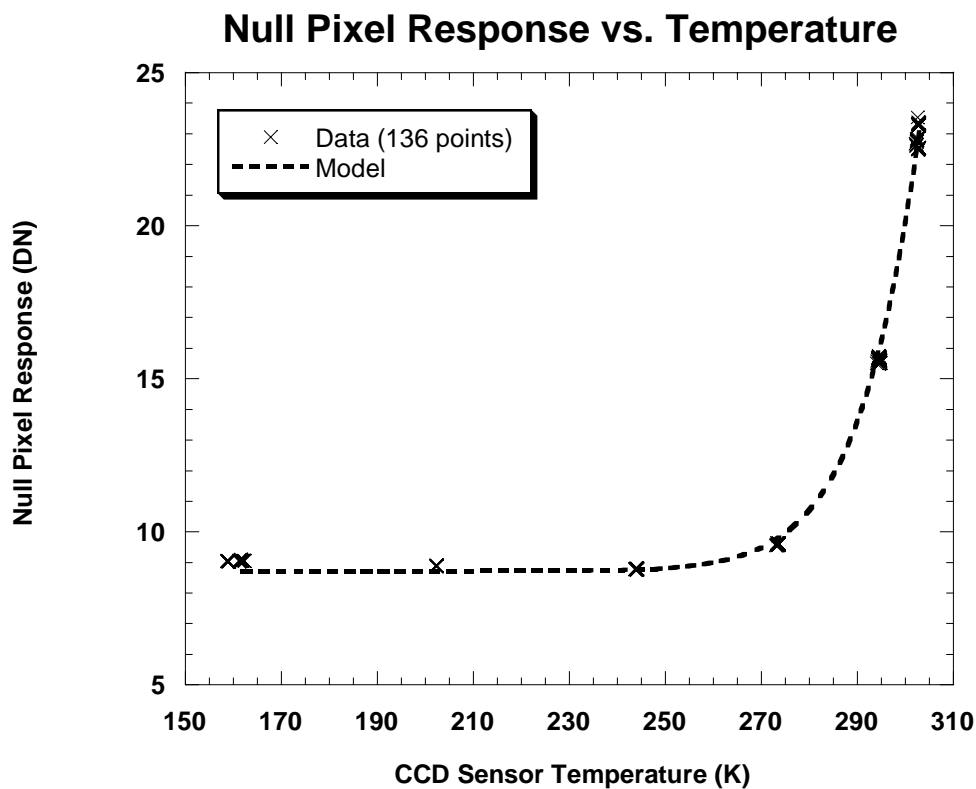
Null Pixel Response vs. Temperature

Figure 9.3.1 Null frame response as a function of temperature.

acquired at the various temperatures and then subtract the appropriate model null

response and offset. Then we fit this data to the second term in Eq. (9.3.2), again using

IDL's (*Research Systems* 1999) built-in gradient expansion algorithm to find a least-

squares fit at each pixel location, a total of 131,072 locations. We find $A_S = 7.0863 \times 10^7$

DN/K$^{3/2}$. Its location on the array is at pixel (1,0) so that $S(1,0) = 1$. We expected the

maximum value to occur at (0,0) but that pixel appeared to be unresponsive during this test and only had a value of 0 DN. The resulting *S(x,y)* array looks like an average shutter image. It is shown in Figure 9.3.2. The differences in the column responses are visible in the image.
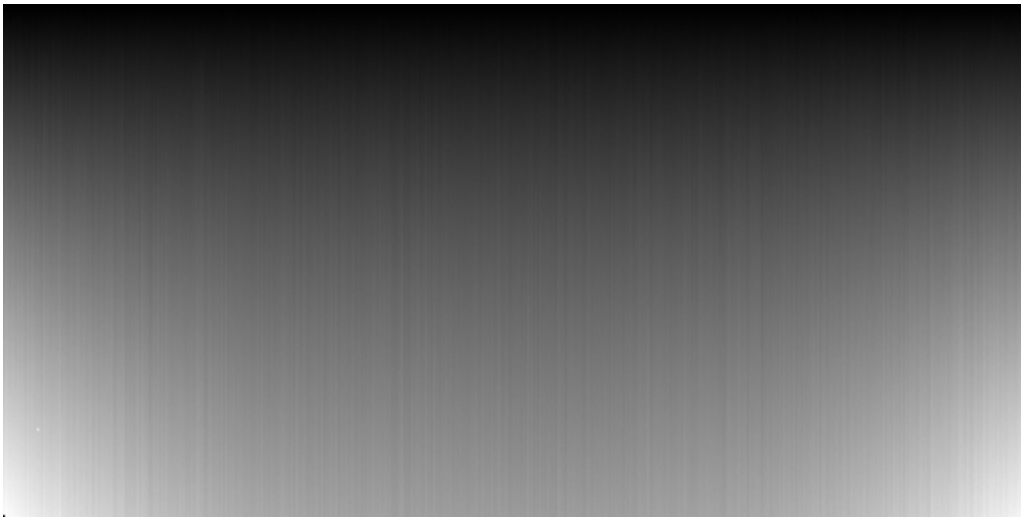

Figure 9.3.2 *S(x,y)* **from Eq. (9.3.2) which shows how a typical shutter image (an image with 0 s exposure and no light incident on the detector) appears.**

The final portion of the model fitting is to determine A_D and *D(x,y)*. We do this by reading the DN values from the images that were acquired at the maximum exposure time possible without saturation (normally 32.7675 s). And then DN values calculated from the known terms of the model are subtracted from the image DN values. Finally, the resulting numbers are divided by the exposure time of the image and fit to the first term of Eq. (9.3.2) as a function of temperature using IDL's (*Research Systems* 1999) non linear least squares fit routine. Our analysis found $A_D = 9.4871 \times 10^7$ DN/K$^{3/2}$/s. The

results for the $D(x,y)$ array are shown in Figure 9.3.3. Again we note that the raw image

data showed DN(0,0) = 0.

Figure 9.3.3 $D(x,y)$ from Eq. (9.3.2) which shows how a typical dark image appears after it has been shutter corrected.

9.4 Summary and Error Estimates

      The final parameters for the RAC dark current model are summarized in Table

9.4.1. The $S(x,y)$ and $D(x,y)$ arrays are stored as IDL variables along with the values for

A_S and A_D in /home/mars/brentb/rac01_dark_model/final_image&shutter_coeff.dat.

      Using the model parameters we can predict the amount of dark current signal to

expect for any pixel of the RAC at any given temperature. For instance, for a 1 s

exposure at a typical RAC temperature on Mars of 0°C, the dark current model predicts

the amount of signal due to thermal noise at a typical pixel would be approximately 46

DN. About 20% of that signal would be due to the 8.7247 DN hardware offset, roughly

2% would be due to the read-out noise, 34% would come from the shutter effect and the

last 56% would come from the 1 s integration time for the exposure. If the frame were

shutter corrected, we would expect 21 DN. So we can safely assert that with RAC

imaging on Mars, for most exposure times we do not expect the dark current to exceed

100 DN.

The uncertainties in the model parameter fits are given in Table 9.4.1 and Figure

9.4.1. The values plotted in Figure 9.4.1 were calculated first by dividing the 1 σ

uncertainty of each parameter at each pixel location by the parameter value at that pixel

location. Those values were then multiplied by 100 and the median error of each CCD

row (the median error of the 512 pixels in each row) was calculated in order to find the

typical error for that row.

The model parameters are known to quite high accuracy except for some parts of

Table 9.4.1 Dark Model Parameters

PARAMETER	VALUE	1 σ UNCERTAINTY
Offset	8.7247 DN	0.1175 DN
A_N	4.6973×10^6 DN/K$^{3/2}$	7.030×10^4 DN/K$^{3/2}$
A_S	7.0863×10^7 DN/K$^{3/2}$	See Fig. 9.4.1
S(x,y)	Array of values 1.0-0.00015*	See Fig. 9.4.1
A_D	9.4871×10^7 DN/K$^{3/2}$/s	See Fig. 9.4.1
D(x,y)	Array of values 1.0-0.06167*	See Fig. 9.4.1

* Excluding the value of 0 at unresponsive pixel location (0,0).

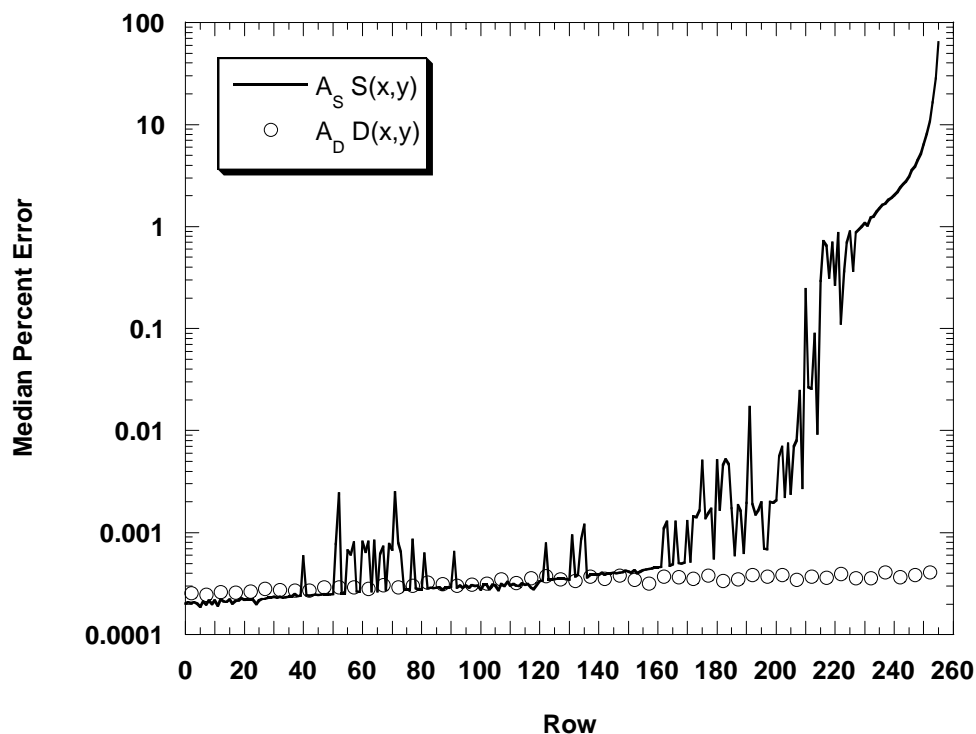## Median Percent Error of Dark Model Parameters vs. CCD Row

Figure 9.4.1 A plot of the typical 1 σ percent errors for the dark model parameters $A_S\ S(x,y)$ and $A_D\ D(x,y)$ versus row location on a RAC image.

the $A_S\ S(x,y)$ parameters. Figure 9.4.1 clearly shows that towards the top of a RAC

image, the values for $A_S\ S(x,y)$ are not known with high accuracy. At row position 229

the typical percent error goes over 1%. And at the very top of the image, at row 255, the

median error is 64.0%. This high amount of relative error is due to the small amount of

shutter dark current at the top of a RAC image. The top portion of the image is the first

row to be shifted to the horizontal readout register and so it accumulates very little

thermal charge before it is read out. So the signal to noise ratio is quite small, the signal

in this case being the dark current. To improve the accuracy of the model parameters in

that part of the array we would need to take a lot more shutter frames during testing since increasing the exposure time is not an option. In order to increase the signal to noise ratio by 1 order of magnitude it would take 1000 shutter dark exposures. That is impractical.

Fortunately, >1% uncertainty in the shutter dark parameters applies only to the upper 11% of the array. For the rest of the array positions, all 6 model parameters are known with high accuracy. The two array parameters tend to have the same relative uncertainty for most positions at the 0.001% level.

It is important to keep in mind the proper interpretation of the model parameter uncertainties. The uncertainties tell us how repeatable the model results would be if a new set of data were used to determine the fit, and not necessarily the accuracy of the fit itself relative to a new set of real data.

To get an idea of how well the model fits real data, we have compared a real dark current image with one produced by the model. The dark frame was obtained at a recorded CCD temperature of 29.2 K, an exposure time of 15.0 s and no shutter correction was applied. Those same values were input into the model of Eq. (9.3.2) to generate a 2-dimensional image. The actual dark frame was then subtracted from the model results to determine the absolute error. Then the error was divided by the dark frame DN values and multiplied by 100 to obtain the percent difference error. The results for most of the pixels are plotted as a histogram in Figure 9.4.2.

The histogram of the percent errors shows that the model and data agree quite well with one another. Of the total 131,072 RAC image pixels, 131,040 or 99.98% of them are plotted within the bounds of Fig. 9.4.2. The most extreme errors were at pixels
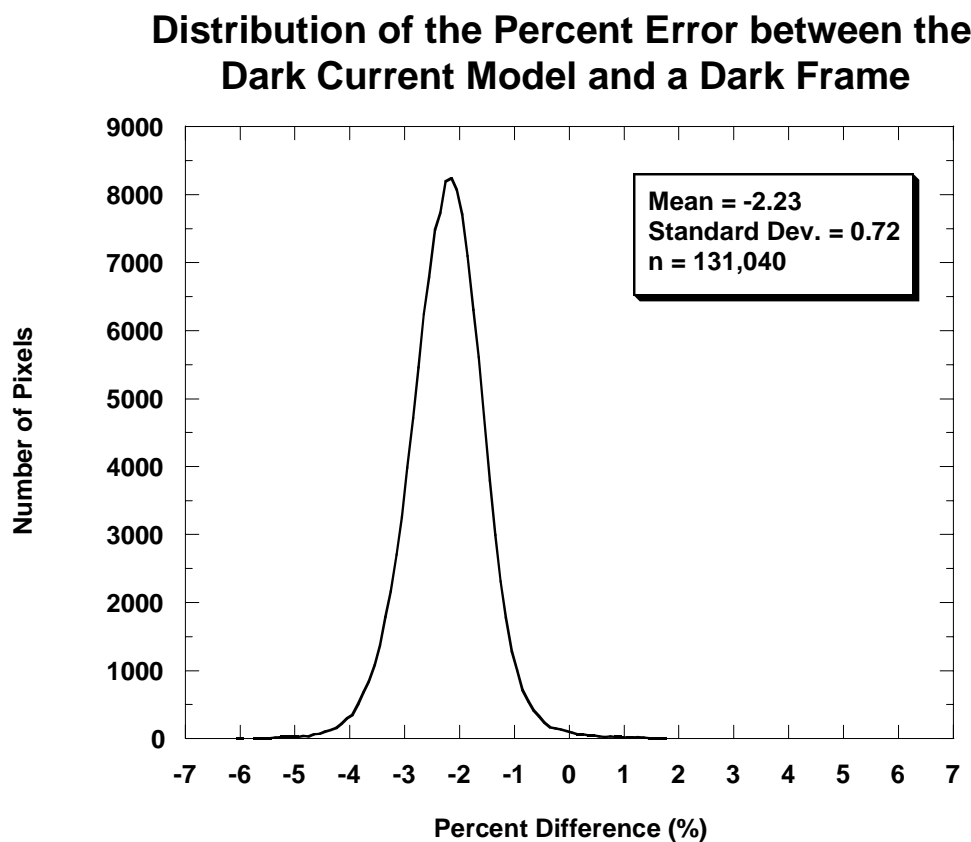
Distribution of the Percent Error between the Dark Current Model and a Dark Frame

Figure 9.4.2 A histogram of the pixel response error between the final dark model and an actual dark frame.

(383,134) and (59,94) and their occurrence is not represented in the plot. At pixel

(383,134) there was a maximum error of 16.8% and at pixel (59,94) there was a

minimum error of –19.8%. The overall distribution of the error across the image was

uniform, however, and there were not any trends evident.

The absolute accuracy of the dark model DN values were low by about 2%. The

model slightly underestimated the signal due to the thermal noise. Error at the 2% level

though is quite good in this case, given that the data was taken in a very steep part of the

curve of Eq. (9.3.2). A review of Figure 9.3.1 shows that at 29.2 K, the temperature

dependence of the dark current is very steep. And so the resulting DN values of the model are very sensitive to the temperature uncertainties.

10.0 Summary and Recommendations

The 2001 Robotic Arm Camera's imaging performance has been well characterized with the laboratory experiments and data analysis that we have described. Our analysis of the calibration data for this camera is at a level that we were not able to achieve with the Mars Polar Lander RAC due to the time constraints and loss of the mission. The RAC parameters reported in the past (*Keller* 2001) have lacked sufficient detail for full calibration of images. The numbers provided in this report will allow RAC images from Mars to be analyzed with high accuracy. Using the information we have produced, instrument effects will be able to be identified and removed from the images to allow proper interpretation of the Martian soil and surface.

There are a few remaining camera characteristics, for which we already have data, that will need to be reported in more detail when the RAC begins its mission on the surface of Mars. We have completed an initial analysis of the laboratory stray light data that shows that stray light and ghost imaging are well-controlled. We also have data, yet to be utilized, on the effectiveness of the robot arm baffles and the RAC response to imaging of standard color chips. Those areas will be studied in more detail after the RAC has initiated its mission on the surface of Mars and the results will be published in a later version of this document.

Before the '01 RAC is integrated into the Mars spacecraft and launched to Mars,

we believe it would be beneficial to return the RAC to the Lunar and Planetary Laboratory for some further testing. Our calibration analysis has revealed that 1-2 weeks of further testing could increase our understanding of the RAC even further, and perhaps improve upon its performance.

In Section 4.0 we discussed how the image quality of the RAC varies across its field of view a lot more than the nominal lens design suggests it should. We would like to do a few more MTF measurements on the camera to confirm that the point spread function in the upper left and lower right hand corners of the images are strongly asymmetric. And if such a test were to confirm that, we would seek to correct this performance by correcting the current lens or replacing it with one of the flight spares.

We would also like the opportunity to be able to do a full test of the RAC's spectral response from 0.4-1.0 μm. For some of the results reported in Section 5.0, we had to rely on the manufacturers' reported spectral characteristics of various components to determine the camera's response in certain situations, components like the CCD and the IR-filter. We would be able to achieve lower uncertainties if we would be able to test the RAC's response to the known spectral output of a monochrometer. This is an instrument we already possess and if we just performed the test at ambient temperature, we could complete it in a day.

In Section 7.0 we highlighted how there were some serious issues with the RAC lamp flat field data. We were able to achieve quite good results with the data we have but we should be able to do better. In particular, we should really have full flat field data for focus motor steps 177, 198, 217 and 234 which would require testing with a

rectangular reflectance target instead of a circular one. In addition, we should be able to achieve better accuracy at the lower focus motor steps if we conduct the lamp flat field testing while the target is rotating or vibrating. This would help blur out the structure in the Spectralon targets when they are viewed under high magnification.

And the final test we would like to perform is to measure the amount of distortion present in a RAC image at 10:1 and infinity focussing. The test we already completed was for 10:1 imaging. But unfortunately the results at that focus motor position show that the RAC produces positive distortion instead of the expected negative distortion. Our theoretical modelling in Section 8.0 showed that this is not unexpected but it would be good to verify our results. And since our testing at 10:1 imaging gave results different from the nominal lens model, it is uncertain just how much distortion would be present in a RAC image taken at infinity focus. We can use the model we have to extrapolate how large the distortion should be, as we already have done. But it is risky to put a lot of confidence in those results since there are numerous combinations of model variables that can reproduce the results we saw at 10:1 imaging.

If it proves impractical to return the 2001 RAC to our laboratory, we still feel very comfortable with the performance of the camera and our knowledge of its characteristics. When it finally reaches the Red Planet, we will be able to extract information from the surface that no one has ever seen before.

References

Applied Image Group/Optics, Tucson, AZ, personal communication, March 2000.

Bevington, P. R. and Robinson, D. K., *Data Reduction and Error Analysis for the Physical Sciences, 2nd Edition*, McGraw-Hill, 1992.

Born, M. and Wolf, E., *Principles of Optics: Electromagnetic Theory of Propagation, Interference and Diffraction of Light 6th Edition*, p. 217, 1980.

Buil, C., *CCD Astronomy*, Willmann-Bell, Inc., p. 38, 1991.

Focus Software, Inc., *Zemax EE 9.0*, Tucson, AZ, 2000.

Frieden, B. R., *Probability, statistical optics, and data testing: a problem solving approach*, Springer-Verlag, 1983.

Gaskill, J. D., *Linear Systems, Fourier Transforms, and Optics*, John Wiley, New York, 1978.

Hartwig, H., Mars Surveyor Lander 2001 Robotic Arm Camera (RAC) Acceptance Data Package, Max-Planck-Institut für Aeronomie, Katlenburg-Lindau, Germany, 1998.

http://www.frontsys.com, 2000.

Janesick, J. R., *Scientific Charge-Coupled Devices*, SPIE – The International Society for Optical Engineering, p. 622, 2001.

Keller, H. U., H. Hartwig, R. Kramm, D. Koschny, W. J. Markiewicz, N. Thomas, M. Fernades, P. H. Smith, R. Reynolds, M. T. Lemmon, J. Weinberg, R. Marcialis, R. Tanner, B. J. Bos, C. Oquest, D. A. Paige, The MVACS Robotic Arm Camera, *J. Geophys. Res.*, 1*06*(E8), 17609-17621, 2001.

Labsphere, A Guide to Integrating Sphere Theory and Applications, www.labsphere.com/tech_info/tech_pub.htm, 2000.

Maki, J. N., J. J. Lorre, P. H. Smith, R. D. Brandt, D. J. Steinwand, The color of Mars: Spectrophotometric measurements at the Pathfinder landing site, *J. Geophys. Res.*, 1*04*(E4), 8781-8794, 1999.

Max-Planck-Institut für Aeronomie, MECA and LRAC CCD FM Specs., Katlenburg-Lindau, Germany, June 1999.

Neckel, H. and D. Labs, The solar radiation between 3300 and 125000 ⊕, *Solar Physics*, 90, 205-258.

Palmer, J., University of Arizona Optical Sciences 506 class notes, 1996.

Pankove, J., *Optical Processes in Semiconductors*, Dover Publications, p. 27, 1971.

Reid, R. J., P. H. Smith, M. Lemmon, R. Tanner, M. Burkland, E. Wegryn, J. Weinberg, R. Marcialis, D. T. Britt, N. Thomas, R. Kramm, A. Dummel, D. Crowe, B. J. Bos, J. F. Bell III, P. Rueffer, F. Gliem, J. R. Johnson, J. N. Maki, K. E. Herkenhoff, R. B. Singer, Imager for Mars Pathfinder (IMP) image calibration, *J. Geophys. Res*., 1*04*(E4), 8907-8925, 1999.

Research Systems, Inc., *Interactive Data Language 5.2*, (Boulder: RSI, 1999).

Rizk, B., The Private Life of an Integrating Sphere: the Radiant Homogeneity of the DISR Calibration Sphere, *Applied Optics* 40(13), 2095-2101, 2001.

Shannon, R. R., *The Art and Science of Optical Design*, Cambridge University Press, 1997.

Smith, P. H., R. Reynolds, J. Weinberg, T. Friedman, M. T. Lemmon, R. Tanner, R. J. Reid, R. L. Marcialis, B. J. Bos, H. U. Keller, W. J. Markiewicz, R. Kramm, F. Gliem and P. Rueffer, The MVACS Surface Stereo Imager on Mars Polar Lander, *J. Geophys. Res*., 1*06*(E8), 17589-17607, 2001.

Smith, W. J., *Modern Optical Engineering: the design of optical systems*, McGraw-Hill, Inc. 1990.